
Sensor development for highly resolved measurements in turbulent flows

Jaroslav Puczyłowski

Der Fakultät für Mathematik und Naturwissenschaften
der Carl von Ossietzky Universität Oldenburg
zur Erlangung des Grades und Titels eines

**DOKTORS DER NATURWISSENSCHAFTEN
DR. RER. NAT.**

angenommene Dissertation

von Herrn Jaroslav Puczyłowski
geboren am 12. Oktober 1982 in Cosel / PL



1. Gutachter: Prof. Dr. Joachim Peinke
2. Gutachter: Prof. Dr. Rustom Bhiladvala
3. Gutachter: Prof. Dr. Niklas Nilius
4. Gutachter: Dr. Martin Silies

Tag der Disputation: 26.09.2015

Abstract

This dissertation presents the continuing work on the development of a novel anemometer, namely the 2d-Laser Cantilever Anemometer (2d-LCA). The primary achievement reached in the course of this development is the creation and successful testing of a series of new sensing elements (cantilevers), which show significant improvement with regard to the angular resolution power of the anemometer when compared to previous prototypes. The performance of the new cantilevers has been tested by means of comparative measurements with standard commercial x-wires. The evaluation of the collected data of both anemometers shows a good agreement between the statistics. Further ideas for cantilever designs are presented, which are believed to further improve the performance of the 2d-LCA. An application for a patent for these new designs has been filed recently (file number: 102015000064.0).

Zusammenfassung

Diese Dissertation beschäftigt sich mit der Weiterentwicklung eines neuartigen Anemometers, dem so genannten 2d-Laser Cantilever Anemometer (2d-LCA). Als wichtigsten Entwicklungsschritt ist die Erschaffung und die erfolgreiche Untersuchung einer Reihe von neuen Messspitzen (Cantilevern) zu nennen. Diese Cantilever weisen im Vergleich zu den vorgängigen Prototypen ein deutlich besseres Auflösungsvermögen bzgl. der Strömungsrichtung auf. Die Leistungsfähigkeit der neuen Cantilever wurde anhand von Vergleichsmessungen mit kommerziellen X-Drähten untersucht. Die statistische Auswertung der Datensätze beider Anemometer zeigt eine gute Übereinstimmung. Des Weiteren werden Entwürfe für weitere Cantilever präsentiert, die die Leistungsfähigkeit des 2d-LCAs weiter ansteigen lassen können. Für diese Entwürfe wurde kürzlich eine Patentanmeldung eingereicht (Az.: 102015000064.0).

Contents

| | |
|---|-----------|
| Introduction | 1 |
| Structure of this thesis | 4 |
| 1 Basic concepts and statistical description | 5 |
| 1.1 Turbulence theory | 5 |
| 1.2 Stochastic tools and length scales in turbulent flows | 8 |
| 1.2.1 Structure functions | 8 |
| 1.2.2 Raw and central moments | 11 |
| 1.2.3 Autocorrelation | 12 |
| 1.2.4 Power spectrum | 13 |
| 1.2.5 Integral length | 14 |
| 1.2.6 Taylor length | 15 |
| 1.2.7 Kolmogorov length | 18 |
| 2 Sensor and system design | 19 |
| 2.1 Working principle | 19 |
| 2.2 Design of the 2d-LCA of second kind | 21 |
| 2.3 Design of the 2d-LCA of third kind | 22 |
| 2.3.1 Modification with regard to stability | 22 |
| 2.3.2 Modification with regard to handling | 24 |
| 2.3.3 Modification with regard to signal quality | 28 |
| 3 Cantilever | 35 |
| 3.1 Cantilever designs and manufacturing process | 35 |
| 3.2 Mechanical and fluidic properties of cantilevers | 38 |
| 4 Calibration | 47 |
| 4.1 Shape of the calibration plane | 48 |
| 4.2 Accuracy of the calibration plane | 49 |
| 4.3 Optimization of the calibration process | 52 |
| 4.4 Angular range of cantilevers equipped with vanes | 53 |

| | | |
|----------|---|------------|
| 4.5 | Reproducibility of calibration planes | 55 |
| 5 | Measurements | 61 |
| 5.1 | Measurements in the wake of a cylinder | 61 |
| 5.2 | Flow with extreme angle of attack | 77 |
| 5.3 | Measurements in the wake of a large grid | 82 |
| 6 | Outlook and Summary | 89 |
| A | Influence of the anemometer housing upon the flow | 93 |
| B | Labview program for automated calibration | 95 |
| C | Adjusting of the Laser | 97 |
| C.1 | Alignment of the laser | 97 |
| D | Characteristics of 2d-PSDs | 99 |
| D.1 | Functionality of a 2d-PSD | 99 |
| D.2 | Position resolution of the 2d-PSD | 100 |
| D.3 | Response speed | 101 |
| E | Experimental setup for the estimation of Q-factors and resonance frequencies | 103 |
| F | Allocation of measured data | 107 |
| G | Lead and connector pin assignment | 109 |
| H | Circuit diagrams | 111 |
| I | Technical drawings | 117 |
| | Curriculum | 137 |
| | List of publications | 139 |

List of Figures

| | | |
|------|---|----|
| 1 | Photography of four 2d-LCAs. | 3 |
| 1.1 | Different regimes in a turbulence spectrum $E(f)$ associated with turbulence for a range of frequencies f | 6 |
| 1.2 | Autocorrelation with osculating parabola and detailed view of the fit for small τ (in terms of Samples). | 16 |
| 1.3 | Development of eqn. (1.26). Small values of r are approximated using a 2nd order polynomial fit. | 17 |
| 2.1 | Schematic illustration of the deflection of the reflected spot due to bending (a) and twisting (b) of the cantilever. | 20 |
| 2.2 | Sectional drawing of the 2d-LCA of second kind showing the main components (a,b) and view of the housing (c). | 21 |
| 2.3 | Sectional drawing of the 2d-LCA of third kind showing the main components (a) and view of the housing (b). | 23 |
| 2.4 | Arrangement of the optical components in the 2d-LCA of second kind (a) and in the 2d-LCA of third kind (b). | 25 |
| 2.5 | Alignment station for attaching the cantilever to the cantilever arm (a). The enlarged sections (b) and (c) show the spring-loaded mechanism that is used to clamp the cantilever chip. . . | 26 |
| 2.6 | Closer view at part #9 and part #10 from two different perspectives. | 27 |
| 2.7 | Photograph of the cardan shafts alone (a) and in installed state (b). | 27 |
| 2.8 | Photograph of the front and back of the central unit with descriptions of the main functions. | 28 |
| 2.9 | Photograph of the circuit board (front and back side) used for the 2d-LCA of third kind. | 30 |
| 2.10 | Circuit for transformation of the current signals provided by the 2d-PSD into amplified voltage signals. | 31 |

| | | |
|------|--|----|
| 2.11 | Comparison between the 2d-LCA of second kind (blue) and the 2d-LCA of third kind (black) in terms of spectra without light on the 2d-PSD (a, d), spectra of a turbulent signal (b, e) and a section of the corresponding time series (c, f). The plots were produced using the respective voltage signals of the x-component of each 2d-LCA. The measurements for the plots in (b, c, e, f) were conducted under same conditions and with same cantilever. | 33 |
| 2.12 | The graph represents the x-signal of the electronics for a sinusoidal excitation at I_1 in the range of 400Hz-250kHz. The other three inputs of the electronics (I_2, I_3, I_4) are fed with constant DC-signals. The dashed lines correspond to a -3db decay in gain with regard to the voltage output at 100Hz. Therefore, the cut-off frequency is about 146kHz. | 34 |
| 3.1 | Redesigned cantilever chip with magnification of the cantilever with vane (highlighted in yellow) and the root section (highlighted in red). | 36 |
| 3.2 | Cantilever with a Ni-vane (left) and first prototype of a SU-8 vane built on a substrate (right). | 37 |
| 3.3 | Architecture of the cantilever chip (side view). | 37 |
| 3.4 | Contaminated reflection pad (a) and a clean reflection pad (b). | 38 |
| 3.5 | c_d -values for a one-sidedly fixed rectangular plate with length / width-ratio of 4:1 obtained from CFD-simulations (black dots) and curve fit according to $c_d \approx 5.73/u + 1.3$ (red line). | 39 |
| 3.6 | Drag force upon the cantilever considering $c_d(u)$ as obtained from fig. 3.5 (black) and a constant $c_d = 1.52$ (red). | 40 |
| 3.7 | Simulated deflection distances along the x-direction of a 2d-PSD with side length of 4mm for velocities of 1-30m/s for cantilevers of $140\mu\text{m}$, $160\mu\text{m}$ and $180\mu\text{m}$ in length. The total light intensity must remain within the grey area in order to be detected by the 2d-PSD entirely. | 41 |
| 3.8 | Sweep frequency against excitation amplitude for a cantilever of $140\mu\text{m}$ in length with vane (green) and a cantilever of same length but without vane (orange). | 43 |
| 3.9 | Evolution of the amplitude for a cantilever of $160\mu\text{m}$ in length without vane at different pressures. The corresponding Q-factors are found in the legend. | 45 |
| 3.10 | Simulation of th first three resonant modes for a cantilever of $160\mu\text{m}$ in length and with a vane of $50\mu\text{m}$ in height. | 46 |

| | | |
|------|--|----|
| 4.1 | Setup for the calibration of the 2d-LCA. | 48 |
| 4.2 | Calibration plane for a cantilever of $160\mu\text{m}$ in length and a vane of $50\mu\text{m}$ in height. | 49 |
| 4.3 | Calibration planes obtained with a cantilever of $140\mu\text{m}$ in length and a vane of $50\mu\text{m}$ in height for different orientations that correspond to -9° , -3° , 0° , $+3^\circ$ and $+9^\circ$ with respect to the lengthways axis of the 2d-LCA (red dashed line). | 50 |
| 4.4 | Calibration plane for a cantilever of $160\mu\text{m}$ in length without vane. | 51 |
| 4.5 | Standard deviations for the three lowest velocities of calibration planes by a cantilever with vane (a) and without vane (b). | 52 |
| 4.6 | Calibration planes recorded with the following step sizes for velocities and angle of attack: 0.5m/s and 1° (a), 1m/s and 1° (b), 1m/s and 3° (c) and 1m/s and 5° (d). | 53 |
| 4.7 | Calibration plane for a cantilever of $160\mu\text{m}$ in length and a vane of $50\mu\text{m}$ in height (a) and without a vane (b) for an angular range of $\pm 90^\circ$ | 54 |
| 4.8 | Calibration plane for a x-wire (Dantec 55p51) for an angular range of $\pm 30^\circ$ (a) and for $\pm 90^\circ$ (b). | 55 |
| 4.9 | Three calibrations by the same cantilever recorded in intervals of half hour. | 56 |
| 4.10 | Deviations between two calibrations with the 2d-LCA in terms of velocities (a) and inflow angle (b). | 57 |
| 4.11 | Three calibrations with the same x-wire recorded in intervals of half hour. | 58 |
| 4.12 | Deviations between two calibrations with the x-wire in terms of velocities (a) and inflow angle (b). | 58 |
| 5.1 | 10.000 raw data points of each anemometer (2d-LCA with vane (a), 2d-LCA without vane (b) and x-wire (c)) plotted in the corresponding calibration plane. | 63 |
| 5.2 | Time series of 1000 samples for the absolute value of the velocity measured by all three anemometers. | 64 |
| 5.3 | Time series of 1000 samples for the angle of attack measured by all three anemometers. | 64 |
| 5.4 | Autocorrelation functions of all three anemometers for the longitudinal velocity signal. | 66 |
| 5.5 | Spectral densities of all three anemometers for the longitudinal velocity signal. | 66 |
| 5.6 | Spectral densities of all three anemometers for the transverse velocity signal. | 67 |

| | | |
|------|--|----|
| 5.7 | Spectral densities for the absolute value of the velocity. The black lines indicate a -5/3 and a -2 slope. | 68 |
| 5.8 | PDFs of increments for the longitudinal velocity component for the 2d-LCA with vane (black), the 2d-LCA without vane (blue) and the x-wire (red) for $\tau_1=0.167\text{ms}$, $\tau_2=1\text{ms}$, $\tau_3=2\text{ms}$, $\tau_4=10\text{ms}$ and $\tau_5=0.1\text{s}$ (from top to bottom). | 69 |
| 5.9 | PDFs of increments for the transverse velocity component for the 2d-LCA with vane (black), the 2d-LCA without vane (blue) and the x-wire (red) for $\tau_1=0.167\text{ms}$, $\tau_2=1\text{ms}$, $\tau_3=2\text{ms}$, $\tau_4=10\text{ms}$ and $\tau_5=0.1\text{s}$ (from top to bottom). | 70 |
| 5.10 | Formparameter (a), skewness (b) and kurtosis (c) for the longitudinal velocity increments against τ for all three anemometers. | 71 |
| 5.11 | Formparameter (a), skewness (b) and kurtosis (c) for the transverse velocity increments against τ for all three anemometers. | 72 |
| 5.12 | Longitudinal (a) and transverse (b) structure functions of order $p = 1, 2, 3, 4$ (from bottom to top) for all anemometers. | 73 |
| 5.13 | Structure functions of different orders p against the third structure function for the 2d-LCA with vane (a) and corresponding fit according to eqn. (1.9) (b). | 74 |
| 5.14 | Structure functions of different orders p against the third structure function for the 2d-LCA without vane (a) and corresponding fit according to eqn. (1.9) (b). | 74 |
| 5.15 | Structure functions of different orders p against the third structure function for the x-wire (a) and corresponding fit according to eqn. (1.9) (b). | 75 |
| 5.16 | Transverse structure functions of different orders p against the third longitudinal structure function with rescaled τ for the 2d-LCA with vane (a) and corresponding fit according to eqn. (1.9) (b). | 75 |
| 5.17 | Transverse structure functions of different orders p against the third longitudinal structure function with rescaled τ for the 2d-LCA without vane (a) and corresponding fit according to eqn. (1.9) (b). | 76 |
| 5.18 | Transverse structure functions of different orders p against the third longitudinal structure function with rescaled τ for the x-wire (a) and corresponding fit according to eqn. (1.9) (b). | 76 |
| 5.19 | Histogram of the angle of attack for the 2d-LCA (green) and the x-wire (red). | 78 |
| 5.20 | Spectral densities of the angle of attack for the 2d-LCA (green) and the x-wire (red). | 79 |

| | | |
|------|--|----|
| 5.21 | Spectral densities of the absolute value of velocity for the 2d-LCA (green) and the x-wire (red). | 79 |
| 5.22 | Increment PDFs for the angle of attack for the 2d-LCA (green) and the x-wire (red) with $\tau_1=0.167\text{ms}$, $\tau_2=0.333\text{ms}$, $\tau_3=1\text{ms}$, $\tau_4=1.667\text{ms}$ and $\tau_5=16.667\text{ms}$ (from top to bottom). Solid lines represent fits of the PDFs. The distributions corresponding to τ_{1-4} were fitted according to eqn. (1.18) and the distribution corresponding to τ_5 was fitted using a Gauss. | 80 |
| 5.23 | Course of the form parameter for the 2d-LCA (green) and a x-wire (red). | 81 |
| 5.24 | PDFs of increments for the absolute value of velocity for the 2d-LCA (green) and the x-wire (red) for $\tau_1=0.167\text{ms}$, $\tau_2=0.333\text{ms}$, $\tau_3=1\text{ms}$, $\tau_4=1.667\text{ms}$ and $\tau_5=16.667\text{ms}$ (from top to bottom). Solid lines represent fits of the PDFs. The distributions corresponding to τ_{1-4} were fitted according to eqn. (1.18) and the distribution corresponding to τ_5 was fitted using a Gauss. | 81 |
| 5.25 | Measurement setup in the S1 wind tunnel at the ONERA facility. Several anemometers are mounted to a rack in a distance of 15.36m behind the grid. The positions of the 2d-LCA, the sensor prototype and the hot wire are highlighted. The magnified area shows the installation of the 2d-LCA. | 83 |
| 5.26 | 2d-LCA mounted to a mobile calibration unit during the measuring campaign at the ONERA S1 wind tunnel. | 84 |
| 5.27 | Time series for the absolute value of the velocity measured with the 2d-LCA (green), hot wire (red) and sensor prototype (purple). The time series correspond to 0.1ms for each anemometer. | 85 |
| 5.28 | Energy spectra obtained from the 2d-LCA (green), hot wire (red) and sensor prototype (purple). The black line indicates a slop of $-5/3$ | 86 |
| 5.29 | Section of filtered time series at 50kHz for the absolute value of the velocity measured with the sensor prototype. The time series corresponds to 0.1ms. | 86 |
| 5.30 | PDFs of increments for the absolute value of the velocity for the 2d-LCA (green), the hot wire (red) and the sensor prototype (purple) for $\tau_1=0.05\text{ms}$, $\tau_2=0.15\text{ms}$, $\tau_3=2\text{ms}$, $\tau_4=20\text{ms}$ and $\tau_5=0.1\text{s}$ (from top to bottom). | 88 |
| 6.1 | New design of a cantilevers with “v”-shaped and “hat”-shaped vanes. | 92 |

| | | |
|-----|---|-----|
| 6.2 | Area of attack provided by a simple vane (blue), “v”- or “hat”-shaped vane with 15° between both sides (red) and 45° between both sides (green). | 92 |
| A.1 | Standard x-wire calibration (a) for 4-12m/s and inflow angle of $\pm 90^\circ$ and a calibration obtained from the same x-wire built into a LCA-housing (b). Black error bars indicate the standard deviations for each calibration points. | 94 |
| B.1 | Screenshot of the LabVIEW user interface for performing automated calibrations. | 96 |
| C.1 | Diffraction patterns in the forward scattered light for different positions of the laser along the chip. The positions indicated are from the perspective of the laser beam. | 98 |
| E.1 | Two cantilever chips prepared and terminated for electrostatic excitation (a) and side view of the cantilever above the silicon block (b). The alternating current for driving the cantilevers is applied between A and B (upper cantilever) or A and C (lower cantilever). | 104 |
| E.2 | Photograph of the vacuum chamber and schematic illustration of the setup. | 104 |
| E.3 | Size of the laser spot in proportion to the cantilever. | 105 |
| F.1 | Calibration points plotted against velocity (a) and angle of attack (b). | 107 |
| F.2 | Interpolated points (blue) using Akima-splines for the data sets representing velocities (a) and angle of attack (b). | 108 |
| H.1 | Circuit diagram for the processing of the 2d-PSD-signals. . . . | 113 |
| H.2 | Main circuit diagram for the amplification and filter section of the central unit. | 114 |
| H.3 | Circuit diagram for the power supply used in the central unit. . | 115 |

Introduction

In fluid dynamics, the word turbulence describes a state of no order. It is derived from the Latin word "turbare", which is often translated as disorder, confusion and disruption. When describing atmospheric and laboratory flow conditions, turbulence is referred to as a state in which streamlines of the propagating flow cross or lose their parallelism. In contrary, a perfect flow situation in which this disorder never occurs is called laminar. Typical examples of turbulent flows are vortices in the wake of bluff bodies or mixing processes of fluids.

Scientists and engineers invest a lot of effort in order to study turbulent flows. The reason is simply its leading role in a wide range of natural and industrial processes. In this manner, it is of tremendous practical importance for the prediction of weather events and ocean circulation, but also for the estimation of heat transfer in technical processes and drag calculation in pipe flows [2]. It is quite likely that a better knowledge and hence more control of this phenomenon will have a positive impact on various areas of our daily life.

The acquisition of turbulent flows is a big challenge in experimental fluid mechanics. This is because in a turbulent flow field the energy of the moving fluid is distributed over a wide range of scales, i.e. very large and very small vortices coexist. The difference between their length scales can be orders of magnitude. In addition, turbulent flows respond very sensitive towards small perturbations and thus are difficult to be reproduced in the laboratory. Because of this highly irregular and non-linear nature a deep investigation is difficult to the present day and has been challenging scientists for centuries. An example for the early interest in turbulence is a detailed drawing by Leonardo da Vinci of a water jet immersed into a basin from the 15th century [1]. It shows the existence of water whirls of various sizes together with highly irregular flow areas.

Today, there are two main ways for getting insight into a turbulent flow, namely by means of measurement techniques or by computational simulations. The computational approach is usually limited by computer memory. For direct numerical simulation (DNS) that is used to solve the Navier-Stokes-equations for real-live cases without any simplifications the computational costs scale with Re^3 [11]. This is because solving the turbulent flow entirely requires resolving

largest scales at resolution of the lowest scales. Moreover, besides the spatial resolution an infinite time resolution would be necessary. Up to today, computational power is not efficient enough to simulate flows at any Reynolds number. And even if it was, for an accurate solution by means of DNS all external factors contributing to the Navier-Stokes-equations need to be known. This is a near impossible task for a real-world experiment.

The second approach is to make use of measurement techniques. A huge variety of different anemometers have been developed with individual properties and fields of applications, but only few are suitable for resolving smallest scales, which for many typical laboratory flows are in the order of few millimeters. In some cases these scales can reach even smaller values of less than 0.1mm. Scientists that do research in these areas agree that a lack of suitable and user-friendly anemometers exists (see for instance [46]). Therefore, it is essential to further promote the development of novel measurement techniques.

In this thesis the focus is on the further development of an anemometer, which is named 2d-Laser Cantilever Anemometer (2d-LCA, fig. 1). It has been designed for high resolved measurements in turbulent flows generated under laboratory conditions. The term “high resolved” combines two parameters, namely the temporal and spatial resolution. These two parameters are of great significance and determine the depth of insight into the flow to be investigated that can be achieved. The temporal resolution of a sensor is the highest sampling frequency f_s that still has a physical meaning. Depending on the kind of anemometer the temporal resolution can be restricted by physical principles like heat inertia as in the case of hot-wires. On the contrary, the spatial resolution specifies the minimum dimension of a turbulent structure that can be detected. For intrusive anemometers the spatial resolution is always equal to either the sensing element, or for anemometers with multiple sensing elements, the volume spanned by those. In the literature there is no clear definition for a highly-resolving or low-resolving sensor. Therefore, for clarity reasons the terms “high resolution” or “high resolved” will from now on refer to spatial resolutions in the range of millimeters or smaller and temporal resolutions in the order of tens of kHz.

In the range of existing measurement techniques in fluid mechanics the 2d-LCA possesses characteristics (particularly spatial and temporal resolution) comparable to x-wires. However, it is based on a different measuring principle, which is adopted from atomic force microscopes. Still, it is suited to complement or even replace hot-wire anemometry depending on the field of application as will be shown in the course of this thesis.

For decades, hot-wires have contributed massively to experimental research in fluid mechanics. However, as any other sensor, hot-wires have restrictions and can be operated in a certain well-defined framework only. Limitations for hot-



Figure 1: Photography of four 2d-LCAs.

wire anemometry exist at very low velocities of typically $v < 1m/s$ as natural convection triggered by buoyancy forces distorts the effect of forced heat convection. This effect becomes even more significant for larger overheat ratios [12]. On the contrary, for large velocities $v > 50m/s$ the calibration function causes noticeable detrimental effects on the resolution power. Further limitations may also be due to the field of operation and especially the fluid in which measurements are performed. Thus, fluids need to be in gaseous form and clean of liquid droplets or particles that could destroy the wire. In [34] difficulties with measurements of snow-laden flows are discussed. Furthermore, as hot-wires are part of an amplifier circuit they very likely pick up electromagnetic noises from the environment, which can strongly affect the measured data [37]. A lot of attention must also be paid when performing measurements very close to walls. Heat reflections from the wall can alienate the signal and result in misinterpretation.

Regarding the directional acceptance ranges, x-wires detect inflow angle up to $\pm 45^\circ$ in theory ^a. This range is insufficient for some experiments. Lastly, the flow character itself imposes a further constraint. As each hot-wire of a probe measures the absolute value of velocity only, reversal and incoming flows are equally interpreted (rectification error).

The working principle used in 2d-LCA does not encounter the above-mentioned restrictions. Thus, it can be used in any transparent fluid (also liquids and particle-laden fluids) and does not suffer from heat-related effects such as convection or reflection ^b. The sensing element of the 2d-LCA is optically isolated from any electronics and is therefore not sensitive towards disturbances caused by noise. Moreover, as will be shown in this thesis the acceptance range for inflow angle can be significantly larger in comparison to x-wires.

^aAs the presence of the prongs becomes more dominant towards the boundaries of this range, the real acceptance region can be actually smaller.

^bLarge temperature gradients may cause unwanted diffraction of the laser beam.

Following the accomplishments achieved in [34, 37, 32, 36], this thesis shall present the newest improvements and challenges of the development process of the 2d-LCA.

Structure of this thesis

The opening chapter of this thesis gives an insight into the prevailing turbulence theory, which is mainly based on the work of L. F. Richardson and A. N. Kolmogorov. This introduction is followed by an overview of statistical tools and concepts that are applied for the characterization of measured data with the 2d-LCA and reference anemometers.

The second chapter focuses on the working principle of the 2d-LCA. Here, it is explained how simultaneous measurements of two velocity components are achieved. The design of the sensor itself together with the latest improvements concerning stability, handling and signal quality is presented in chapter 3. This chapter also addresses the differences between an older prototype of the 2d-LCA and the newest version.

In the fourth chapter, a detailed characterization of the cantilevers used in this thesis is given. At first, the design and the architecture of the cantilevers are discussed. This is followed by an inspection of the mechanical properties including analytic and experimental approaches.

The fifth chapter discusses the calibration planes produced by the 2d-LCA with different kind of cantilevers. Here, the emphases are placed on the shape, accuracy and reproductibility of the calibrations. In addition, the main differences between calibration planes produced by the 2d-LCA and by commercial x-wires are discussed. Lastly, the influence of the mesh-size used for producing a calibration plane is studied with the aim to optimize the calibration process.

Next, in chapter 6 measurements conducted with the 2d-LCA and other reference anemometers are analyzed. Altogether, three experiments are presented. These include velocity measurements in turbulent wake flow generated by two different cylinders and a grid. All experiments feature different conditions and aim to compare the performance of the 2d-LCA with other anemometers.

Finally, chapter 7 gives an outlook and summarizes the work done in this thesis.

Chapter 1

Basic concepts and statistical description

Velocity data obtained from measurements in turbulent flows are evaluated using statistical tools. In the following, a brief overview of concepts that are used in this thesis will be given. A detailed inspection and derivation is found in the standard literature on turbulence, for instance [11, 6, 20, 24].

1.1 Turbulence theory

The most famous model for describing turbulent flows was proposed by Lewis Fry Richardson in 1922 [5]. According to his idea, the energy in a turbulent flow is fed into the system at large spatial scales L and is then transferred to increasingly smaller scales in a cascade-like process until the presence of viscosity becomes perceptible and finally dissipation takes place at scales η . Thus, there is a continuous energy flux ε being transferred within a hierarchy of vortex sizes. Richardson's model is widely accepted, although a proof of properness has not yet been presented [6, 7]. As a matter of fact, it raises several doubts. Thus, it assumes ε to be constant at all times and does not allow for energy transformation in upscale direction or skipping of scales [8].

Still, despite some disagreements Richardson's model provides the basis for a famous work on turbulence theory, which was published in 1941 by A. Kolmogorov [9] (also often referred to as K41). The core conclusions of K41 state that: 1. For high Reynolds numbers the energy flux ε , which is equivalent to the energy dissipation rate, is independent of the viscosity ν of the fluid. 2. As energy is transferred within the cascade process, vortices lose their directional biases towards smaller scales. At scales of the order of η the small-scale motions are statistically homogenous, isotropic and without any inherited ge-

ometrical information from their decent eddies for any driving scale L . This universal behavior of small-scale turbulence leads to the presumption that its statistics depend on ε and ν only.

The quantity η is of major practical importance because it identifies the spatial dimension on which complete dissipation takes place within turbulent flows. Structures of size smaller than η do not exist. A turbulent flow that is said to be fully developed is characterized by a range of scales that separates L from η . This range is referred to as the inertial range. Fig. 1.1 gives an illustrative overview of all the scales discussed in this section on the basis of a power spectrum.

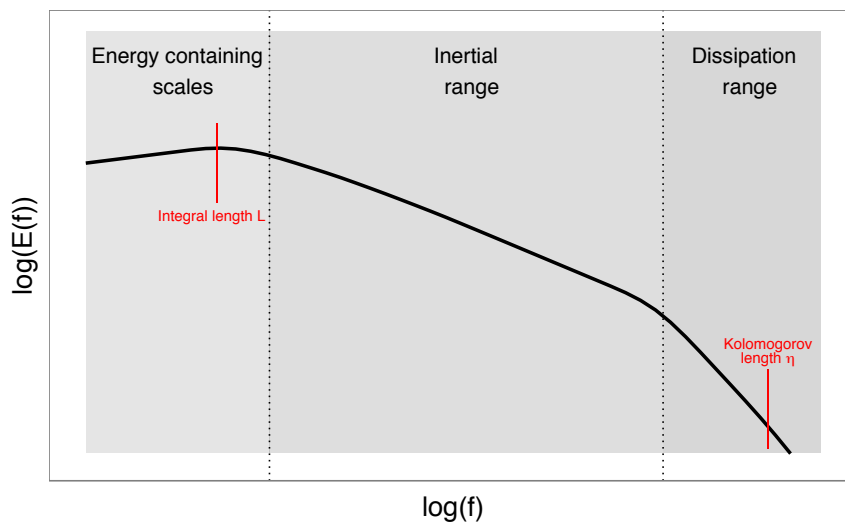


Figure 1.1: Different regimes in a turbulence spectrum $E(f)$ associated with turbulence for a range of frequencies f .

Intrusive 2d-anemometers (like the 2d-LCA or x-wires) perform velocity measurements at one point of the flow only. In order to assess it on the whole, one might think that it is necessary to simultaneously and continuously measure its velocity vector at every position. However, this is not necessarily the case. As the temporal progression of turbulent flows is not repeatable in nature or in the laboratory, the stochastic properties are of bigger importance than the precise course of the flow [19]. Assuming fully developed turbulent flows moving with a mean velocity, it is sufficient to measure the velocity vector $u(t)$ at only one spatial position within the flow (Eulerian measurement) in order to obtain a representative velocity statistic. It is assumed that the mean velocity \bar{u} of the flow is high enough for the turbulent structures to pass by the sensor without any relevant changes as long as the turbulence intensity $TI = u'_{rms}/\bar{u}$ is below roughly

10%, with $u' = u - \bar{u}$ [45, 11]. Figuratively speaking, in that case the turbulence pattern with all its vortices is "frozen" and moves as one static formation. This idea has been proposed by G. I. Taylor and is named Taylor's hypothesis of frozen turbulence. Therefore, instead of measuring at various positions, one can restrict the sensor position to one point and measure in the time domain. Expressed mathematically, Taylor's hypothesis reads:

$$-\bar{u} \frac{\partial u}{\partial x} = \frac{\partial u}{\partial t}. \quad (1.1)$$

In the 18th century George G. Stokes and Osborne Reynolds introduced a dimensionless quantity, the so-called Reynolds number Re , that places inertial forces in relationship to viscous forces within a fluid. Hence, Re is given by:

$$Re = \frac{uL_c}{\nu}, \quad (1.2)$$

with the flow velocity u and the kinematic viscosity ν . L_c is a characteristic length depending on the flow setup. From the relation the decrease of the stabilizing and smoothing effect of viscosity with growing Re becomes immediately evident. Although L_c is somewhat loosely defined, in many laboratory setups the length to be chosen is quite obvious. Thus, for instance L_c is the diameter of a pipe when characterizing pipe flows, or in the case of wake flows, the width of the wake-generating body. Many authors agree to a rough classification, that characterizes a laminar flow at $Re \approx 1$ and a turbulent flow at $Re \gg 1$. The transition between these two regimes is also depending on the boundary conditions and setup related properties, e.g. surface roughness of flow channels.

Two individual flow situations behave similar if their Re and the boundary conditions match. Because of that, conclusions from experiments with small setups, like models of wind turbine airfoils, can be drawn for life-sized problems [38]. Another way of characterizing states of flow is to make use of the Taylor Reynolds Number Re_λ , that depends on intrinsic properties of the flow only. It is defined as:

$$Re_\lambda = \frac{\lambda \sigma}{\nu}. \quad (1.3)$$

Here λ is the Taylor's microscale and σ the standard deviation of the flow velocity. λ is the length scale, at which the impact of dissipation becomes rife and will be discussed in more detail in section 1.2.6.

1.2 Stochastic tools and length scales in turbulent flows

1.2.1 Structure functions

Kolmogorov's K41 and K62 theories for characterization of homogeneous and stationary turbulence are based on the statistical investigation of structure functions, which are defined in terms of velocity increments. Velocity increments may be generated in the temporal or spatial domain. In both cases only the difference between two velocities is considered. For the analysis in accordance with K41 mostly longitudinal velocity increments $u_{x,\tau}(t)$ are considered. Its definition is given by:

$$u_{x,\tau}(t) = u_x(t) - u_x(t + \tau). \quad (1.4)$$

Here, τ is the separation time between two velocities. As t does not matter for stationary turbulence, $u_{x,\tau}(t)$ can be expressed as $u_{x,\tau}$ or for the sake of simplification as u_τ . The raw moments of velocity increments are called structure functions $S_u^p(\tau)$ and are defined as:

$$S_u^p(\tau) = \langle (u_x(t) - u_x(t + \tau))^p \rangle = \langle u_\tau^p \rangle. \quad (1.5)$$

In order to transfer u_τ into velocity increments based on spatial scales, i.e. real separation distances r , Taylor's hypothesis of frozen turbulence may be applied (see section 1.1). A notation for structure functions in spatial domain is given by:

$$S_u^p(r) = \langle (u_x(x+r) - u_x(x))^p \rangle = \langle u_r^p \rangle. \quad (1.6)$$

The essential hypothesis of the K41 theory is that for $\eta \ll r \ll L$, the structure functions scale with:

$$S_u^p(r) = C_p \bar{\varepsilon}^{\frac{p}{3}} r^{\frac{p}{3}} \propto r^{\frac{p}{3}}. \quad (1.7)$$

Here, C_p is a universal constant and $\bar{\varepsilon}$ is the mean dissipation rate that is assumed to be prevailing in Richardson's model of turbulence cascades. This relation has been derived from dimension analysis using the first core conclusion of K41 and thus is valid within the inertial range only. For that, Kolmogorov combined the quantities ε and r in such a way to meet the dimensions of $S_u^p(r)$. As discussed in section 1.1, the assumption to regard ε as a uniformly dis-

tributed quantity is unfounded and as a consequence the relation in eqn. (1.7) cannot be accurately reproduced in experiments for $p > 3$. The reason for this is that ε is differently concentrated throughout the flow. To correct for this, the K41 theory has been refined by Kolmogorov himself and Obukhov in [22] by introducing a log-normal distribution for ε , which describes the decay process in a more appropriate way. In a log-normal distribution the logarithms of a quantity are normally distributed. Thus, the model introduces an intermittent behavior for ε . Based on this correction, the scaling of structure functions with r is complemented according to:

$$S_u^p(r) = C_p \bar{\varepsilon} r^{\zeta_p}, \quad (1.8)$$

where

$$\zeta_p = \frac{p}{3} - \frac{\mu}{18} p(p-3). \quad (1.9)$$

This relation holds for $3 \leq p \leq 8$ only and becomes increasingly imprecise towards higher p ^a. The quantity μ is called the intermittency factor and is a universal constant that is determined experimentally. Scaling relations of structure functions are useful for the estimation of the energy dissipation rate and the extent of the inertial range [23].

One of the most important laws in fully developed turbulence arises from the 3rd structure function $S_u^3(r)$ for the longitudinal velocity increments, which satisfies the relation:

$$S_u^3(r) = -\frac{4}{5} \bar{\varepsilon} r. \quad (1.10)$$

Eqn. (1.10) is referred to as the -4/5-law and can be derived directly from the Navier-Stokes-equations. It is of significant importance because it is one of a few non-trivial and exact laws in fully developed turbulence that has been obtained so far [6].

The existence or the extent of an inertial range within a set of measured data is often verified by means of a scaling law when plotting $S_u^3(r)$ against r in a log-log plot. Because of the logarithmic axis the scaling exponent ζ_3 becomes a straight line within the region that corresponds to the inertial range. Here, the flow is said to be self-similar. However, for many data sets obtained from

^aFor $p > 8$ the relation in eqn. (1.8) becomes very sensitive towards extreme events, which will scale with an exponent of p and thus dominate the mean value. Therefore, for a representative relation, a huge amount of data is needed.

experiments the inertial range and thus the region where a scaling law can be applied is too small in order to deduce ζ_3 with a small statistical error.

In [43] a method is described that allows for determining ζ_p for flows with small or even not-existing inertial ranges. The method is referred to as extended-self similarity (ESS) and is based on scaling laws between structure functions of different orders $q \neq p$. In [43] it is exemplarily shown that a wide scaling law exists between $S_u^2(r)$ and $S_u^3(r)$ and also between $S_u^6(r)$ and $S_u^2(r)$. In the range where this scaling law holds, a relation according to:

$$(1.11)$$

holds. The relative scaling exponent ζ_q/ζ_p is immediately apparent from a log-log plot. The most comfortable way is to apply this method for $p = 3$ and thus $\zeta_p = 1$. That way the relative scaling exponent is simply ζ_q .

The same approach can be applied for the transverse structure functions. However, in [25, 49] it has been found that the transverse cascade process of the turbulent decay is faster than the longitudinal cascade by a factor of 3/2. Thus, for a qualitative comparison of the transverse and longitudinal scaling exponents this difference must be taken into account when generating the transverse structure functions $S_{t,u}^p(\tau)$. This is done by rescaling the time lag τ accordingly. Thus, the transverse structure function becomes:

$$S_{t,u}^p(\tau) = \langle (u(t) - u(t + \frac{2}{3}\tau))^p \rangle. \quad (1.12)$$

The factor of 3/2 is derived from the Karman equation

$$S_{t,u}^2(\tau) = S_u^2(\tau) + \frac{\tau}{2} \frac{\partial S_u^2(\tau)}{\partial \tau}, \quad (1.13)$$

which is interpreted as the Taylor expansion of $S_u^2(\tau) + \frac{\tau}{2} \frac{\partial S_u^2(\tau)}{\partial \tau} \approx S_u^2(\tau + 1/2\tau) = S_u^2(3/2\tau)$. In [25, 49] it has been shown that this rough approximation fits well to experimental observations.

The analysis of scaling exponents of rescaled transverse structure functions is known as the extended-self similarity hypothesis for transverse structure functions (ESST).

1.2.2 Raw and central moments

Raw moments (or moments around zero) for an arbitrary quantity X are defined as $\langle X \rangle^p$, with p being a natural number that specifies the order. The first raw moment is the mean or the expected value of X . For a statistically independent quantity the expected value is determined by the ensemble average. Statistically independence is ensured if either N independent experiments are performed at the same time or if X is a random variable that is observed in one experiment at different times n . The ensemble average is given by:

$$\langle X \rangle = \lim_{N \rightarrow \infty} \frac{1}{N} \sum_{n=1}^N X_n. \quad (1.14)$$

Here, n is the index for each individual observation. Since the condition $N \rightarrow \infty$ cannot be fulfilled in an experiment, $\langle X \rangle$ is approximated by the arithmetic mean.

Higher-order raw moments are found not to have much meaning in statistical description of turbulence and therefore are rather unimportant.

Much more interesting are the moments around the mean, the so-called central moments. These are defined as $\langle (X_n - \langle X \rangle)^p \rangle$. The first central moment, i.e. $\langle (X_n - \langle X \rangle)^1 \rangle$, is zero. The second central moment is referred to as the variance $\text{var}(X) = \langle (X_n - \langle X \rangle)^2 \rangle = \sigma^2$, which is also the square of the standard deviation σ .

Normally or Gaussian distributed values of X depend on the mean value and the second central moment only. The corresponding probability density function (PDF) is given by:

$$B(X) = \frac{1}{\sigma\sqrt{2\pi}} \exp\left(-\frac{(X_n - \langle X \rangle)^2}{2\sigma^2}\right). \quad (1.15)$$

Other higher order central moments are also defined and give further information on the distribution of X . It is common to use the third and the fourth central moments for visualizing the shape of a PDF. Thus, the third central moment specifies the skewness S , which is related to an asymmetry of a PDF. Positive values of S indicate a stronger spreading of X towards positive values and also result in longer tails on the positive side. In accordance, negative S indicate a stronger pronunciation of the negative region of the PDF. The skewness is normalized and expressed as:

$$S = \frac{\langle (X_n - \langle X \rangle)^3 \rangle}{\langle (X_n - \langle X \rangle)^2 \rangle^{3/2}}. \quad (1.16)$$

The fourth central moment is related to the kurtosis K . PDFs with higher values of K are characterized by a stronger pronounced peak around its mean value, whereas low values of K generally correspond to a wider distribution around the mean. In normalized form K is given by:

$$K = \frac{\langle (X_n - \langle X \rangle)^4 \rangle}{\langle (X_n - \langle X \rangle)^2 \rangle^2}. \quad (1.17)$$

Gaussian PDFs have no skewness ($S = 0$) and a kurtosis of $K = 3$.

The intermittent character as introduced in K62 by the log-normal distribution of ε is reflected in the PDF of increments $B(u_r)$, which shows a higher probability for large events when compared to a Gaussian distribution. A model introduced in [30] assumes $B(u_r)$ to be a superposition of individual Gaussian distributions $p(u_r | \sigma)$ of fixed r and standard deviations σ that are log-normally distributed. Thus, the PDF is given by:

$$B(u_r) = \frac{1}{2\pi\lambda_f} \int \exp\left(-\frac{\ln^2(\sigma/\sigma_0)}{2\lambda_f^2}\right) \exp\left(-\frac{u_r^2}{2\sigma^2}\right) \frac{d(\ln\sigma)}{\sigma}. \quad (1.18)$$

σ is related to the energy transfer rate ε by $\sigma \sim (r\varepsilon)^{1/3}$ and it can be concluded that ε follows a log-normal distribution. Of particular interest in eqn. (1.18) is the parameter λ_f that determines the form of the probability density function. It is referred to as the form parameter and can be calculated according to [35] using:

$$\lambda_f^2 = \ln\left(\frac{\langle u_r^4 \rangle}{3 \langle u_r^2 \rangle^2}\right). \quad (1.19)$$

For $\lambda_f \rightarrow 0$, eqn. (1.18) becomes eqn. (1.15) again. The quantity σ_0 is the maximum of the log-normal distribution and thus the most probable standard deviation on r .

1.2.3 Autocorrelation

Instead of using structure functions for the analysis of turbulent flows, one could also use autocorrelation functions. In fact, both approaches contain the same amount of information and can be seen as equivalent. For example, the second order structure function can be transformed into a notation in terms of the

autocorrelation coefficient $R(r)$:

$$S_u^2(r) = 2 \langle u'^2 \rangle (1 - R(r)) \quad (1.20)$$

with $u' = u(x) - \langle u(x) \rangle$ and $R(r)$ being defined as:

$$R(r) = \frac{\langle u'(x)u'(x+r) \rangle}{\langle (u(x) - \langle u(x) \rangle)^2 \rangle} = \frac{\langle u'(x)u'(x+r) \rangle}{\text{var}(u(x))} = \frac{\langle u'(x)u'(x+r) \rangle}{\langle u'^2 \rangle}. \quad (1.21)$$

As can be seen, $R(r)$ is related to the second structure function only and thus does not provide any information about intermittency or non-Gaussianity.

Depending on the quantity of interest, an analysis based on autocorrelation or structure functions is preferred. One example for a quantity that is directly obtained from the autocorrelation function is the integral length L (see also section 1.25).

The connection between $R(r)$ and the power spectrum $E(k)$ is given by the Wiener-Khinchin theorem, which is discussed in more detail in section 1.2.4.

1.2.4 Power spectrum

The power spectrum of a velocity time signal $u(t)$ is primarily used to estimate the dynamic range, i.e. the ratio between the weakest and the strongest signal. It is evaluated in the frequency or wave number domain and is typically represented in a log-log representation.

For fully developed turbulence, the power spectrum takes on a specific shape from which the extent of the three main regimes (as discussed in section 1.1) can be roughly estimated. Within the inertial range a relation according to Kolmogorov's two-third law (eqn. (1.7)), but in terms of energy density per unit wave number $E(k)$ with dimensions $[L^3/T^2]$ can be derived. To do so, again dimensional analysis is used. Because the wave number k and the energy dissipation rate ε have dimensions of $[L^{-1}]$ and $[L^2/T^3]$ respectively, it follows that:

$$E(k) \propto \varepsilon^{2/3} k^{-5/3}. \quad (1.22)$$

Eqn. (1.22) is called Kolmogorov's $-5/3$ -law. As solely the dimensions of ε were used in order to derive this relation, its validity is limited to the inertial range only. In a log-log plot Kolmogorov's $-5/3$ -law is recognizable as a linear scaling of the wave number or frequency with slope $-5/3$ (also see figure

1.1). Therefore, it is often used for a quick estimation of the extent of the inertial range. Lower frequent values of k that do not scale linearly pertain to the integral range, whereas higher values of k indicate the beginning of the dissipation range.

The $-5/3$ scaling of k can be also derived analytically by means of the Wiener-Khinchin theorem, which states that the Fourier transformation of the autocorrelation function $R(r)$ for a stationary random process equals the power spectrum. From eqn. (1.7) and 1.20 a relation for $R(r)$ is given by:

$$R(r) = 1 - Cr^{\frac{2}{3}}. \quad (1.23)$$

Applying the Fourier transformation yields:

$$\begin{aligned} I &= \int (1 - Cr^{\frac{2}{3}}) e^{ikr} dr \\ I &= 2\pi\delta(k) - C \int r^{\frac{2}{3}} e^{ikr} dr \\ I &= 2\pi\delta(k) - C \int \frac{kr^{\frac{2}{3}}}{k^{\frac{2}{3}}} e^{ikr} \frac{d(kr)}{r} \\ I &= 2\pi\delta(k) - Ck^{-\frac{5}{3}} \int kr^{\frac{2}{3}} e^{ikr} d(kr) \\ I &= 2\pi\delta(k) - Ck^{-\frac{5}{3}} \int \underbrace{U^{\frac{2}{3}} e^{iU}}_{=constant} dU \\ & \quad I \propto k^{-\frac{5}{3}}. \end{aligned} \quad (1.24)$$

A $-5/3$ -scaling has been found in power spectra of various types of experiments, such as measurements in tidal channels, low-temperature helium gas flows and also in CFD-simulations [6].

1.2.5 Integral length

The largest scale L within a turbulent flow, at which energy is injected, can be determined using the autocorrelation function [6, 11]. To do so, the autocorrelation coefficient $R(r)$ is evaluated for velocities with growing spatial distances r . $R(r)$ reaches a value of 0 at a distance where no correlation exists. This can be interpreted as the end of a coherent structure, i.e. a vortex. Thus, integration

over $R(r)$ yields the integral scale:

$$L = \int_0^{+\infty} R(r) dr. \quad (1.25)$$

The courses of the autocorrelations obtained from measured velocity data often have several zero-crossings (thus negative correlation at some places) and do not converge completely to zero. Specifically, that means that the integral from eqn. (1.25) for calculating the integral length L cannot be carried out because of the upper integration limit of $r \rightarrow \infty$. In order to eliminate this problem the correlation function is often fitted by means of an exponential function together with a threshold value as the upper limit.

An alternative approach uses the first zero crossing as the limit for integration. This method, however, leads to large errors if the correlation does not decay exponentially. This, for example, is the case if vortex shedding is still perceptible in wake-generated turbulent flow.

For temporal data the integral of $R(\tau)$ is carried out over $\bar{u} dt$ instead of dr (Taylor's hypothesis).

1.2.6 Taylor length

The Taylor length (or Taylor microscale) λ is the scale on which dissipation begins to take place. Length scales smaller than λ are strongly affected by viscosity and fall within the dissipation range, whereas larger scales fall within the inertial range. One method for the determination of λ from measured data has become widely accepted. The approach uses the fact that for very small r the development of the autocorrelation coefficient follows a positive curvature [21]. This curvature is present even for values of $r > \eta$, which cannot be explained with Richardson's model, nor the relation in eqn. (1.23). It is believed (see for example [11]) that this behavior is caused by the influence of dissipation. The range of the positive curvature is therefore used for estimation of the Taylor's microscale λ .

The procedure is explained using fig. 1.2 that shows a autocorrelation in terms of time intervals τ for a data set of grid-generated turbulence measured with the 2d-LCA. Within the region of positive curvature a parabola of the form $R(\tau) = 1 - \tau^2/\lambda^2$ is fitted. It rolls off the autocorrelation curve and intersects with the τ -axis at a position that corresponds to λ . The result from this method

strongly depends on the resolution of the sensor [17] and the quality of the fit. Thus, for reliable results the data should have a resolution of typically one order of magnitude smaller than λ [21].

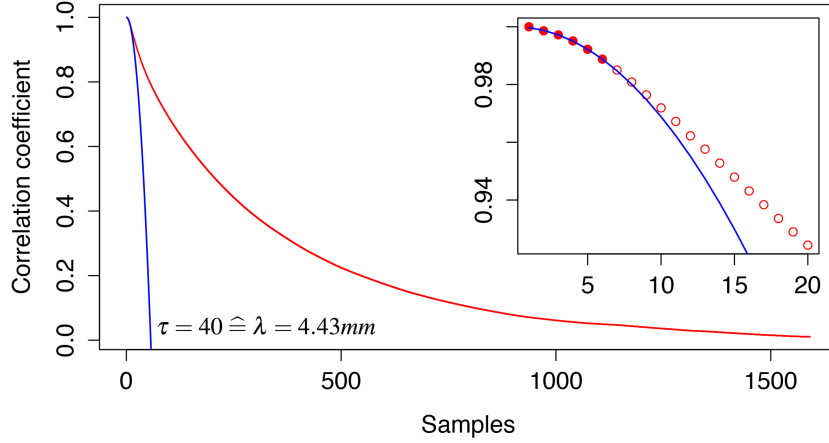


Figure 1.2: Autocorrelation with osculating parabola and detailed view of the fit for small τ (in terms of Samples).

A more robust approach for determination of λ is introduced in [29]. It uses the relation:

$$\lambda^2 = 2 \frac{\langle u'^2 \rangle}{\left\langle \left(\frac{\partial u}{\partial x} \right)^2 \right\rangle}. \quad (1.26)$$

The derivative in the denominator is determined using the difference quotient $\langle (u(x) - u(x+r))^2 \rangle / r^2 = \langle u_r^2 \rangle / r^2$ for spatial lags r that are larger than the dimensions of the sensor. Smaller values of r down to 0 are determined by means of a curve fit (polynomial of 2nd order). Thus, the value on the y-axis that corresponds to $r = 0$ can be interpreted as λ^2 . This method is shown in fig. 1.3 for some turbulence data measured with the 2d-LCA. In this example the smallest value of r is smaller than the sensor dimension (length of the cantilever $l = 160 \mu\text{m}$) and therefore has been excluded from the fit.

In the following, this indirect determination of the derivative will be referred to as the Löfdahl-Aronson approach, named after the authors who first made use of it.

For highly resolved data (sampling frequency of few tens of kHz) both methods

deliver comparable Taylor lengths. However, the autocorrelation obtained from data that has been recorded with a low sampling frequency provides less points in the region of positive curvature. This immediately leads to a larger error when estimating Taylor's lengths from the parabola fit. On the contrary, the Löfdahl-Aronson approach is not affected by the sampling frequency.

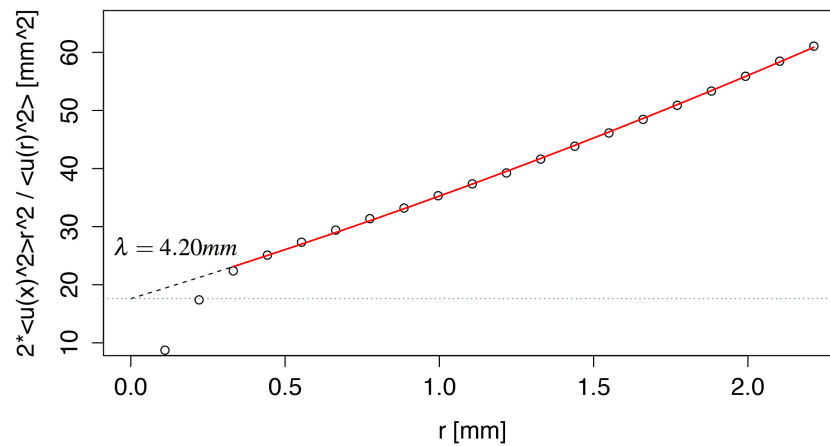


Figure 1.3: Development of eqn. (1.26). Small values of r are approximated using a 2nd order polynomial fit.

1.2.7 Kolmogorov length

The Kolmogorov length scale η is given by:

$$\eta = \left(\frac{v^3}{\varepsilon} \right)^{\frac{1}{4}} \quad (1.27)$$

with the energy dissipation rate ε defined in [11] as:

$$\varepsilon = 15\nu \left\langle \left(\frac{\partial u}{\partial x} \right)^2 \right\rangle. \quad (1.28)$$

The derivation of η is based on considerations derived from K41 and dimension analysis. For a discrete time series $u(x)$, the calculation of the derivative $\frac{\partial u}{\partial x}$ requires a high resolution. This however is often associated with noise. In order to account for this, the derivative is calculated using the same procedure as explained for eqn. (1.26) (Löfdahl-Aronson method). Ignoring the effect of spatial filtering due to the probe size ^a, would underestimate the value of ε .

^aIn that case $\frac{\partial u}{\partial x}$ is calculated as the product of the velocity increment between two adjacent points and the mean velocity.

Chapter 2

Sensor and system design

The objective of this chapter is to explain the working principle of the 2d-LCA and its mechanical and electrical design (except for the cantilever). During the work of this thesis many changes to various components of the anemometer have been undertaken with the goal to improve the signal quality and optimize handling and stability. In particular, the robustness of the 2d-LCA concerning mechanical impacts was insufficient prior to this work.

Following the nomenclature as introduced in [37], the latest version of the 2d-LCA with all improvements will be referred to as the 2d-LCA of third kind. Hence, the previous version (before modifications) is the 2d-LCA of second kind.

2.1 Working principle

The underlying principle utilized in the 2d-LCA is the detection of the deformation of an one-sidedly fixed microstructured cantilever that is exposed to a fluid flow [37, 34]. For a straight inflow, i.e. a flow direction perpendicular to the cantilever surface, the deformation is a response to the drag force \hat{F}_{drag} , that is given by

$$\hat{F}_{drag} = \frac{1}{2}c_d(u)\rho Au^2. \quad (2.1)$$

Here, $c_d(u)$ is the drag coefficient, ρ is the density of the fluid and A is the area of the cantilever that is facing the flow. \hat{F}_{drag} is a uniformly distributed pressure load and causes a simple bending of the cantilever. The largest deflection s

occurs at the tip of the cantilever and is calculated by:

$$s = \frac{l^4 \hat{F}_{drag} w}{8EI_A} \propto \hat{F}_{drag}, \quad (2.2)$$

where l and w are the length and width of the cantilever, E is the Young modulus and $I_A = wd^3/12$ denotes the inertial momentum using the thickness d .

For an oblique flow, i.e. flow at an angle of attack $\alpha \neq 0$, the total deformation of the cantilever is observed to be a superposition of bending and twisting. In that case the quantities A and $c_d(u)$ become functions of α and eqn. (2.1) is complemented by

$$F_{drag} = \frac{1}{2} c_d(u, \alpha) \rho A(\alpha) u^2. \quad (2.3)$$

The detection of the deformation is accomplished by means of the laser pointer principle that is also used in atomic force microscopy. For that purpose, a laser provided by a laser diode ($\lambda_{laser} = 660\text{nm}$, Power = 5mW) is focused onto the tip of the cantilever. The resulting reflection beam is tracked using a 2d-position sensitive detector (2d-PSD) with an active area of $4\text{mm} \times 4\text{mm}$ ^a. This principle is schematically illustrated in fig. 2.1 for both deformation modes. The deflection paths of the reflected spot along the active area due to bending and twisting are decoupled and follow two perpendicular directions. After calibration, each

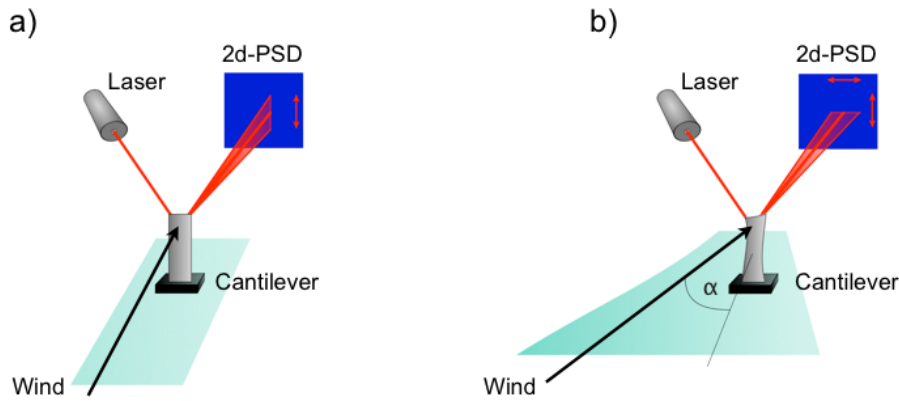


Figure 2.1: Schematic illustration of the deflection of the reflected spot due to bending (a) and twisting (b) of the cantilever.

^aA description of the working principle and further specifications of the 2d-PSD are found in appendix D.

position of the reflected spot along the active area can be unambiguously assigned to a flow velocity and an angle of attack, from which the longitudinal and transverse velocity components can be calculated. That way, simultaneous measurements in 2 dimensions are possible.

2.2 Design of the 2d-LCA of second kind

The design of the 2d-LCA of second kind is shown schematically in fig. 2.2 from two different perspectives. In order to establish a better relationship to the text several building components were numbered. Several parts and complete assemblies have undergone significant modifications, which will be treated separately in 2.3.

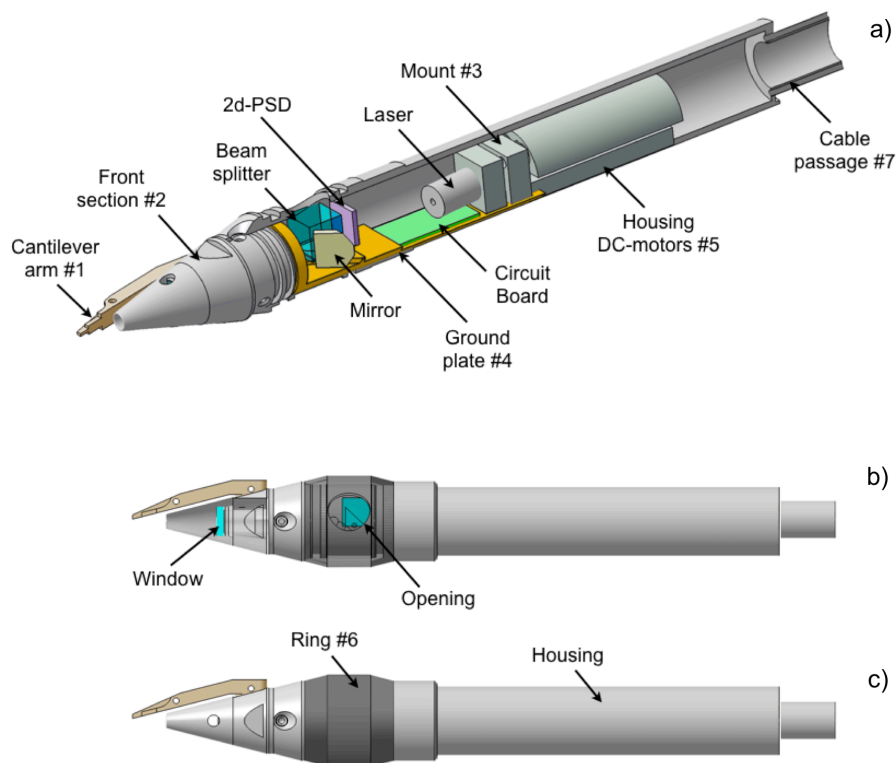


Figure 2.2: Sectional drawing of the 2d-LCA of second kind showing the main components (a,b) and view of the housing (c).

The sensors dimensions are 21.8cm in length and 2.4cm in diameter. All structural building components are self-designed and were made of brass, eloxated aluminum or Teflon. The cantilever arm (part #1) that holds the cantilever is

rigidly fixed to the front section (part #2). The laser is placed on a self-build mirror mount (part #3) that can be remotely adjusted using two DC-motors. That way, the position of the beam can be altered. The laser is redirected by means of a mirror before it passes through a beam splitter cube and finally strikes the cantilever. It exits the inside of the 2d-LCA via a window that is mounted within the passage of the front section. The window is made of KBr and features great transmission properties with almost no losses in the wavelength of the laser. The reflected laser light enters the inside through the same window and strikes the 2d-PSD after passing the beam splitter a second time. All of the inner components are attached to a ground plate (part #4) that can be taken as the foundation of the 2d-LCA. Part #5 is made of Teflon and is used for supporting the DC-motors. The circuit board for processing the signals is in close proximity of the 2d-PSD. That way, losses of signal strength due to long cable and the sensitivity towards noise can be minimized. Furthermore, the 2d-LCA is equipped with various O-rings that provide sealing against fluids from the outside and thus allow for measurements in liquid domains.

The housing of the 2d-LCA is made of aluminum. It provides an opening for access to the 2d-PSD and serves for monitoring of the reflected spot. While operation it is covered using a ring (part #6). The cantilever is located in a distance of 1cm away from the edge of the front section, which is designed with an opening angle of 24.7° . In [37] the influence of the sensor housing and especially of the front section on the flow has been estimated to be negligible. This result has been reviewed by means of a different method that uses a standard x-wire that is built into a 2d-LCA housing (see appendix A).

At the rear end the housing is equipped with a cable passage (part #7) for connection to external units like power supply or A/D-converter. The performance of the 2d-LCA of second kind has been evaluated in [34] and [36] and motivated for further development.

2.3 Design of the 2d-LCA of third kind

Fig. 2.3 shows the setup of the 2d-LCA of third kind. Several modifications have been introduced in order to improve the sensors performance, which will be discussed in the following sections. The technical drawings are found in appendix I.

2.3.1 Modification with regard to stability

The performance of the 2d-LCA of second kind suffered from insufficient stability. It became evident that the alignment of the laser and thus the position

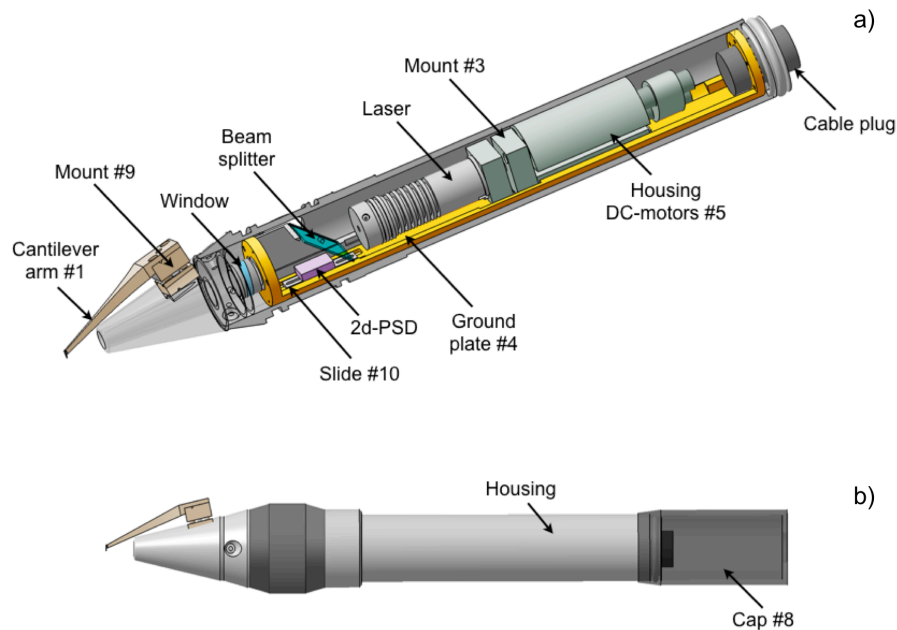


Figure 2.3: Sectional drawing of the 2d-LCA of third kind showing the main components (a) and view of the housing (b).

of the reflected spot changed when the anemometer was shaken, exposed to vibrations or simply pulled by its cable. In order to work against this sensitive behavior, the following parts were redesigned and improved:

Laser mount (part #3): Shocks and knocks against the outer housing led to an displacement of the reflected spot along the 2d-PSD. This shifting can be mainly attributed to a change of the laser alignment. The self-built laser mount turned out to provide an insufficient strength for the weight of the laser module. That is why it was replaced by a high quality and commercially available mirror mount of type Newport MM-050-HEX. This mount features a much stronger restoring force and thus improves the stability.

Ground plate (part #4): The foundation of the 2d-LCA of second kind has been designed very slim and has been fixed to the front section by two screws only. This single-sided fixing together with the very fragile design resulted in unwanted flexibility of the inside of the sensor. Consequently, the alignment of the laser was affected by the deformations of the ground plate, which in turn resulted from shakes or turns of the anemometer. The

stability has been greatly increased by introducing a new ground plate, which is reinforced (thicker and wider) and is also fixed to the rear part of the housing by means of six screws.

Cable passage (part #7): The 2d-LCA of second kind has been equipped with a cable that is directly fed into the inside of the sensor through a cable passage. Pulling the cable raised tensions on the inner components and thus caused a misalignment of the laser. For that reason a plug at the rear of the anemometer has been introduced. It simplifies the handling with the 2d-LCA at the one hand and provides strain relief on the other hand. Additional strain relief is accomplished by a cap (part #8) that also protects the plug.

2.3.2 Modification with regard to handling

Here, the term handling refers to all necessary actions involving arrangements and adjustments of the anemometer that have to be carried out by the user. Improving the handling is an essential part of the development process. In general, good handling properties lead to a wider use of any sensor and decrease the risk of failure. In the following, new features to improve the handling of the 2d-LCA are discussed.

Optical components: A new arrangement of the optical components has been introduced in the 2d-LCA of third kind for several reasons. The laser path as implemented in the older design is shown in fig. 2.4 a). As illustrated the beam splitter cube causes ghost spots, which result from multiple reflections at its edges. Although the edges provide anti-reflection coating, weak reflections are unavoidable. The window (part #6) within the front section generates an additional reflection for the same reason. This reflection causes a spot that strikes the 2d-PSD. Even though it stays in the same location regardless of the cantilever deformation, it still affects the dynamics of the center of gravity of the main reflection spot and thus reduces the resolution power.

The issues listed above led to an improved optical path as shown in fig 2.4 b). The beam splitter cube has been replaced by a thin beam splitter plate that reduces the influence of the ghost spot. The unwanted spot from the reflection caused by the window has been turned away by inclining the window. That way, the reflected spot misses the 2d-PSD. Lastly, the position of the 2d-PSD has been shifted and the mirror has been removed. This arrangement provides more space within the sensor and provides good access to the 2d-PSD from the opening in the housing. This leads to

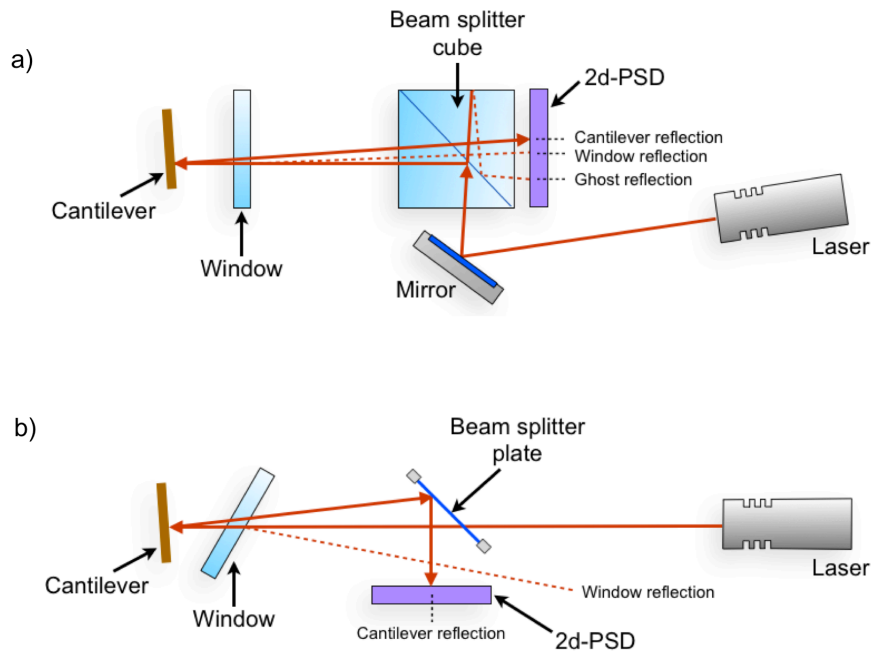


Figure 2.4: Arrangement of the optical components in the 2d-LCA of second kind (a) and in the 2d-LCA of third kind (b).

easier adjustment of the laser spot and thus improves the handling while preparation. The whole preparation process, which needs to be carried out prior to measurements is explained in appendix C.

Cantilever alignment: The previously used cantilever arm is rigidly fixed to the front section of the 2d-LCA. The cantilever chip is handled by means of tweezers and is glued to the cantilever arm with commercially available superglue. However, this procedure does not allow for a precise and reproducible alignment. As a consequence the spot reflecting from the cantilever likely misses the 2d-PSD. A correction of alignment is achieved by means of bending of the cantilever arm with pliers. This method is not user-friendly and requires training. In addition, there is a risk of destroying the cantilever.

In order to achieve a better alignment, an alignment station has been developed (see fig. 2.5). It basically consists of a three-dimensional positioning stage with a mounted cantilever arm and a slot with a spring-loaded face where the cantilever chip is clamped. Once the cantilever is carefully pressed against the back wall of the slot a reproducible align-

ment for each cantilever is guaranteed. Both components are brought together by means of the positioning stage (ideally this is carried out under a microscope). Finally, the arm is glued to the cantilever using a small amount of glue.

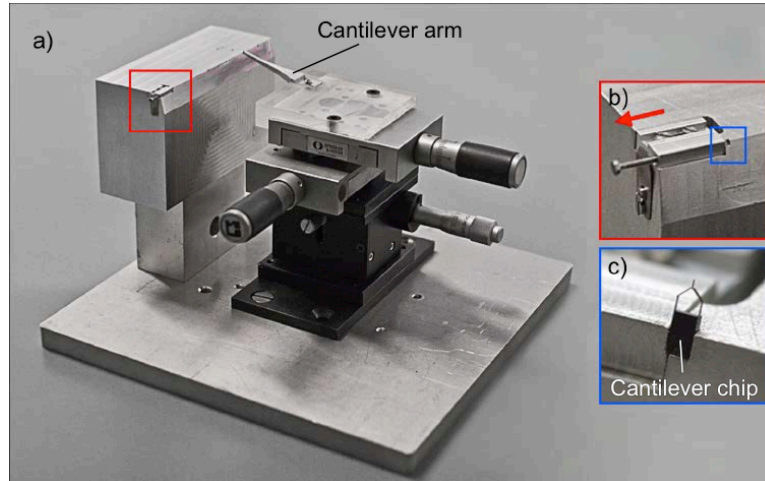


Figure 2.5: Alignment station for attaching the cantilever to the cantilever arm (a). The enlarged sections (b) and (c) show the spring-loaded mechanism that is used to clamp the cantilever chip.

Although the alignment station ensures an overall good alignment of the cantilever, small deviations are still likely to occur mainly due to production tolerances of the cantilever arms. These deviations are compensated by means of part #9 and part #10 (see fig. 2.6). Part #9 is a self-built mirror mount, that allows for precise changes of the spot position along the x-axis of the 2d-PSD, whereas part #10 is a slide to modify the position along the y-axis.

DC-motor mechanism: Due to production tolerances, the DC-motors in the 2d-LCA of second kind tend to tilt within the motor housing (part #5) when using small voltages, i.e. low torque. Larger applied voltages overcome this jamming, but also have an adverse effect on the positioning accuracy due to the faster rotation. In order to achieve a smooth and slow rotational speed, tiny self-built cardan shafts were introduced between the laser mount and the DC-motors (see fig. 2.7). These shafts compensate for tolerances and improve the position accuracy.

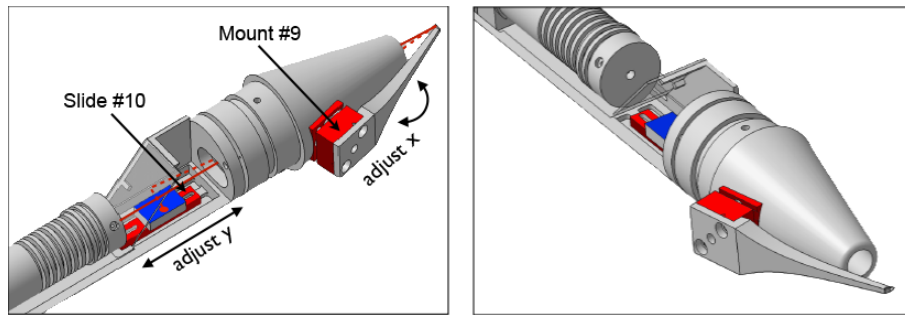


Figure 2.6: Closer view at part #9 and part #10 from two different perspectives.

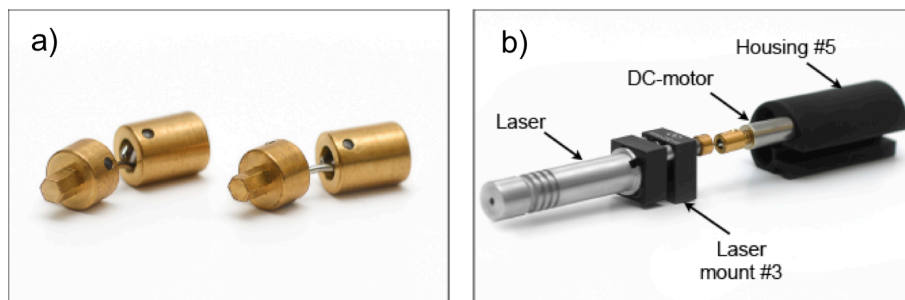


Figure 2.7: Photograph of the cardan shafts alone (a) and in installed state (b).

Central unit: Before this thesis the 2d-LCA has been used in connection with a unit that provides setting possibilities for the DC-motors and the power supply for the electronics. A second power supply for supplying the laser module and an A/D converter has been connected in addition. In [36] an alternative central unit has been introduced that also features some signal conditioning. Still, the overall setup consisted of several separated modules that created potential sources of errors and limited the mobility. For that reason, a new central unit (fig. 2.8) has been developed. The 2d-LCA of third kind comes with one box that includes the power supply for all components of the anemometer, controls of the DC-motors and an A/D-converter. Combining all of these components in one box saves cable length and significantly improves the handling. In addition, the unit contains adjustable low-pass filters and amplifications settings. Thus, the voltage output of the anemometer can be adapted to the input range of the A/D-converter, which minimizes discretization. The backside enables the connection of additional sensors to the built-in A/D-converter with

6 analog input channels. Thus, measurements with several probes can be performed simultaneously. The circuit diagram for the central unit is found in appendix H.

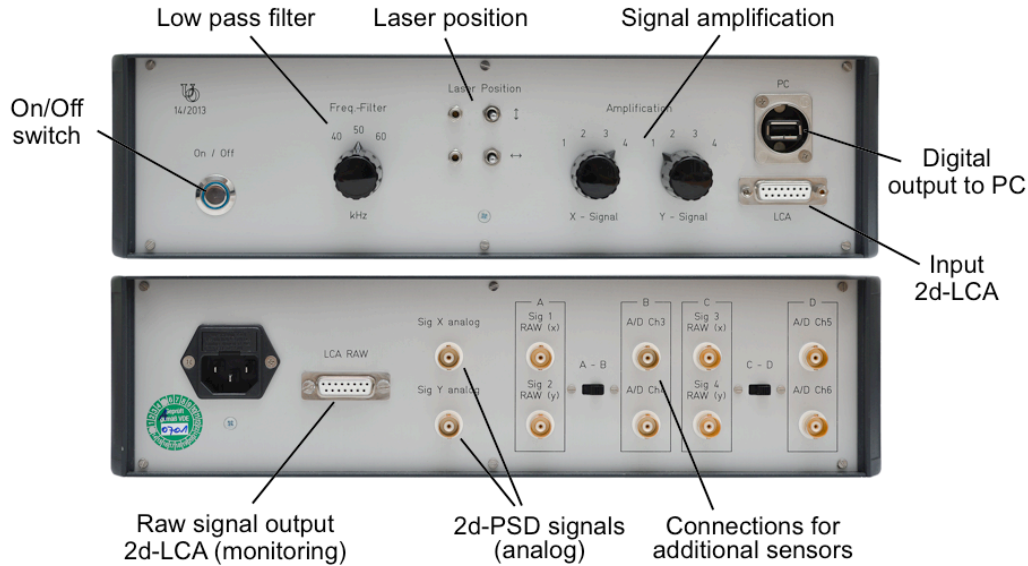


Figure 2.8: Photograph of the front and back of the central unit with descriptions of the main functions.

2.3.3 Modification with regard to signal quality

The output signal of the 2d-LCA is characterized by its dynamical behavior and its noise level. The signal quality is determined by the design of the circuit and its components. A particular focus is on the 2d-PSD (type Hamamatsu S5990-01) that is used in the 2d-LCA of second and third kind. As the performance of this position detector is crucial for the overall performance of the anemometer, it deserves some closer inspection. The explanation of functionality and the discussion of properties of 2d-PSDs is moved to appendix D. In the following, all efforts to improve the signal quality will be presented.

The 2d-LCA of second kind outputs four voltage signals that are obtained from four current signals provided by a 2d-PSD by means of transimpedance connections. These signals are computed to output the position of the reflected spot (given by two voltage signals that correspond to the x- and y-coordinates) by an external unit that is discussed in [36]. The four voltage signals provided by the internal electronics are very weak ($\sim 100\text{mV}$). This is because of the low photo

currents provided by the 2d-PSD. The amplification is done by the external unit before computation. However, this procedure causes some noise in the final signals.

That is why the electronics of the 2d-LCA of third kind were completely revised. A new designed internal circuit (see appendix H for circuit diagram) does not only process the current signals provided by the 2d-PSD, but also computes the x- and y-component of the reflected spot along the 2d-PSD. This circuit board (see fig. 2.9) is small enough to fit within the anemometer housing. Thus, the 2d-LCA of third kind outputs only two signals that already give the position of the reflected spot. The steps necessary to accomplish this are summarized in the following:

1. Transformation of the current signals ($I_1 - I_4$) provided by the 2d-PSD into voltage signals ($V_1 - V_4$).
2. Amplification of voltage signals ($V_1 - V_4$) to the order of 1V.
3. Summing the voltage signals ($V_1 - V_4$) according to:

$$\hat{V}_x = (V_1 + V_3) - (V_2 + V_4)$$

$$\hat{V}_y = (V_1 + V_3) - (V_2 + V_4)$$

$$V_{sum} = V_1 + V_2 + V_3 + V_4$$

4. Performing division according to:

$$V_x = \frac{\hat{V}_x}{V_1 + V_2 + V_3 + V_4}$$

$$V_y = \frac{\hat{V}_y}{V_1 + V_2 + V_3 + V_4}$$

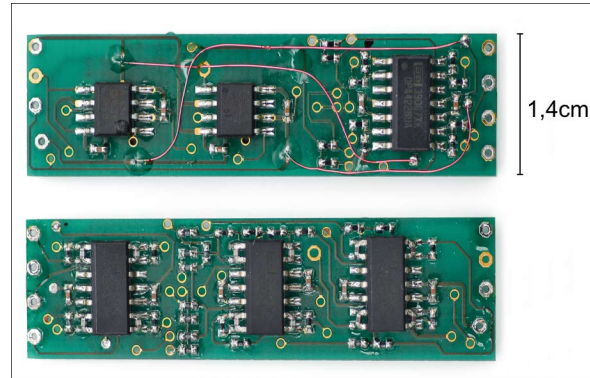


Figure 2.9: Photograph of the circuit board (front and back side) used for the 2d-LCA of third kind.

The transimpedance connection used for the first step corresponds to the circuit shown in fig. 2.10. It consists of a low-noise voltage-based op-amp of type OPA-4277U, a capacitor that eliminates oscillations due to the input capacitance of the 2d-PSD and a feedback resistor R_f . For the subsequent summing (step 2) it is beneficial to have larger signals in the order of 1V as the op-amps used here perform better in this region. In order to achieve that, R_f is adjusted

accordingly. In step 3 the output signals of the transimpedance preamplifier are

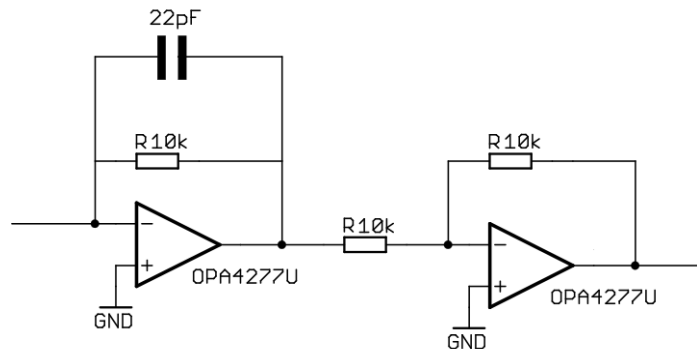


Figure 2.10: Circuit for transformation of the current signals provided by the 2d-PSD into amplified voltage signals.

passed on to summing and inverting amplifiers in order to calculate \hat{V}_x , \hat{V}_y and V_{sum} . For these analog operations the same type of op-amps, which feature a very high slew rate ^a of $8V/\mu s$ are used. The slew rate can be taken as a measure for the speed of an op-amp and thus plays a key role in the design of the electronics.

Lastly, in step 4 the divisions are carried out using an analog multiplier of type AD633JR, which has been integrated in the feedback loop of another op-amp of type OPA-4277U.

In order to demonstrate the performance of the revised electronics some tests were carried out that are presented in figure 2.11. Blue graphs correspond to the 2d-LCA of second kind and black graphs to the 2d-LCA of third kind. Here, only the raw voltage signals of the x-component are considered. The graphs in fig. 2.11 (a) and (d) show power spectra without a reflected spot, thus only the noise due to the electrical components is visible. Figure 2.11 (b) and (e) show power spectra as obtained from measurements in a turbulent flow and (c) and (f) refer to the corresponding time series. The plots were generated using the same test conditions for both types of 2d-LCA.

As can be seen from the plot in (a), the noise due to the electronics is at a constant high level with the exception of some sharp peaks around 25kHz, whereas the noise level of the new electronics improved a lot (d). The spectrum in (b) reaches a dynamic range of about 6 orders of magnitude until it merges into noise, which is one order less when compared to the newer design. Lastly, the time series shown in (c) is superimposed with noise and shows amplitudes in

^aThe slew rate for a sinusoidal signal is given by: $sl = 2\pi \cdot f \cdot V$

the range of 50mV only. The signal can be further amplified by means of an external amplifier, thus making better exploitation of the acceptance range of the A/D-converter. However, in that case the noise is amplified as well. In contrast, the revised electronics provide a much stronger (few V) and smoother signal as can be seen from the plot in (e).

Although, all components of the circuit were chosen to operate fast enough in order to resolve the first resonance frequency of the cantilever ($\approx 100\text{kHz}$), the temporal resolution of the circuit has been tested under laboratory conditions. For this purpose, the circuit has been fed with three constant DC-signals and one alternating signal in the range of 500Hz-250kHz. Fig. 2.12 exemplarily shows the drop in gain of the output signal for the x-component with regard to the gain at 100Hz for increasing excitation frequency. A drop of -3dB occurs at about 146kHz. This cut-off frequency fits well to the design.

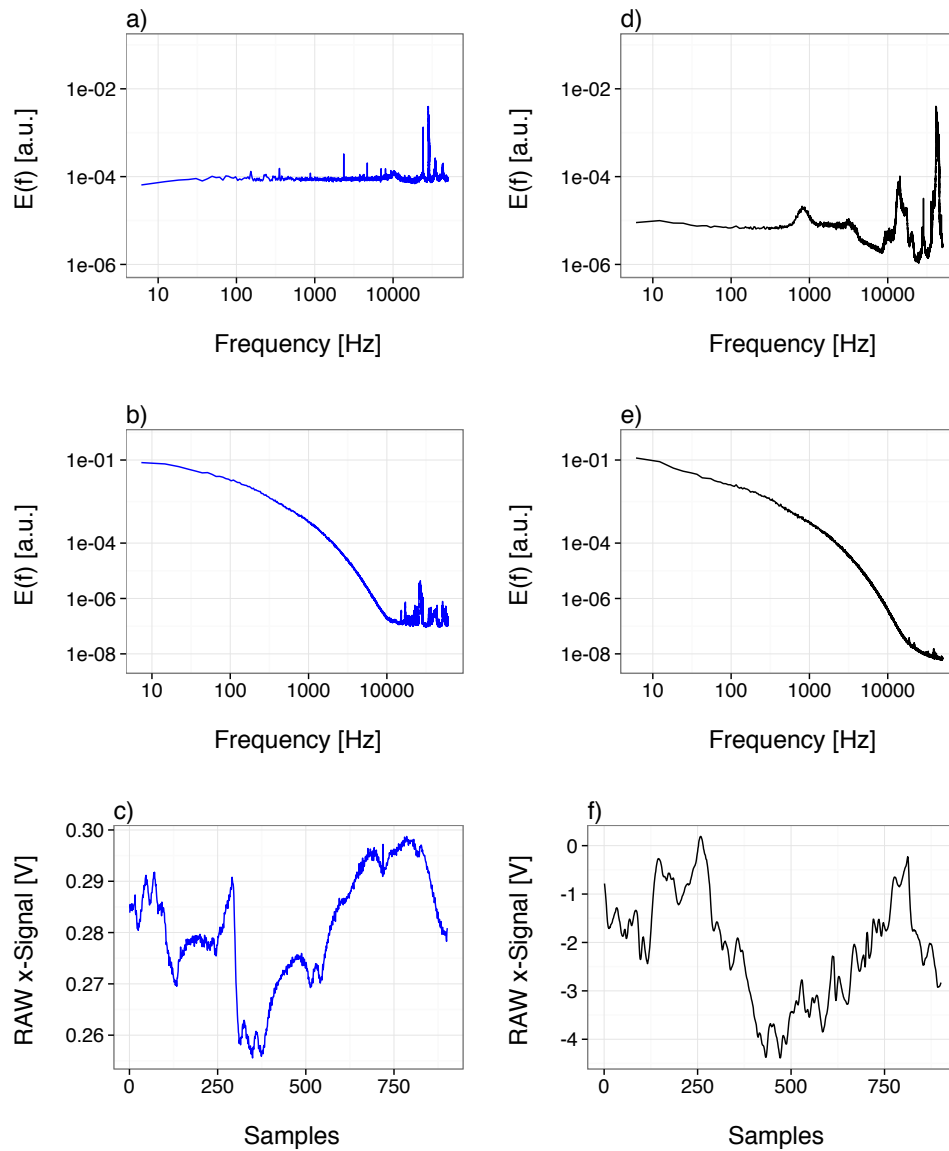


Figure 2.11: Comparison between the 2d-LCA of second kind (blue) and the 2d-LCA of third kind (black) in terms of spectra without light on the 2d-PSD (a, d), spectra of a turbulent signal (b, e) and a section of the corresponding time series (c, f). The plots were produced using the respective voltage signals of the x-component of each 2d-LCA. The measurements for the plots in (b, c, e, f) were conducted under same conditions and with same cantilever.

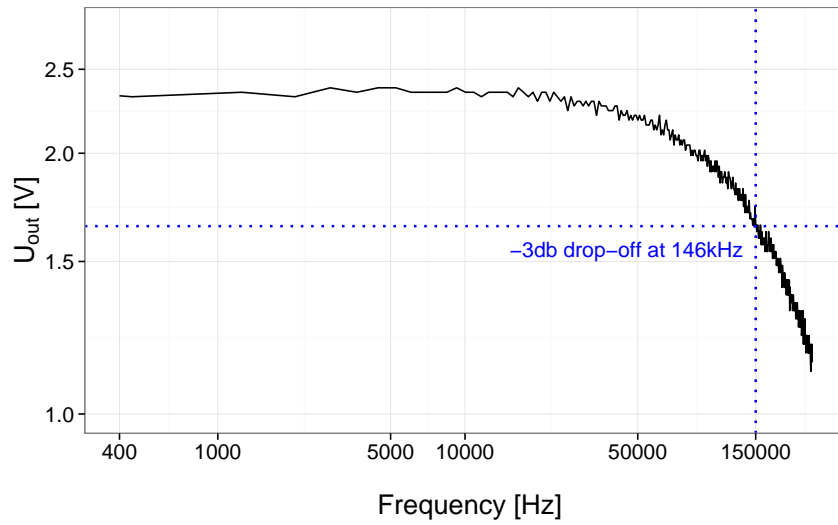


Figure 2.12: The graph represents the x-signal of the electronics for a sinusoidal excitation at I_1 in the range of 400Hz-250kHz. The other three inputs of the electronics (I_2, I_3, I_4) are fed with constant DC-signals. The dashed lines correspond to a -3db decay in gain with regard to the voltage output at 100Hz. Therefore, the cut-off frequency is about 146kHz.

Chapter 3

Cantilever

The properties of the sensing element of the 2d-LCA, i.e. the cantilever, are primarily decisive for the overall performance of the anemometer. The work done in recent years [36, 32] shows that the optimization of the cantilever design is essential for the ongoing development of the 2d-LCA. This chapter takes a close look at the manufacturing process of the cantilevers used for this thesis and gives an introduction to the analytic and experimental investigation of its characteristic properties.

3.1 Cantilever designs and manufacturing process

The cantilevers used in [36, 34, 32, 37] have simple rectangular designs and are made of silicon oxide (SiO_2). These cantilevers have equal thicknesses of 2μ and different widths of $35\mu\text{m}$ or $40\mu\text{m}$ and lengths of $140\mu\text{m}$, $160\mu\text{m}$, $180\mu\text{m}$, $200\mu\text{m}$ or $220\mu\text{m}$. The cantilevers are attached to a framework structure through the front face, i.e. an area of size width \times thickness.

In [34] it has been found that the rectangular cantilevers are sensitive towards inflow directions and that calibrations in two-dimensional flows up to angle of attack of $\pm 40^\circ$ are possible. However, the dynamics of the signal corresponding to the transverse velocity component was reported to be very weak in comparison to the longitudinal component. On these grounds, in [36] FEM-simulations of redesigned cantilevers were presented that gave reason to believe that a small vane at the tip of the cantilever could significantly increase the sensitivity towards cross-winds. Motivated by these results, cantilevers with new designs were manufactured.

A cantilever chip of the newest generation is shown in fig. 3.1 together with an magnification of the vane-equipped cantilever (highlighted in yellow) and the root region (highlighted in red). The illustrated cantilever is $180\mu\text{m}$ in length,

$40\mu\text{m}$ in width and $1.65\mu\text{m}$ in thickness. The size of the vane is $50\mu\text{m} \times 35\mu\text{m} \times 9\mu\text{m}$ (height \times length \times width). Other designs with shorter lengths of $140\mu\text{m}$ and $160\mu\text{m}$ and smaller vane heights of $30\mu\text{m}$ have been realized as well.

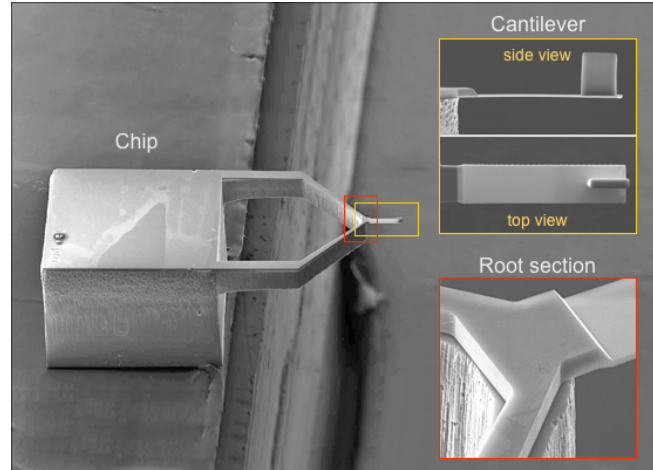


Figure 3.1: Redesigned cantilever chip with magnification of the cantilever with vane (highlighted in yellow) and the root section (highlighted in red).

The main feature of the new cantilever design is the vane. First prototypes of vane-equipped cantilevers used vanes made of nickel (Ni). These were attached to the cantilevers using galvanic processes. However, this approach has not yielded satisfactory results. Tests in the wind tunnel have shown that the Ni-vanes fall off the cantilever surface at velocities of about 10-15m/s. Better results have been achieved with vanes made of SU-8, a polymer that can be shaped using photo-patterning techniques. The material is applied onto the wafer using spin coating. After that it is thermally dried and cross-linked by means of UV exposure and tempering. In the final stage, the unexposed areas are removed using a solvent. The vanes most likely stick to the cantilever surface due to electrostatic forces, but sustain wind speeds of up to at least 50m/s. Figure 3.2 shows a comparison between a Ni-vane (left) and the first attempt of a vane made of SU-8 (right). As can be seen, the SU-8 vane has much smoother surfaces than the Ni-vane.

The architecture of the new cantilever design is shown schematically in fig. 3.3. The cantilever chip consists of a device layer and a handle layer. Both layers are made of Si and are separated by a thin layer of SiO₂ (thickness of $1\mu\text{m}$). The cantilever is part of the device layer, whereas the device layer is basically a

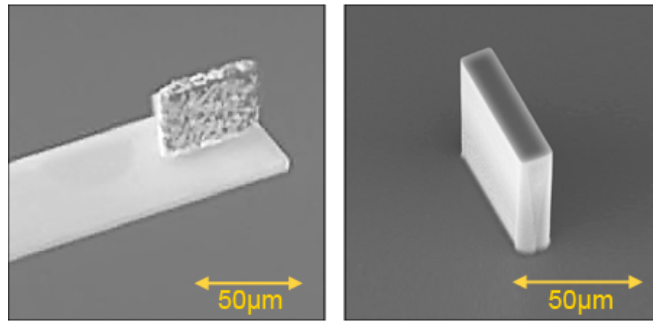


Figure 3.2: Cantilever with a Ni-vane (left) and first prototype of a SU-8 vane built on a substrate (right).

silicon block ($575\mu\text{m}$ in height) that is used as support and for attaching to the cantilever holder of the 2d-LCA (see fig. 2.2 part #1).

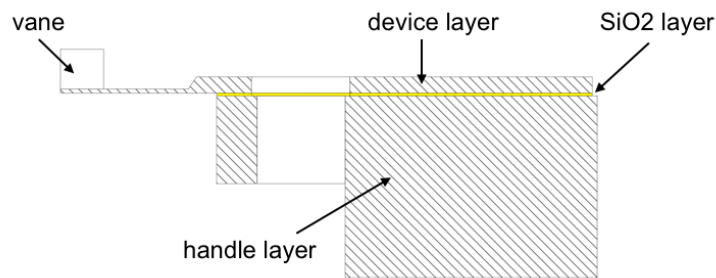


Figure 3.3: Architecture of the cantilever chip (side view).

The older cantilever designs suffered from a very high fragility. In fact, many broke already due to shakes of the wafer while being still attached to it or in the process of breaking the bridge between the chip and the wafer. In order to decrease these risks for the new cantilevers the stability of the junction has been strengthened by thickening the cantilever at its root (see the section marked in red in fig. 3.1). That way, considerably more robustness against breakage has been achieved.

Lastly, the side of the cantilever that is facing the laser beam is equipped with a reflection pad of $40\mu\text{m} \times 40\mu\text{m}$ ($+10\mu\text{m}$ shadow area) in size. The reflection pad consists of a 50nm-gold layer and a 5nm-titanium layer (bonding agent). The pad ensures good reflectivity of the incoming laser beam as light at a wavelength of 630nm would simply pass through the silicon. The impact on the size of the reflection pad has been studied in [32]. It has been found that smaller

reflection pads produce more uniform spots, which in general have a positive impact on the signal quality. On the contrary, the older designs were completely coated with aluminum. However, some (about 10%) of the available cantilevers were contaminated with solvent during the manufacturing process resulting in a non-uniform reflection surface. One of the most affected cantilevers is shown in figure 3.4 (a) together with a clean one (b).

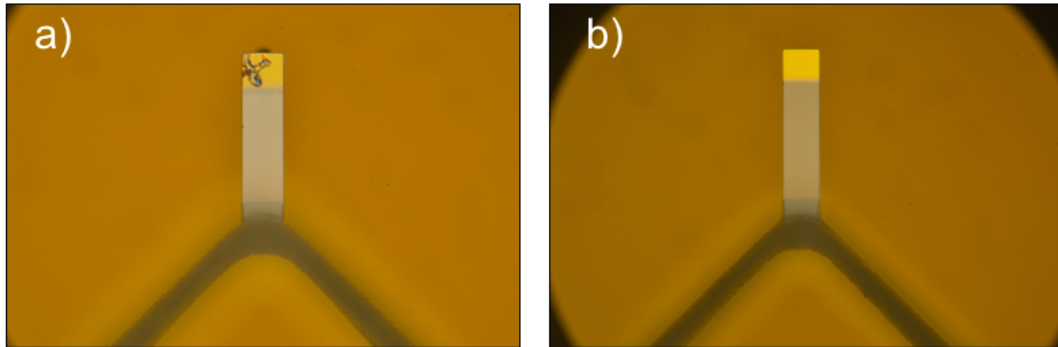


Figure 3.4: Contaminated reflection pad (a) and a clean reflection pad (b).

3.2 Mechanical and fluidic properties of cantilevers

The dimensions of the cantilever implicate small local Re ^a in the range of $\approx 2-50$ for typical laboratory flow velocities of 1-20m/s (in air). For lower velocities inertial forces become prominent and the state merges into the Stoke's regime where $F_{drag} \propto v$.

The c_d -curve for Re up to 130 has been studied by means of steady-state CFD-simulations using OpenFOAM. In the course of this, the flow situation around the cantilever geometry has been reproduced, i.e. the one-sided mounting has been considered. The resulting c_d -curve is shown in figure 3.5 in dependence of Re and v . The obtained values are fitted using $c_d \approx 5.73/u + 1.3$ (red curve). It has been found that c_d undergoes large variations for Re up to about 40 and converges to a constant value of 1.52 for higher Re . The divergence from literature values of $c_d = 1.19$ (rectangular plate of length / width ratio 4:1 for Re of 100-100.000 [3, 4]) is caused by different boundary conditions that apply to free hanging structures. For lower Re not much consistent data exists for rectangular structures.

^aThe width of the cantilever is taken as the characteristic length for the calculation of Re .

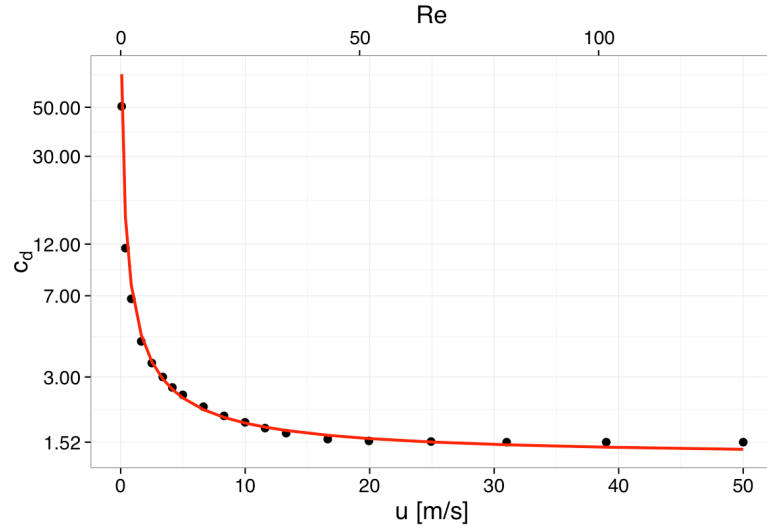


Figure 3.5: c_d -values for a one-sidedly fixed rectangular plate with length / width-ratio of 4:1 obtained from CFD-simulations (black dots) and curve fit according to $c_d \approx 5.73/u + 1.3$ (red line).

For constant ρ and $u \gtrsim 1$ m/s the variation of c_d/u is small compared to u^2 and therefore one can assume $\hat{F}_{drag} \propto u^2$. As a consequence the deflection of the cantilever and hence the resolution power of the sensor increase with increasing u ^b. This is demonstrated in fig. 3.6 where $\hat{F}_{drag}(c_d(u), u)$ is compared with $\hat{F}_{drag}(c_d = 1.52, u)$. The length and thickness of the cantilever are the crucial parameters to set its sensitivity towards the drag force. At least for a straight inflow the width w does not affect the deflection distance s , as can be seen from eqn. (2.2). The deflection distance Δd of the laser spot along the active area of the 2d-PSD can be estimated using:

$$\Delta d \approx D \cdot \tan(2\gamma), \quad (3.1)$$

with

$$\gamma = \arctan \left[\hat{F}_{drag} \cdot \frac{l^3}{2E \cdot I_A} \left(\frac{l_{pad}^4}{12l^4} - \frac{l_{pad}^3}{3l^3} + \frac{l_{pad}^2}{2l^2} \right) \right]. \quad (3.2)$$

Here, D is the distance between the cantilever and the 2d-PSD and l_{pad} (\approx

^bThis is true for deflections within the elastic range only, i.e. the amount of deflection where the stiffness remains constant.

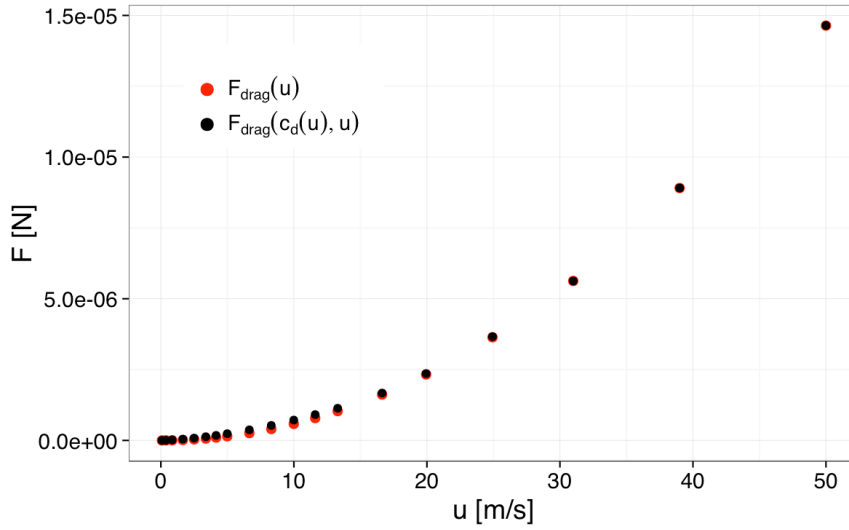


Figure 3.6: Drag force upon the cantilever considering $c_d(u)$ as obtained from fig. 3.5 (black) and a constant $c_d = 1.52$ (red).

$l - 20\mu\text{m}$) corresponds to the position of the center of the reflecting pad. In fig. 3.7 eqn. (3.1) is plotted for three different cantilever lengths of $140\mu\text{m}$, $160\mu\text{m}$ and $180\mu\text{m}$ with the properties listed in table 3.1 and $c_d(u)$ as shown in fig. 3.5. Since the sensor area of the 2d-PSD is $4\text{mm} \times 4\text{mm}$ and the size of the spot is approximately 2mm (size of the 0th-order intensity maxima [32]), an effective maximum deflection distance that can be processed by the 2d-PSD reduces to 2mm (highlighted in grey). The plot in fig. 3.7 can be used to

| | |
|----------------------------|-----------------------------|
| Density Si | 2336 kg/m^3 |
| Density air | 1.204 kg/m^3 |
| Young's modulus E for Si | 130GPa (100-layer) |
| Cantilever width w | $40\mu\text{m}$ |
| Cantilever thickness t | $1.65\mu\text{m}$ |
| Distance D | 10 cm |

Table 3.1: Overview of the parameters used for the simulation in fig. 3.7.

choose the right cantilever if the flow velocity can be estimated. Moreover, it shows that an increase of the measurement range due to a longer cantilever is

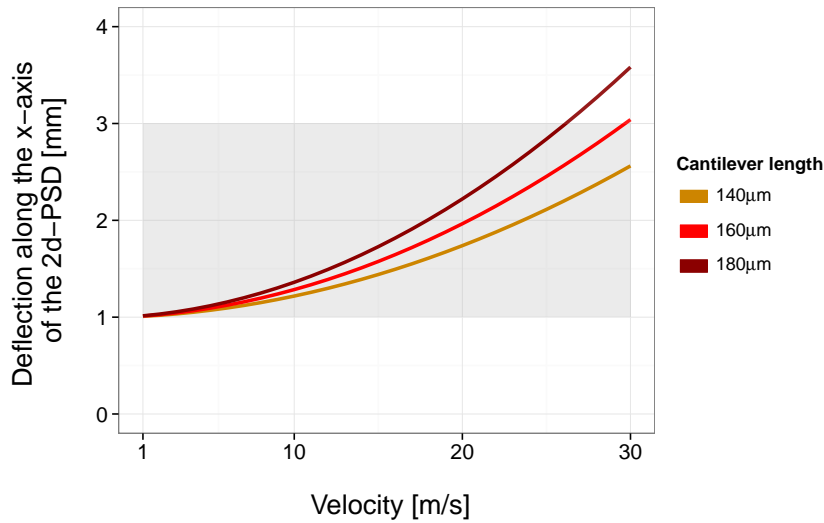


Figure 3.7: Simulated deflection distances along the x-direction of a 2d-PSD with side length of 4mm for velocities of 1-30m/s for cantilevers of 140µm, 160µm and 180µm in length. The total light intensity must remain within the grey area in order to be detected by the 2d-PSD entirely.

only achieved at the expense of resolution power.

The temporal resolution of the 2d-LCA is limited by the frequency of the first resonant mode of the cantilever. In this context, two main questions arise: 1. What are the resonant modes for the individual cantilever designs? 2. Do these modes correspond to frequencies high enough in order not to be excited while performing measurements in turbulent flows?

For a one-sidedly clamped cantilever, the excitation frequency for the first mode is calculated according to

$$\omega_{vac} = \xi^2 \sqrt{\frac{EI_A}{m_s l^3}} = \sqrt{\frac{k}{m_s}}. \quad (3.3)$$

Here, $\xi=1.875$ is the first damping coefficient for a clamped cantilever with one free hanging end, E is the Young's modulus, I_A is the moment of inertia and $k = \xi^4 EI_A / l^3$ is the spring constant. The quantity m_s denotes the structural mass of the cantilever. Eqn. (3.3) does not consider damping and thus is only valid in vacuum. For a cantilever with specifications as listed in table 3.1, $\omega_{vac} = 102.5\text{kHz}$. The coating for the reflections pad has been considered as a uniformly distributed mass.

This result has been verified experimentally by using a setup originally designed for investigations of natural modes of nanowires, which are used as mass and force measurement devices [40]. The measurements were done at the University of Vicortia, BC, Canada. The setup consists of a vacuum chamber, which is evacuated to 10^{-7} mbar. Within this vacuum chamber up to three chips with cantilevers were placed and excited electrostatically. The excitation was done by a spectrum analyzer of type Agilent E4402B that provided a sweep signal of 35kHz-145kHz at constant amplitude of 2mV. While doing so, the oscillation of one cantilever at each time has been monitored using laser interferometry. A detailed discription of the experimental setup is given in appendix E.

The response of the cantilever in terms of amplitude is shown in fig. 3.8 in the orange line graph. As can be seen, a large peak exists at a frequency of 99.8kHz that corresponds to the first natural frequency. This is very close to the previously found value of 102.5kHz using eqn. (3.3). From the peak in the graph the Q-factor can be determined using $Q = f_{peak} / \Delta f$, where f_{peak} is the peak frequency and Δf is the half-power bandwidth. For the cantilever considered here a Q-factor of $Q_s = 199.8$ has been found. The subscript 's' indicates that the Q-factor depends on structural quantities only as all viscous effects were eliminated.

The influence of fluid damping can be estimated analytically. However, before beginning this analysis it must be clarified wheather continuum or statistical mechnics should be applied. This is done by using the Knudsen number given by $Kn = l_p / w$ with l_p being the mean free path between air molecules at a pressure of 1atm. For a cantilever width of $w = 40\mu\text{m}$ and $l_p = 65\text{nm}$, Kn is in the order of $1 \cdot 10^{-3}$, which means that the problem can be described using continuum mechanics.

The eqn. (3.4) shows the relation between the frequencies of the resonant modes

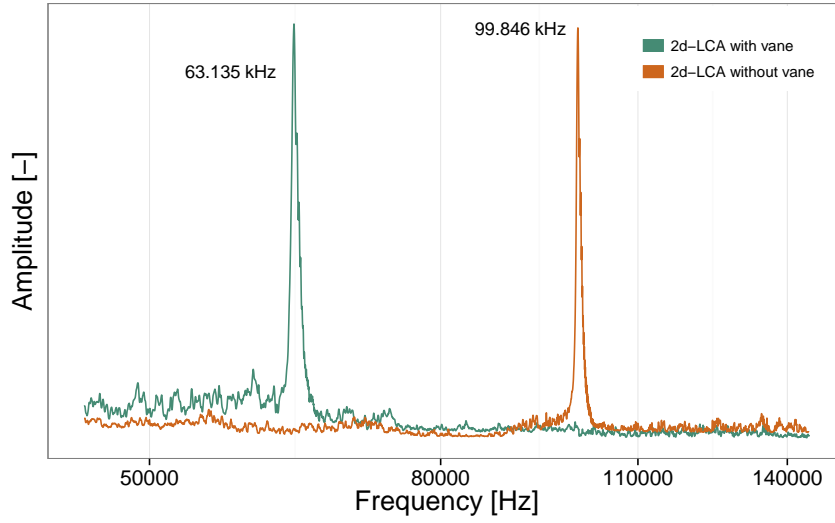


Figure 3.8: Sweep frequency against excitation amplitude for a cantilever of $140\mu\text{m}$ in length with vane (green) and a cantilever of same length but without vane (orange).

for the undamped and damped case. A noticeable departure from the measured frequency in vacuum due to fluid damping is only expected for Q -factors of $Q \sim 1$.

$$\omega_{fluid} = \omega_{vac} \left[1 - \frac{1}{2Q^2} \right]^{\frac{1}{2}} = \omega_{vac} \left[1 - \frac{C^2}{2mk} \right]^{\frac{1}{2}} \quad (3.4)$$

Here $m = m_s + m_f$ is the effective mass, with m_f being the fluid added mass seen by the oscillating cantilever when opposing the flow. Similarly, the total damping $C = C_s + C_f$ is the sum of damping due to the structural composition C_s and fluid damping C_f . C_f and m_f for a beam with rectangular cross-section can be calculated according to [41] by:

$$m_f = \frac{\rho_f}{\rho_s} \kappa_m m_s \quad (3.5)$$

$$C_f = \pi \nu \rho_f l \beta \kappa_c, \quad (3.6)$$

with the dimensionless parameter $\beta = \omega_{vac} w^2 / 4\nu$, that depends on the kine-

matic viscosity ν , the width of the cantilever w and the undamped frequency ω_{vac} and

$$\kappa_m = RE \left(1 + \frac{4iK_1(-i\sqrt{i\beta})}{\sqrt{i\beta}K_0(-i\sqrt{i\beta})} \cdot \Omega(\omega) \right) \quad (3.7)$$

$$\kappa_c = IM \left(1 + \frac{4iK_1(-i\sqrt{i\beta})}{\sqrt{i\beta}K_0(-i\sqrt{i\beta})} \cdot \Omega(\omega) \right). \quad (3.8)$$

K_0 and K_1 denote modified Bessel functions of third kind. $\Omega(\omega)$ is a correction term that applies for beams with rectangular cross-sections and is given by:

$$\begin{aligned} RE(\Omega(\omega)) = & (0.91324 - 0.48274 \cdot \log(\beta) + 0.46842 \cdot \log(\beta)^2 \\ & - 0.12886 \cdot \log(\beta)^3 + 0.044055 \cdot \log(\beta)^4 - 0.0035117 \cdot \log(\beta)^5 \\ & + 0.00069085 \cdot \log(\beta)^6) \cdot (1 - 0.56964 \cdot \log(\beta) + 0.48690 \cdot \log(\beta)^2 \\ & - 0.13444 \cdot \log(\beta)^3 + 0.045155 \cdot \log(\beta)^4 - 0.0035862 \cdot \log(\beta)^5 \\ & + 0.00069085 \cdot \log(\beta)^6)^{-1} \end{aligned}$$

$$\begin{aligned} IM(\Omega(\omega)) = & (-0.024134 - 0.029256 \cdot \log(\beta) + 0.016294 \cdot \log(\beta)^2 \\ & - 0.00010961 \cdot \log(\beta)^3 + 0.000064577 \cdot \log(\beta)^4 \\ & - 0.000044510 \cdot \log(\beta)^5) \cdot (1 - 0.59702 \cdot \log(\beta) + 0.55182 \cdot \log(\beta)^2 \\ & - 0.18357 \cdot \log(\beta)^3 + 0.079156 \cdot \log(\beta)^4 - 0.014369 \cdot \log(\beta)^5 \\ & + 0.0028361 \cdot \log(\beta)^6)^{-1}. \end{aligned}$$

The value of C_s is obtained from:

$$C_s = m_s \omega_{vac} / Q_s. \quad (3.9)$$

With the equations 3.9, 3.6, 3.5 and the relation

$$Q = Q_s \frac{\sqrt{1 + (m_f/m_s)}}{1 + (C_f/C_s)} \quad (3.10)$$

the Q-factor for the damped case can be calculated. This calculation yields $Q =$

6.1, which is significantly smaller than Q_s . Consequently, even in the unlikely case of excitations due to the turbulent flow the oscillation of the cantilever would be massively damped.

Fig. 3.9 demonstrates the evolution of the amplitude peak for small variations of the pressure. The plot was created using the same experimental setup as described above. This time, however, a longer cantilever of $l = 160\mu\text{m}$ without a vane has been used and the pressure in the chamber has been altered.

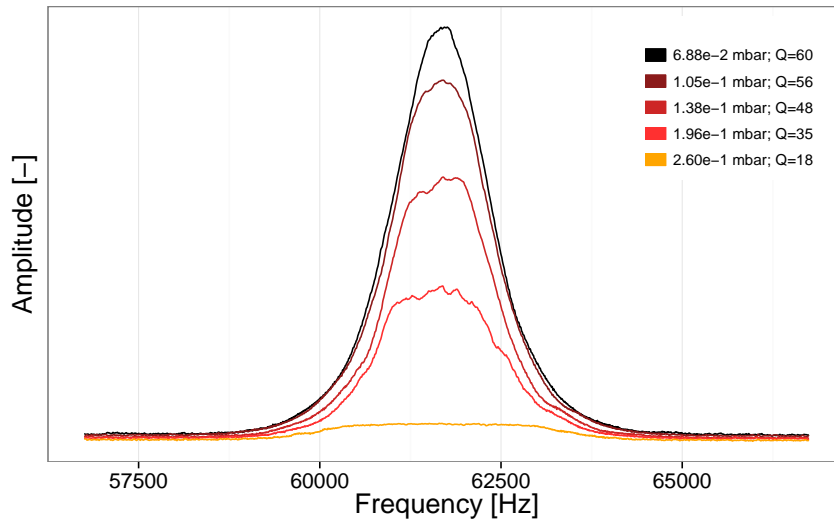


Figure 3.9: Evolution of the amplitude for a cantilever of $160\mu\text{m}$ in length without vane at different pressures. The corresponding Q-factors are found in the legend.

The green spectrum in fig. 3.8 corresponds to a cantilever of $140\mu\text{m}$ in length and a vane of $30\mu\text{m}$ in height. Due to the additional mass, which is comparable to the mass of the cantilever, the resonance peak shifts by more than 30% to a peak frequency of 63.1kHz . From eqn. (3.3) one can see that doubling the mass leads to a decrease of ω_{vac} by the factor of $1/\sqrt{2}$, which corresponds to $\approx 70\text{kHz}$.

The investigation of resonant frequencies of higher modes was done using computational simulations with COMSOL. Exemplarily, the shapes of the first three modes for a cantilever of $160\mu\text{m}$ in length and with a vane of $50\mu\text{m}$ in height are shown in fig. 3.10. As expected, the first mode is a simple bending mode. The second mode is torsional and the third mode is again a bending mode with two nodes.

COMSOL has been also used to estimate the resonant frequencies of the first three modes for the types of cantilevers listed in table 3.2.

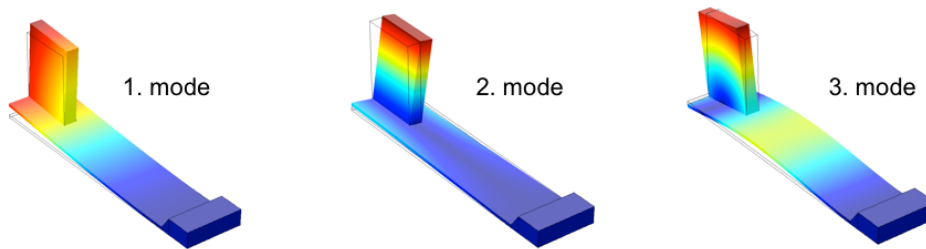


Figure 3.10: Simulation of the first three resonant modes for a cantilever of $160\mu\text{m}$ in length and with a vane of $50\mu\text{m}$ in height.

| Type of cantilever | 1. mode | 2. mode | 3. mode |
|--|------------|-----------|-----------|
| length = $140\mu\text{m}$ vane height = $0\mu\text{m}$ | 101.6 kHz | 635.1 kHz | 732.1 kHz |
| length = $140\mu\text{m}$ vane height = $30\mu\text{m}$ | 62.2 kHz | 356.6 kHz | 485.5 kHz |
| length = $160\mu\text{m}$ vane height = $0\mu\text{m}$ | 59.4 kHz | 371.3 kHz | 484.3 kHz |
| length = $160\mu\text{m}$ vane height = $50\mu\text{m}$ | 50.5 kHz | 196.3 kHz | 311.0 kHz |
| length = $180\mu\text{m}$ vane height = $0\mu\text{m}$ | 46.9.5 kHz | 293.4 kHz | 427.4 kHz |

Table 3.2: Overview of the first three resonant frequencies for different types of cantilevers.

Chapter 4

Calibration

The calibration of the 2d-LCA is carried out in a laminar flow wind tunnel, although later measurements are taking place in a turbulent domain. This can be done for typical laboratory flows at velocities around 20m/s and Kolmogorov lengths η in the order of millimeters. In that case the flow around a cantilever can be assumed as quasi-static. The time needed for a flow structure of size η to pass the cantilever is about $50\mu\text{s}$, which is much slower than the time scales corresponding to the first resonant modes of all cantilevers currently used (see table 3.2). Therefore, for the above-mentioned flow situation all cantilevers face laminar inflow only. Hence, non-linearities due to the dynamical response of the cantilever are not to be expected. However, as for any finite size local probe limitations might occur for turbulent flows with smaller Kolmogorov lengths and/or faster mean velocities, i.e. for flow structures that pass the cantilever in a time close to $2\pi/\omega_{fluid}$. This event has not been studied yet and needs to be examined in the future.

During calibration the 2d-LCA is mounted on a turning table, which is positioned in front of the tunnel outlet. The cantilever is aligned along the rotational axis of the turning table (see fig. 4.1). While calibrating, the voltages of the relative x- and y-components of the reflected spot along the 2d-PSD (see also appendix D) are recorded for different angle of attack and flow velocities. This process has been completely automated using various hardware components like A/D-converters for the operation of the wind tunnel or a stepper motor for driving the turning table. The control of the whole system is done by a LabVIEW-program that was developed in the working group TWiSt at the University of Oldenburg. The labview program is explained in detail in appendix B.

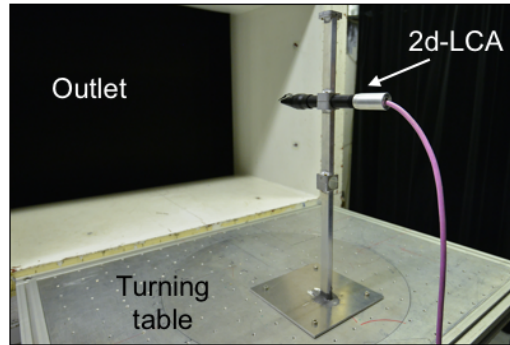


Figure 4.1: Setup for the calibration of the 2d-LCA.

4.1 Shape of the calibration plane

The shape of the calibration plane differs for individual cantilever design. To begin with, fig. 4.2 shows exemplarily a calibration plane for a cantilever of $160\mu\text{m}$ in length with a $50\mu\text{m}$ -vane in the ranges of $\pm 35^\circ$ and 4-12m/s with interval steps of 5° and 1m/s. As mentioned before, the plot shows the relative x –and y-coordinates of the laser spot along the 2d-PSD in terms of voltages. For clarity reasons, same velocities are connected with red lines and same angle of attack with blue lines.

As can be seen, the boomerang-shaped curves that correspond to same velocities become wider towards increasing flow velocities. Thus, the resolution within the calibration plane is not equally distributed. This is a consequence of the quadratic relation between the drag force and flow velocity (eqn. (2.1)) and a non-constant value of $c_d(u)$ (see section 3.2). It is also striking that the upper wing corresponding to positive angle of attack is rounder than the part that covers negative inflow angle. Tests have shown that this effect is related to the orientation of the whole sensor with respect to its main lengthways axis. Fig. 4.3 demonstrates this imbalance between both wings for different sensor orientations that correspond to angle of -9° , -3° , 0° , $+3^\circ$ and $+9^\circ$. One can see that for increasing alignment angle the shape of the wings corresponding to positive angle of attack gets more pronounced, whereas the other wing corresponding to negative angle is shrunk. Thus, for good reproducibility the orientation must remain preserved.

Next, the shape of a calibration plane for a cantilever of $160\mu\text{m}$ in length, but without a vane is examined (fig. 4.4). The calibration has been recorded for the same ranges of velocities and inflow angle as for the cantilever with vane. In direct comparison, one notices a change of the shape for the trajectories corresponding to same velocities. The previously observed boomerang-shaped

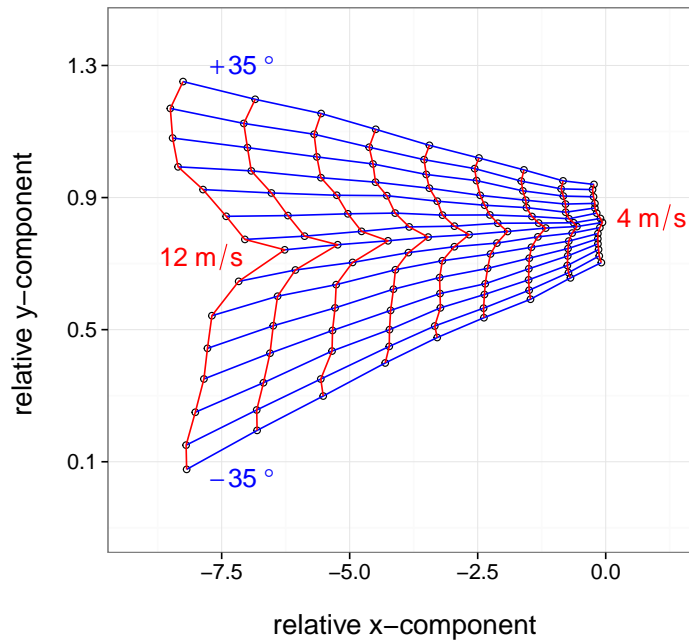


Figure 4.2: Calibration plane for a cantilever of $160\mu\text{m}$ in length and a vane of $50\mu\text{m}$ in height.

trajectories turned into simple arc-shaped curves. But even more important, the twisting direction of the cantilever has changed, i.e. for same angle of attack the cantilever without a vane twists in opposite direction as the cantilever with vane. It is believed that this effect is caused by lift forces acting on the cantilever. The total amount of twisting that is associated with the range along the y-axis is smaller. Note, that the range of the y-axis is only one third of the y-scale of figure 4.2. This shows the significant impact of the vane upon the twisting behavior of the cantilever.

4.2 Accuracy of the calibration plane

The calibration planes for both types of cantilevers (with vane and without vane) have in common that the resolution power increases towards higher velocities. In order to quantify this, the calibration in fig. 4.2 is considered again. The average distance between the two lowest velocities (4m/s and 5m/s) in terms of voltage is about 0.6V, whereas the average distance for the last two highest velocities (11m/s and 12m/s) is 1.3V. The A/D-converter (type Data Translation 9816A) used here features a resolution of 16bit and is operated in a range of

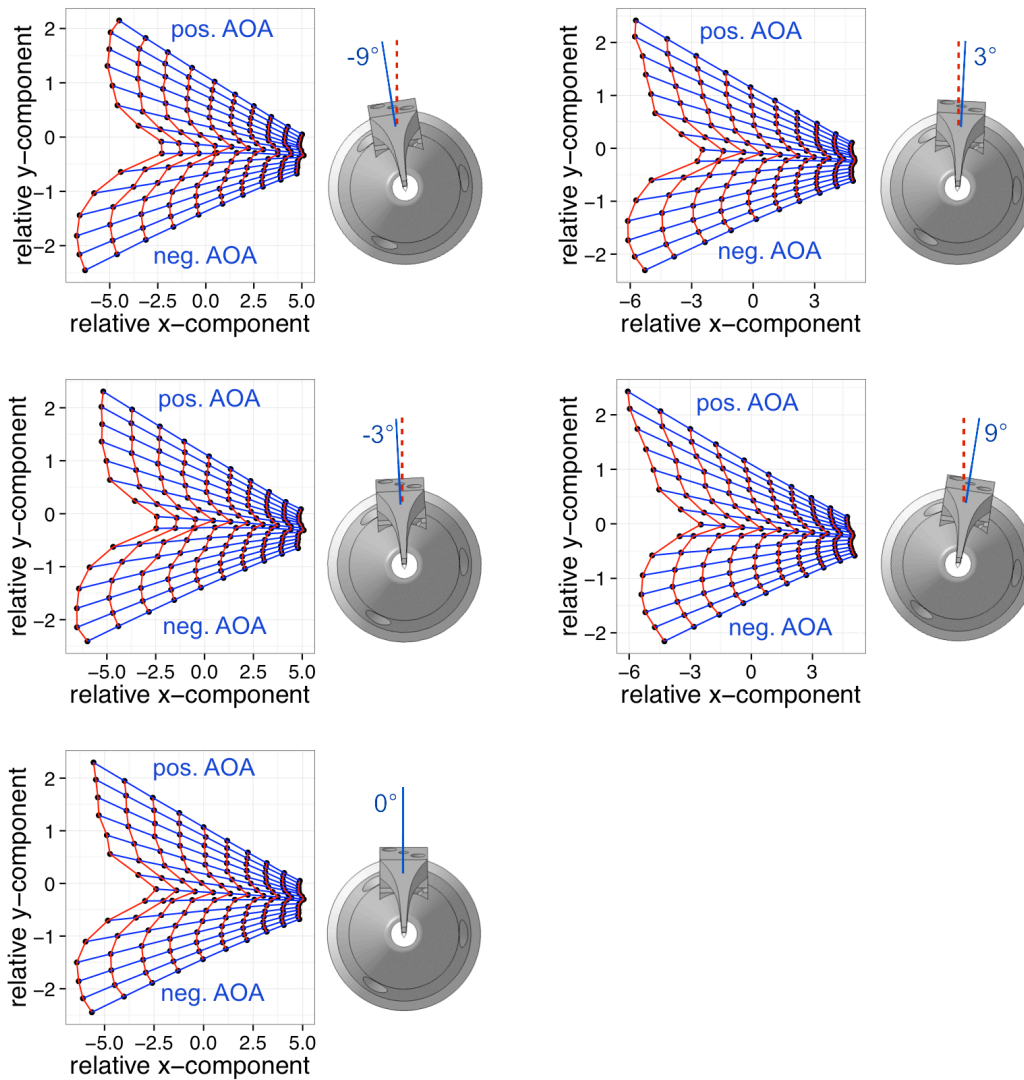


Figure 4.3: Calibration planes obtained with a cantilever of $140\mu\text{m}$ in length and a vane of $50\mu\text{m}$ in height for different orientations that correspond to -9° , -3° , 0° , $+3^\circ$ and $+9^\circ$ with respect to the lengthways axis of the 2d-LCA (red dashed line).

$\pm 10\text{V}$ ^a. Thus, the A/D-converter provides about 2000 discrete values for resolving velocities between 4-5m/s and even about 4200 for velocities between

^aThe number N of total discrete points or levels provided by the A/D-converter with a resolution of n -bit is given by $N=2^n$. The resolution in terms of voltage is calculated by dividing the voltage range (here 20V) by N .

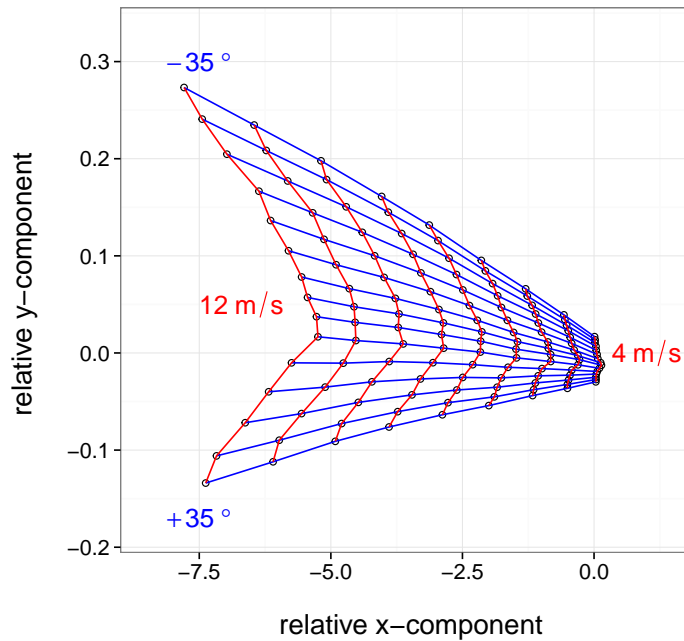


Figure 4.4: Calibration plane for a cantilever of $160\mu\text{m}$ in length without vane.

11-12m/s. These values are equivalent to velocity resolutions of $5 \cdot 10^{-4}\text{m/s}$ and $2.3 \cdot 10^{-4}\text{m/s}$, respectively. Similarly, an analogous estimation can be done for the resolution of the angle of attack according to fig. 4.2. This time the average distance between two points along the curve of the largest velocity (12m/s) is 0.2V. This corresponds to about 650 discrete values and a theoretical average resolution of $5^\circ/650 = 0.008^\circ$. For the lowest velocity of 4m/s the average distance between two points is only 0.02V. Consequently, the resolution drops to 0.08° in average.

In the case of the cantilever without vane (see fig. 4.4) the average distance between two points along the 4m/s curve is 9mV and thus a average resolution of only 0.17° can be achieved. For shorter cantilevers and even lower velocities the angular resolution continues to drop.

In addition, the impact of measurement noise becomes increasingly significant. Fig. 4.5 a) and b) show the standard deviations in terms of error bars for the three lowest trajectories of velocity of the calibration planes shown in fig. 4.2 and 4.4. The comparison makes it clear that a much better accuracy is achieved when using a cantilever with vane.

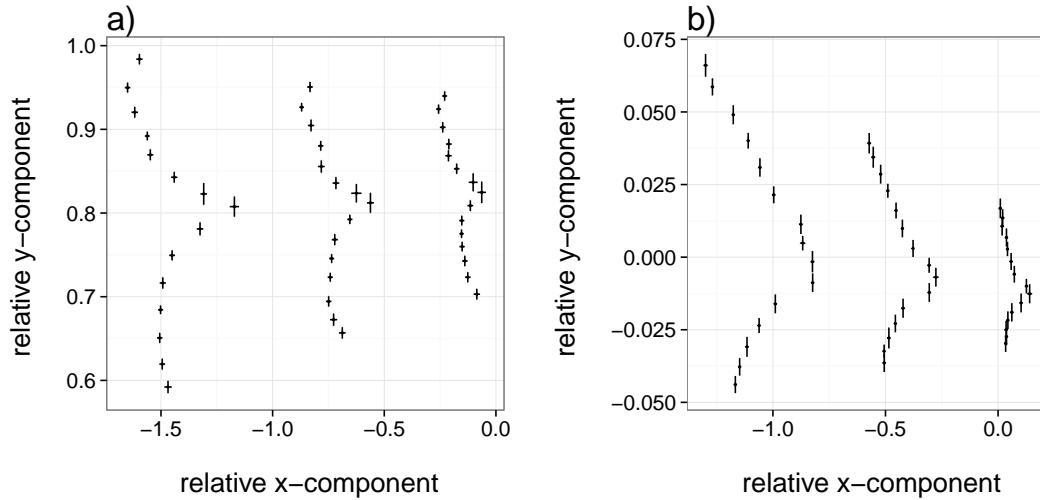


Figure 4.5: Standard deviations for the three lowest velocities of calibration planes by a cantilever with vane (a) and without vane (b).

4.3 Optimization of the calibration process

As described in the beginning of section 4 the calibration points are obtained from x- and y-positions of the laser spot along the 2d-PSD in terms of voltage signals that are recorded for predefined combinations of velocities and inflow angle. The acquisition of each calibration point takes about 10 seconds in average (including the time needed by the wind tunnel and the stepper motor). A calibration in the range of 3-12m/s and $\pm 40^\circ$ with steps of 1m/s and 1° takes about 2hours. Therefore, it is worth investigating how many calibration points are actually necessary in order to obtain good results in a reasonable time. For this purpose, a fine-meshed calibration plane in the ranges of 3-12m/s and $\pm 40^\circ$ with steps of 0.5m/s and 1° was recorded. The original calibration is „thinned-out“ (one or both step sizes are increased) in three steps and after each step the coarser calibration is used for allocation of raw signals from the same time series of a turbulent flow. Fig. 4.6 a)-d) show all four calibration planes. The new step sizes are: 1m/s and 1° (b), 1m/s and 3° (c), 1m/s and 5° (d).

The allocation of the measured data is done based on a method as introduced in [34]. The procedure is described in appendix F. The evaluation of the velocity and inflow angle obtained by means of the different calibrations is done by comparing basic data as listed in table 4.1. It is found that the deviations between the finest and the coarsest calibrations are in the range of about 0.2-0.9% for all parameters evaluated. In the following, calibrations with a coarse step

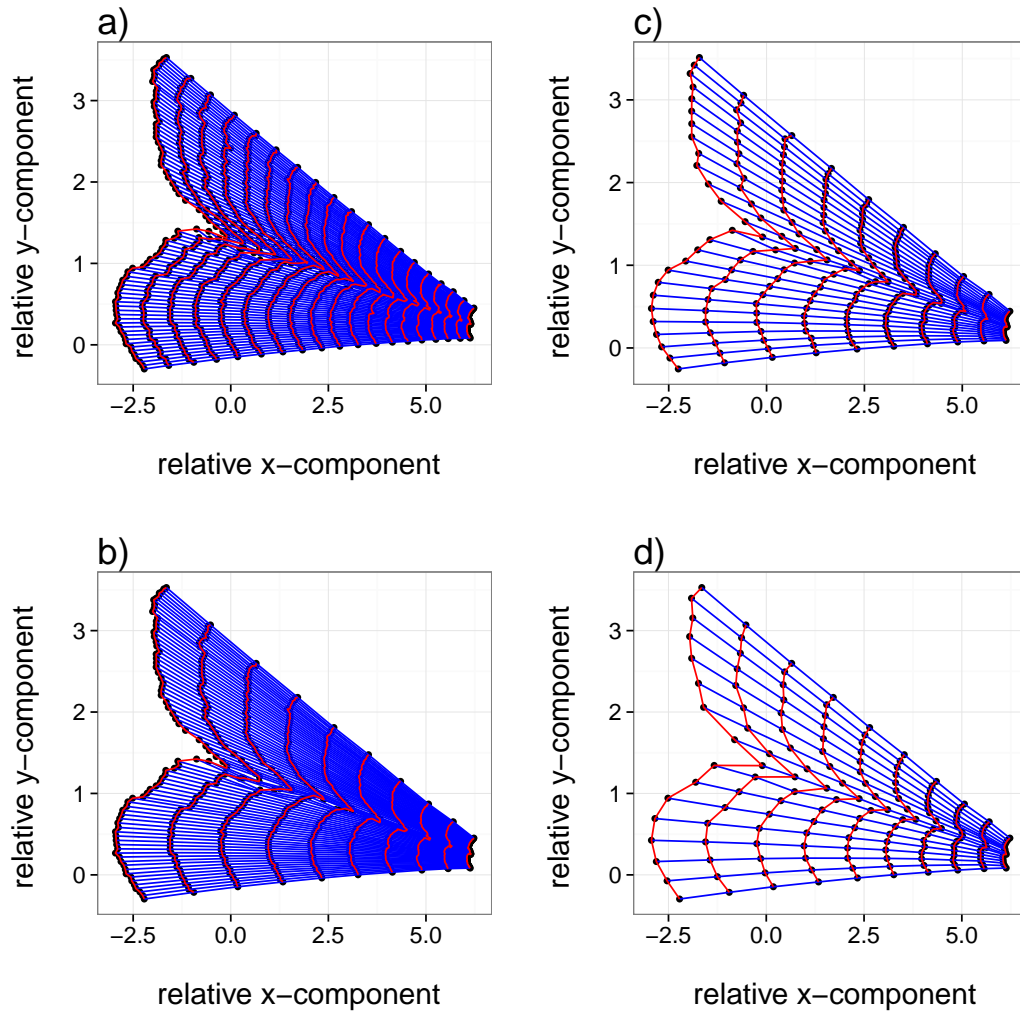


Figure 4.6: Calibration planes recorded with the following step sizes for velocities and angle of attack: 0.5m/s and 1° (a), 1m/s and 1° (b), 1m/s and 3° (c) and 1m/s and 5° (d).

size of 1m/s and 5° will be used.

4.4 Angular range of cantilevers equipped with vanes

In the following, the angular range and the impact of the vane will be examined. To begin with, larger sections of the previously discussed calibrations from fig. 4.2 and 4.4 are considered. Fig. 4.7 shows the calibration for large angle of

| step sizes [m/s] / [°] | mean velocity [m/s] | min./ max. velocity [m/s] | mean AOA [°] | min./ max. AOA [°] | TI in % |
|------------------------------|---------------------------|---------------------------------|--------------------------|-----------------------|------------|
| 0.5 / 1 | 9.20 $\sigma = 1.33$ | 3.38 / 16.94 | -1.08 $\sigma = 6.71$ | -35.13 / 39.73 | 14.44 |
| 1 / 1 | 9.19 $\sigma = 1.33$ | 3.41 / 17.00 | -1.07 $\sigma = 6.72$ | -34.99 / 39.52 | 14.46 |
| 1 / 3 | 9.19 $\sigma = 1.32$ | 3.41 / 17.03 | -1.07 $\sigma = 6.71$ | -34.97 / 39.55 | 14.36 |
| 1 / 5 | 9.22 $\sigma = 1.35$ | 3.41 / 17.06 | -1.12 $\sigma = 6.71$ | -35.06 / 39.46 | 14.59 |

Table 4.1: Overview of the basic parameters that were obtained from four calibrations with different step sizes of velocity and angle of attack.

attack in the range of $\pm 90^\circ$ for the cantilever with vane (a) and for the cantilever without vane (b).

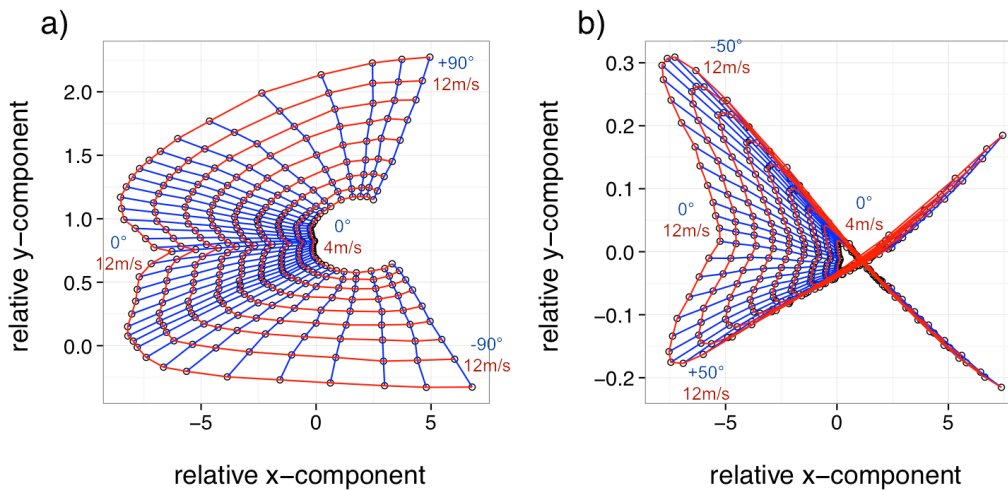


Figure 4.7: Calibration plane for a cantilever of $160\mu\text{m}$ in length and a vane of $50\mu\text{m}$ in height (a) and without a vane (b) for an angular range of $\pm 90^\circ$.

It is striking that the calibration plane of the cantilever with vane remains

unique, i.e. there are no ambiguities within the entire plane. The distances between paths of same inflow angle (blue lines) even become larger towards greater angle. On the contrary, the calibration plane obtained from the cantilever without vane collapses for inflow angle exceeding a range of about $\pm 50^\circ$.

For comparison, the same calibration plots have been generated for a standard x-wire (Dantec 55p51). Fig. 4.8 shows a calibration in the ranges of 4-12m/s and angle of attack of $\pm 30^\circ$ (a) and a larger section with angle of attack of $\pm 90^\circ$ (b). The figure shows that the x-wire generates a calibration plane that is unique within a limited angular section only. For more extreme inflow angle exceeding this section, the calibration begins to fold inside the center and loses its uniqueness as in the case of the cantilever without vane. Because of this overlapping or folding, calibration values in these regions are assigned to multiple inflow angle.

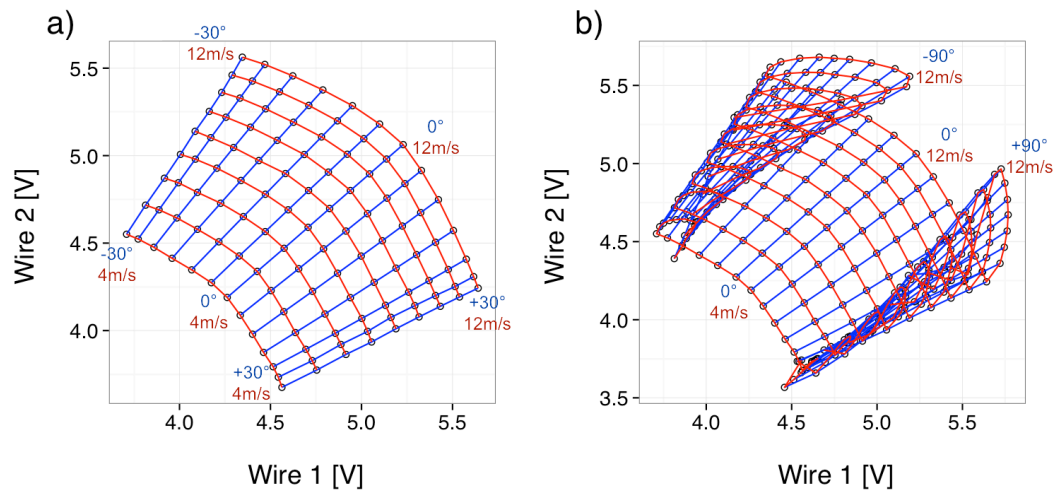


Figure 4.8: Calibration plane for a x-wire (Dantec 55p51) for an angular range of $\pm 30^\circ$ (a) and for $\pm 90^\circ$ (b).

4.5 Reproducibility of calibration planes

The reproducibility of the calibration can be used to assess the signal stability of the 2d-LCA over time. Also, it seems reasonable to say that measured data can be only trusted if the calibration remains unchanged after the measurement. For that reason, the following investigation places a focus on the deviations between three calibration planes that were recorded over a day. The time between

the calibrations was about half hour and had been used for measurements of wake flows.

The plot in fig. 4.9 gives an overview of all three calibrations with same ranges of 4-13m/s and $\pm 35^\circ$.

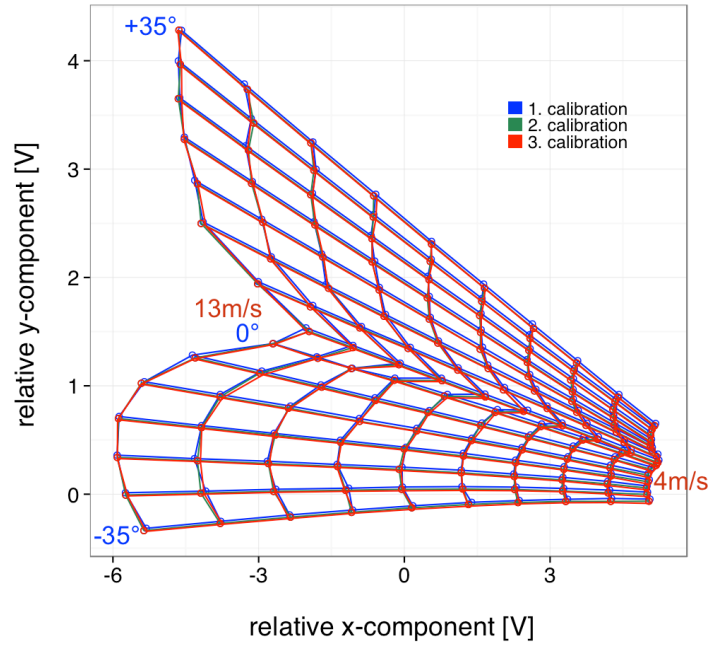


Figure 4.9: Three calibrations by the same cantilever recorded in intervals of half hour.

The deviations between the three calibrations are marginal and almost not visible from the plot. Still, for defining the reproducibility it is important to study the impact of these deviations. To do so, the recorded calibration points of the last calibration are applied as a raw data set for the first calibration. Thus, the measured x- and y-values of the later calibration for each combination of velocity and angle of attack are allocated using the first calibration. The difference between the first calibration points and the corresponding allocated values gives the deviations in terms of velocities and angle of attack. These deviations are graphically illustrated along the first calibration plane in fig. 4.10 for the velocities (a) and the angle of attack (b).

As can be seen, the biggest deviations in terms of velocity occur in the center region around 0° with a peak value of about 0.18m/s. For the angle of attack a large deviation of about 2° is apparent in the areas of lowest speeds (4-5m/s). With reference to the longitudinal and transverse velocity component, it follows

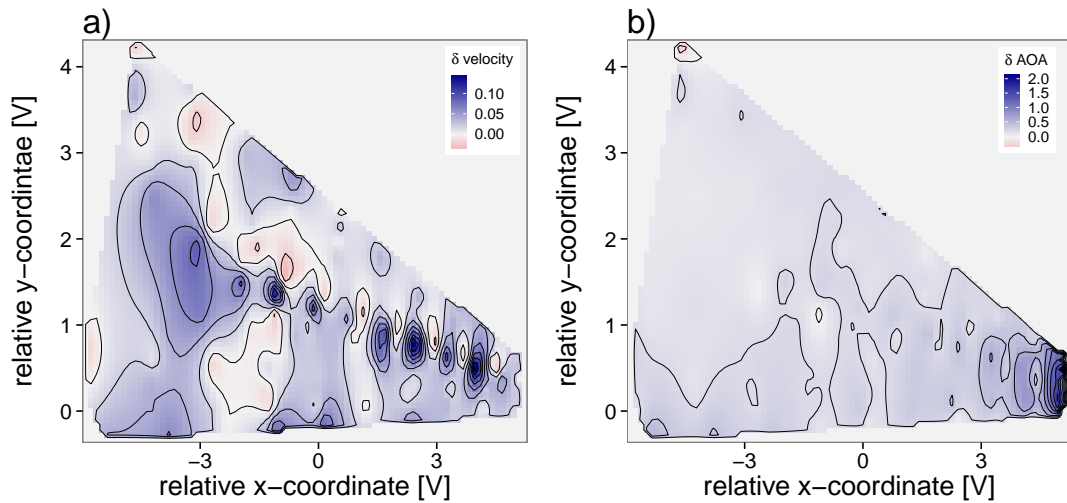


Figure 4.10: Deviations between two calibrations with the 2d-LCA in terms of velocities (a) and inflow angle (b).

that the average deviation is 0.02m/s and 0.04m/s, respectively.

In order to better assess this result, the same analysis has been repeated for a standard x-wire (type DANTEC 55P51). Fig. 4.11 shows all three calibration planes plotted on top of each other. In contrast to the 2d-LCA calibration shown in fig. 4.9 the deviations between the x-wire calibrations clearly follow a trend, i.e. the calibrations drift into one direction.

The impact of this shifting upon the measured raw data is again investigated using the procedure explained above. The deviations in terms of velocity and angle of attack are presented in fig. 4.12 a) and b), respectively.

The plot exhibits the biggest velocity deviations of about -0.2m/s in the upper right region that corresponds to positive angle of attack and velocities between 12-13m/s. The largest deviations of the angle of attack of about -0.8° are located in the region of the lowest velocity and negative extreme angle of attack. This analysis leads to an average deviation of the longitudinal component of 0.06m/s and 0.05m/s for the transverse component.

In conclusion, one can say that the reproducibility of the 2d-LCA calibrations improves towards increasing velocities and more extreme angle of attack. The biggest deviations that are found for small velocities and angle of attack are related to the findings in section 4.2. In contrast, the x-wire calibrations show a clear drifting behavior that becomes worse with time but can also be corrected. The drifting is much likely caused by the electronics and the aging of the wires. For the cantilever, it is expected that aging can be neglected as silicon is very

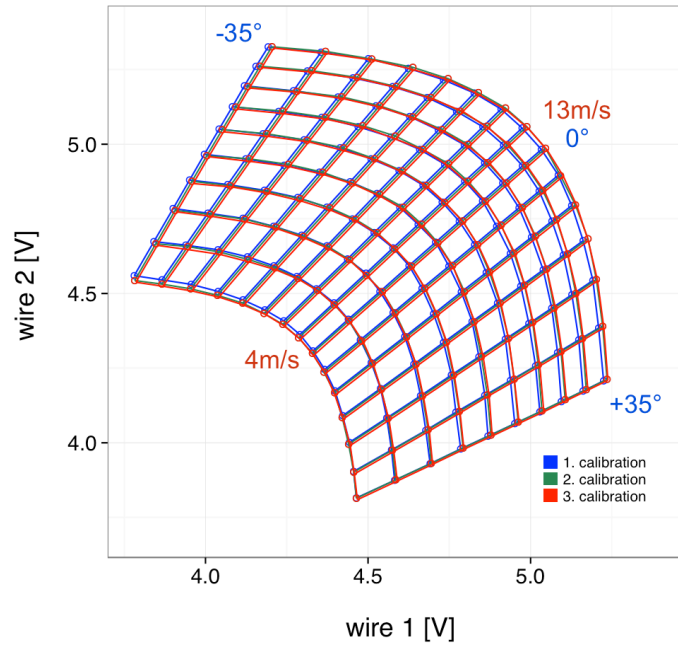


Figure 4.11: Three calibrations with the same x-wire recorded in intervals of half hour.

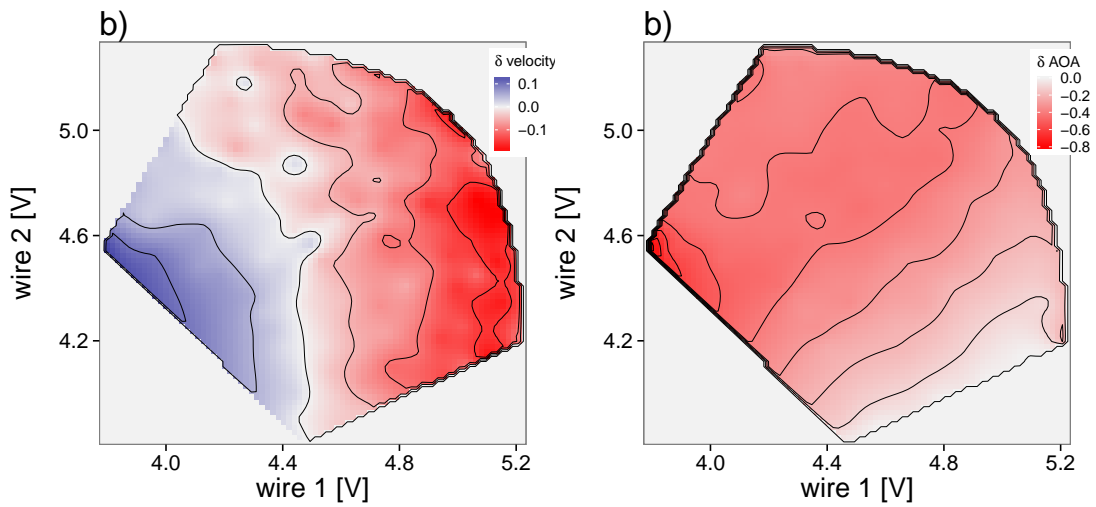


Figure 4.12: Deviations between two calibrations with the x-wire in terms of velocities (a) and inflow angle (b).

durable.

Further tests have revealed that if an x-wire is disconnected from the anemometry system (STREAMLINE) between two calibrations, the deviations are much larger. The reason for this is a slight change of electrical resistance at the contact points of the plug. This limits the mobility of x-wires insofar as it is almost not possible to perform measurements without an on-site calibration unit. This limitation does not apply for the 2d-LCA.

Chapter 5

Measurements

In the following chapter measurements of wake turbulence performed with the 2d-LCA will be presented. For the purpose of validation all measurements were accompanied by commercially available measurement techniques such as hot-wires or x-wires.

5.1 Measurements in the wake of a cylinder

Measurements with two 2d-LCAs of third kind (one with a vane-equipped cantilever and one without a vane) and an x-wire were carried out in the turbulent wake flow generated by a cylinder of 2 cm in diameter. All three anemometers were aligned 80 cm behind the cylinder. At this distance the wake flow reaches a well-developed turbulent state. Two data sets were recorded simultaneously (2d-LCA with vane and x-wire). The third data set obtained with the 2d-LCA without vane had been recorded at the same day. Although, simultaneous measurements with all three anemometers would be possible, it has been preferred to use the same 2d-LCA body with both types of cantilevers in order to absolutely eliminate any effect due to the sensors itself when comparing the different designs. Even though all 2d-LCA bodies share the same design, smallest tolerances in the alignment of components can not be excluded.

The measurements took place in the wind tunnel of the University of Oldenburg. The table 5.1 presents all characteristic parameters of the setup.

General data evaluation and one-point statistics

To begin with, the figure 5.1 exemplarily shows 10.000 raw data points (voltage signals) of each anemometer plotted in the corresponding calibration plane. These plots indicate whether the borders of the calibration plane completely

| | |
|-------------------------------------|--|
| wind velocity | 12 m/s |
| cylinder dimensions | diameter: 2 cm length: 60 cm |
| 2d-LCA (first) | Cantilever length of $160\mu\text{m}$ with vane of height $50\mu\text{m}$ |
| 2d-LCA (second) | Cantilever length of $160\mu\text{m}$ without vane |
| x-wire | type: Dantec 55p51 wire length: 1.25mm (sensitive) |
| sampling frequency | 60kHz (low-pass filter at 30kHz) |
| number of Data points | 8.000.000 (for each anemometer) |
| Reynolds number Re | 16.900 |
| Taylor-Reynolds number Re_λ | ≈ 380 |

Table 5.1: Overview of the setup parameters.

enclose the measured values. As can be seen, the calibration limits of 5-14m/s and $\pm 35^\circ$ are sufficient in order to allocate all raw data into velocity and angular data. The allocation is done using a slightly altered method as introduced in [34]. All details of this procedure are found in appendix F.

Next, short sections of the time series (1000 samples) of the absolute value of the velocity (fig. 5.2) and the angle of attack (fig. 5.3) are inspected. The evaluation allows for a qualitative comparison between all anemometers. From the time series of the absolute value of the velocity one can see that the overall shapes of all three signals look similar at first sight. The differences in the time series of the angle of attack are slightly larger. Here, the series obtained with the x-wire is more smoothed in comparison.

It should be borne in mind, that equal trends between all three data sets should not be expected as the anemometers were either spaced apart by 20 cm or measurements were not conducted simultaneously.

In table 5.2 the key parameters that characterize the flow are listed. The parameters include mean and extreme values for the absolute value of the velocity and the angle of attack, the integral and Taylor lengths and the turbulence intensity (TI). In addition, the variances for the absolute values of the velocities are given. The integral lengths were calculated according to eqn. (1.25) by means of an exponential fit as described in section 1.2.3. The Taylor lengths were estimated using eqn. (1.26) and the Löfdahl-Aronson approach for the derivative $\frac{\partial u}{\partial x}$ (see section 1.2.6). The values in brackets correspond to the alternative and

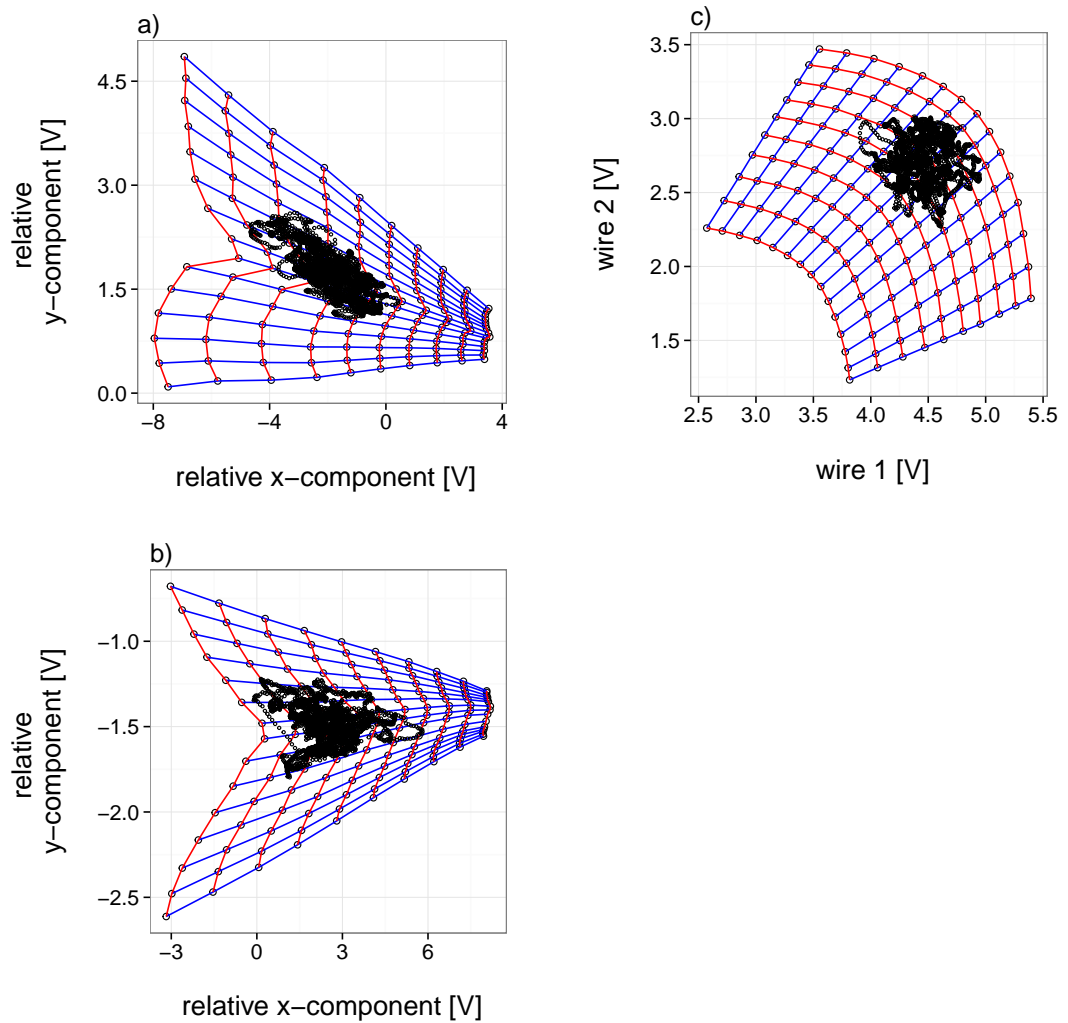


Figure 5.1: 10.000 raw data points of each anemometer (2d-LCA with vane (a), 2d-LCA without vane (b) and x-wire (c)) plotted in the corresponding calibration plane.

more established procedure that makes use of the positive curvature of the autocorrelation (also see section 1.2.6). Both methods deliver comparable values. It is notable that all three sensors are also consistent with the mean values of the velocity and angle of attack. Moreover, the values of Kolmogorov lengths (also calculated using the Lödahl-Aronson method) agree well. Differences become apparent for the integral length measured with the x-wire that is smaller by about 5mm and 7mm when compared to the 2d-LCA with vane and without

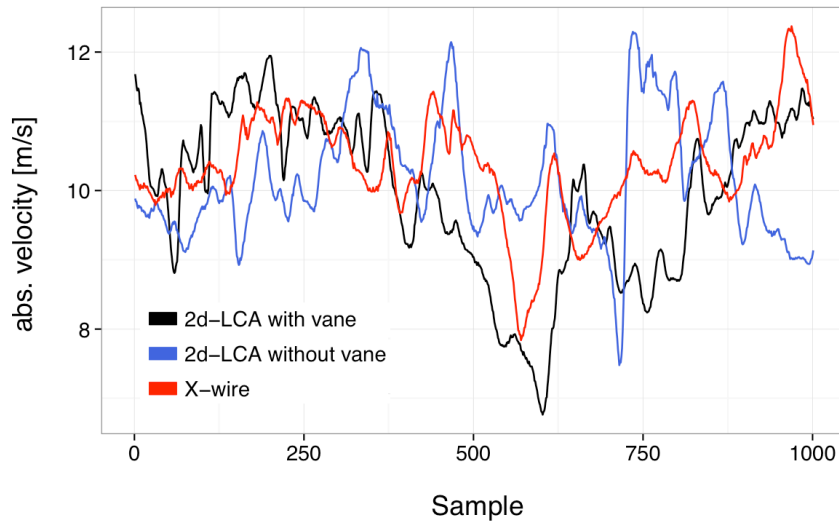


Figure 5.2: Time series of 1000 samples for the absolute value of the velocity measured by all three anemometers.

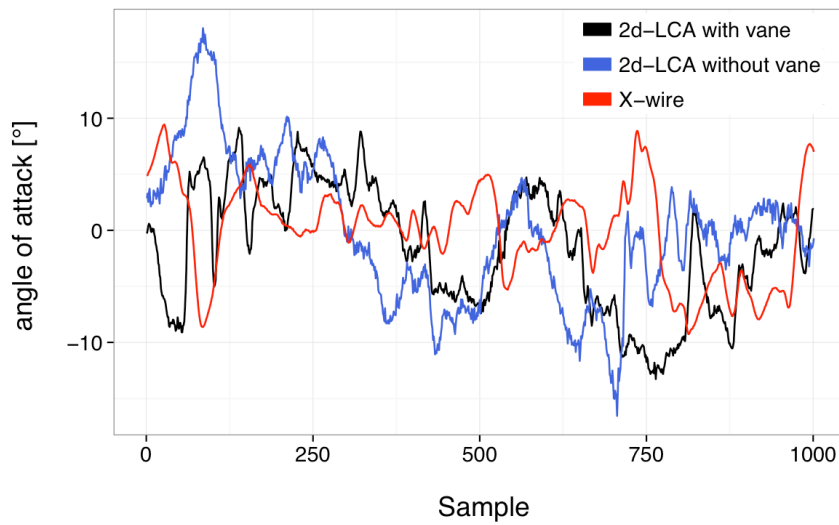


Figure 5.3: Time series of 1000 samples for the angle of attack measured by all three anemometers.

vane, respectively. The corresponding autocorrelation functions are found in fig. 5.4. Further minor deviations exist with regard to the minimal and maximal angle of attack. Lastly, the turbulence intensity and the variances determined

| Parameter | 2d-LCA with vane | 2d-LCA without vane | X-wire |
|-----------------------------------|------------------|---------------------|----------------|
| mean velocity [m/s] | 10.85 | 10.48 | 10.93 |
| min. / max. velocity [m/s] | 4.87 / 15.38 | 4.61 / 14.44 | 7.61 / 14.89 |
| mean angle of attack [°] | -0.07 | -0.25 | -0.68 |
| min. / max. angle of attack [°] | -23.07 / 23.55 | -24.12 / 22.62 | -21.32 / 20.53 |
| integral length L [mm] | 36.75 | 39.11 | 32.00 |
| Taylor length λ [mm] | 5.88 (5.53) | 6.03 (6.07) | 6.06 (6.17) |
| Kolmogorov length η [mm] | 0.27 | 0.26 | 0.29 |
| turbulence intensity TI [%] | 11.83 | 14.14 | 8.76 |
| variance σ^2 [m^2/s^2] | 1.65 | 2.16 | 0.92 |

Table 5.2: Key parameters of the flow measured with the 2d-LCA (cantilever with vane and without vane) and a x-wire.

from both 2d-LCA data sets are larger. Here, the 2d-LCA with a vane sees the highest turbulence intensity and the largest variance, whereas the x-wire refers to the smallest values of both quantities. This behavior is attributed to the low frequency content of the signal as will be discussed in the next section.

Two-point statistics

In the following, the spectral densities of all three data sets are analyzed. For that purpose the individual velocity components and the absolute values are compared between the anemometers. All time series were normalized in the same way. Figure 5.5 regards the spectral densities of the longitudinal components and figure 5.6 represents the transverse component. Finally, figure 5.7 shows the spectral density that corresponds to the absolute value of the velocity. All power spectra were averaged and normalized by the absolute power for ease of comparison. Averaging was accomplished by adding multiple spectra of shorter sections of 8×1024 samples. The longitudinal spectra of all anemometers correspond well in terms of general shape and dynamic behavior. In the region of 0.5-3kHz the spectra are not distinguishable at all. For higher frequencies a departure of the spectrum recorded with the 2d-LCA with vane is perceptible, whereas the spectra of the x-wire and the 2d-LCA without vane follow the same run up to a frequency of about 6kHz. In the high-frequency region

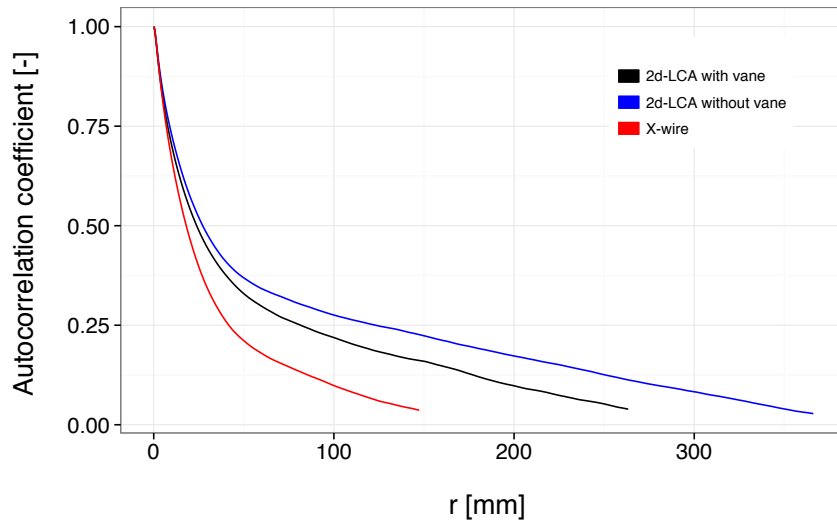


Figure 5.4: Autocorrelation functions of all three anemometers for the longitudinal velocity signal.

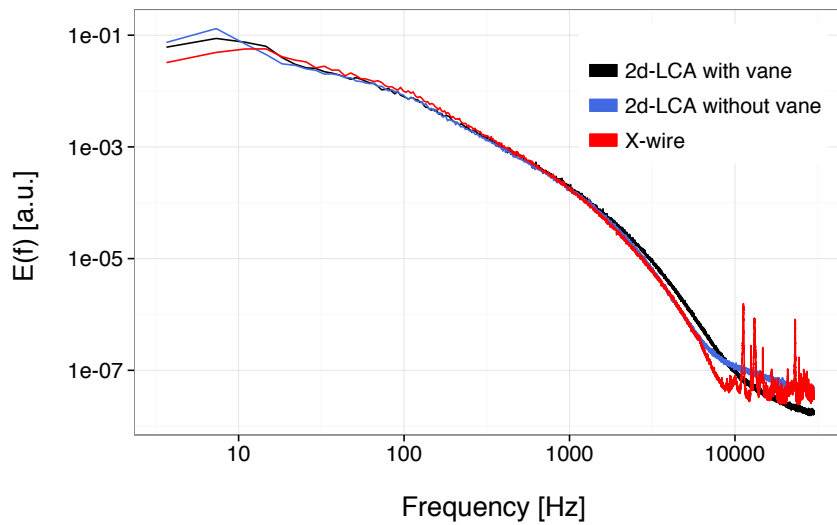


Figure 5.5: Spectral densities of all three anemometers for the longitudinal velocity signal.

where no more structures can be resolved, the x-wire spectrum is dominated by electromagnetic noise. Further deviations exist in the area below 10Hz. Here, one can see that the low-frequent content in the 2d-LCA spectra is much larger

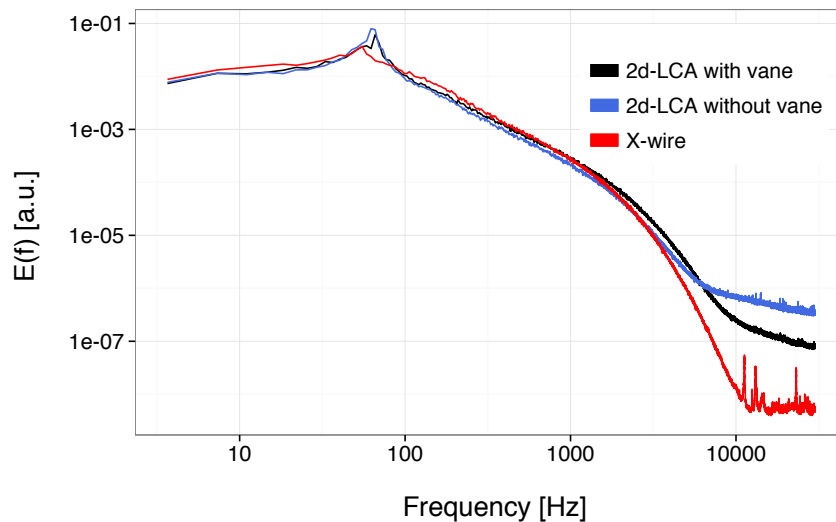


Figure 5.6: Spectral densities of all three anemometers for the transverse velocity signal.

than in the spectrum of the x-wire. This also explains the differences between the integral lengths and variances as shown in table 5.2. However, it should also be mentioned that low-frequent part of the spectrum is disadvantaged by a low number of data and thus features a larger statistical error.

The spectra of the transverse component agree well up to about 1.8kHz. For frequencies beyond that both 2d-LCA spectra show higher densities. The steeper slope in the x-wire spectrum is caused by spatial averaging, i.e. by smoothing small structures due the size of the sensing element. Such findings have been observed before in comparison measurements between hot-wires of different lengths [31, 33]. Moreover, the slope in the high-frequency region might also be influenced by the signal conditioning process (CTA-unit). Own measurements have shown that different spectra are obtained in this region with the same type of x-wire when using DANTEC CTAs or CTAs by A. A. Lab. The same findings are reported in [47].

The dynamic range of the spectrum of the 2d-LCA with vane is larger than the spectrum corresponding to the 2d-LCA without vane by about one order of magnitude. Still, both 2d-LCA spectra are lower than the x-wire spectrum. Similar findings have been reported in [34, 36].

Since the longitudinal velocity component is clearly dominating, the prevailing flow situation and thus the spectrum does not differ a lot from the spectrum for the absolute value of the velocity. Only in the high-frequency region the already mentioned deviation of the vane-equipped 2d-LCA spectrum is less pro-

nounced. A $-5/3$ - slope in accordance with eqn. (1.22) is found in the region between 0.1-1kHz. A steeper slope of about -2 is apparent between 4kHz and 7kHz.

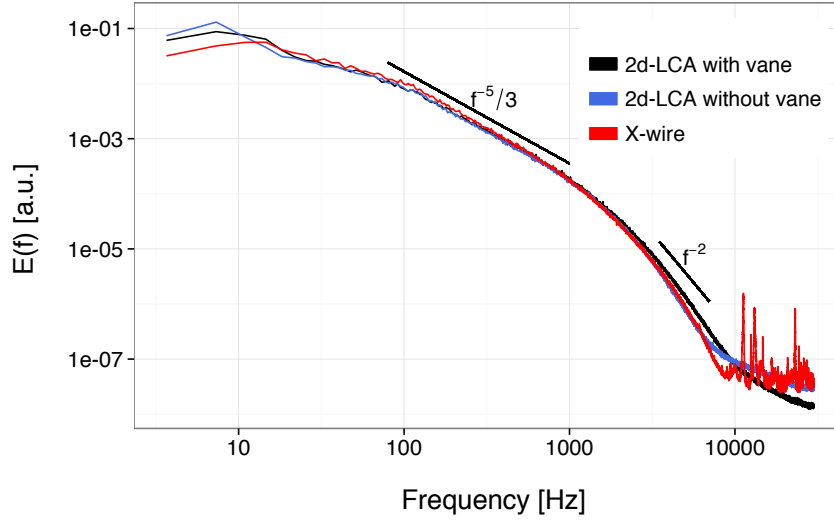


Figure 5.7: Spectral densities for the absolute value of the velocity. The black lines indicate a $-5/3$ and a -2 slope.

In the following, velocity increments according to eqn. (1.4) will be considered. The plot in fig. 5.8 shows the PDFs of longitudinal velocity increments for five different time lags τ . The values of τ used here are $\tau_1=0.167\text{ms}$, $\tau_2=1\text{ms}$, $\tau_3=2\text{ms}$, $\tau_4=10\text{ms}$ and $\tau_5=0.1\text{s}$ (from top to bottom). This corresponds to frequencies of $f_1 = 6\text{kHz}$, $f_2 = 1\text{kHz}$, $f_3 = 500\text{Hz}$, $f_4 = 100\text{Hz}$ and $f_5 = 10\text{Hz}$ within the spectrum shown in 5.5.

For the sake of clarity, PDFs of all anemometers corresponding to same τ were placed in groups, which afterwards were shifted against each other. In addition, the PDFs were normalized by the standard deviation of the increments. The PDFs show that all three anemometers reveal the same statistics in the increment data for all values of τ considered here. Small deviations between the anemometers can be identified for positive increments in the PDF corresponding to τ_1 only. Overall, the statistics show the well-known growing intermittent character of laboratory turbulence towards smaller scales.

The PDFs for the transverse velocity increments are shown in fig. 5.9. Unlike the PDFs of the longitudinal velocity increments, the statistics of the transverse increments are symmetric along the center. For a deeper investigation of the shapes of the PDFs, the form parameter λ_f^2 (eqn. (1.19)), the skewness S (eqn. (1.16)) and the kurtosis K (eqn. (1.16)) are evaluated with regard to τ . Fig.

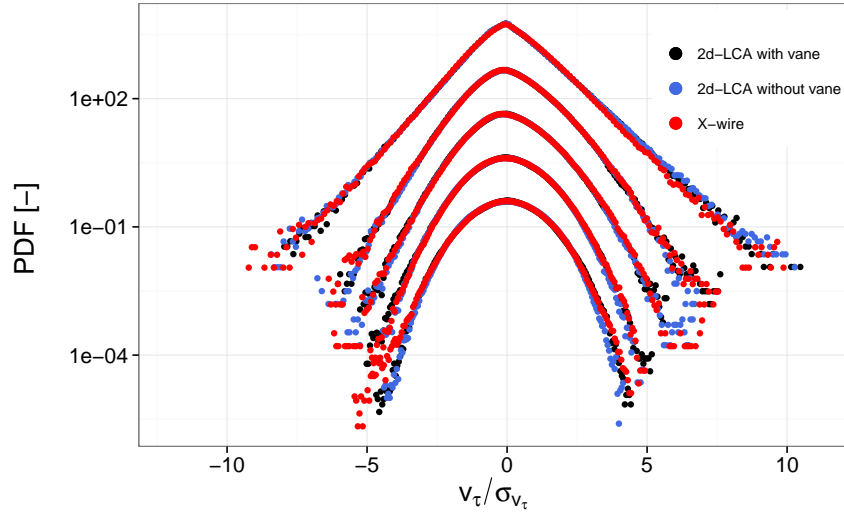


Figure 5.8: PDFs of increments for the longitudinal velocity component for the 2d-LCA with vane (black), the 2d-LCA without vane (blue) and the x-wire (red) for $\tau_1=0.167\text{ms}$, $\tau_2=1\text{ms}$, $\tau_3=2\text{ms}$, $\tau_4=10\text{ms}$ and $\tau_5=0.1\text{s}$ (from top to bottom).

5.10 a) - c) show the trends of λ_f^2 , S and K for the longitudinal component, respectively. From the trends of λ_f^2 and K one can see that the PDFs begin to take a Gaussian form ($\lambda_f^2 \approx 0$ and $K \approx 3$) for $\tau > 10\text{ms}$. The positive skewness^a, however, remains present up to $\tau \approx 80\text{ms}$.

Equivalent plots of λ_f^2 , S and K for the transverse component are shown in fig. 5.11 a) - c). Here, λ_f^2 and K start at higher values but essentially follow the same trend as for the longitudinal component, whereas the skewness parameter remains close to zero for all τ . A further possibility to compare the distributions of increments is to make use of structure functions as defined in 1.5. Fig. 5.12 shows a comparison of the first four structure functions of each anemometer for the longitudinal (a) and transverse (b) component. The structure functions were normalized by $\langle u_\tau^2 \rangle >^{\frac{p}{2}}$ and shifted against each other for a better representation. The deviations between the structure functions are in accordance with the trends observed for λ_f^2 and K (see fig. 5.10 a), c) and 5.11 a), c)).

Next, the data collected by the both anemometers will be used to verify theoretical expectations. Specifically that means that the structure functions for the longitudinal increments shall be used to verify the relation in eqn. (1.9) for the

^aNote that the PDFs shown here correspond to v_τ and not to v_r . Because of eqn. (1.1) the skewness parameters for v_τ and v_r have opposite signs

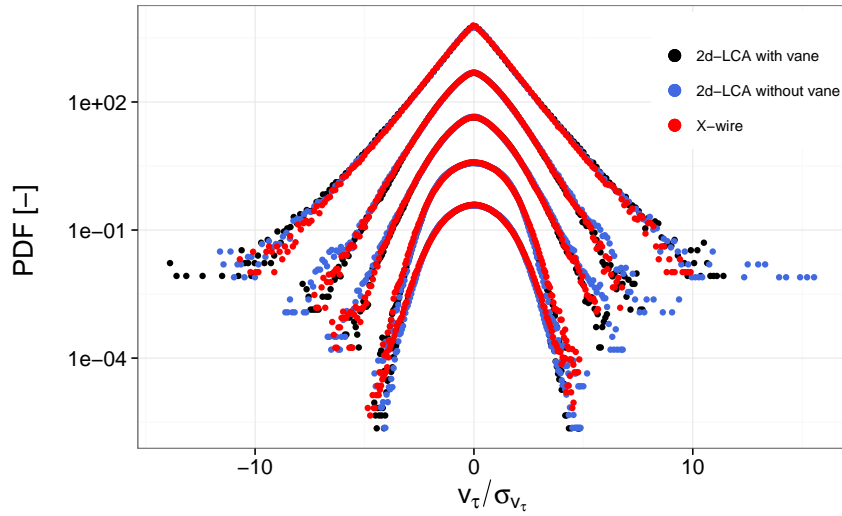


Figure 5.9: PDFs of increments for the transverse velocity component for the 2d-LCA with vane (black), the 2d-LCA without vane (blue) and the x-wire (red) for $\tau_1=0.167\text{ms}$, $\tau_2=1\text{ms}$, $\tau_3=2\text{ms}$, $\tau_4=10\text{ms}$ and $\tau_5=0.1\text{s}$ (from top to bottom).

scaling exponents ζ_p that is derived in K62. To do so, the ESS method (see section 1.2.1) is applied. Thus, the first 8 structure functions are plotted against the third structure function in a log-log plot and the scaling exponents ζ_p are determined from the slopes of the resulting graphs by means of linear fits. This approach is illustrated in fig. 5.13 a) for the 2d-LCA with vane, and in fig. 5.14 a) and fig. 5.15 a) for the 2d-LCA without vane and the x-wire, respectively. In the next step, the values of ζ_p obtained this way are plotted against p as shown in figures 5.14-5.15 b). This time a function according to eqn. (1.9) is fitted, from which the intermittency factor μ is determined. The values of μ found are 0.262 for the vane-equipped 2d-LCA, 0.264 for the 2d-LCA without vane and 0.233 for the x-wire. The values of μ found here are comparable to other experiments. In [37] μ was found to be 0.24 ± 0.003 for an one-dimensional LCA, [17] reports a value of 0.23 for hot-wire measurements in an open stream and [39] specifies μ to be 0.26 for an experiment in a turbulent channel flow that was also conducted with a hot-wire.

Next, the transverse structure functions $S_{u,t}^p$ are analyzed by means of ESST (see section 1.2.1). This procedure is based on ESS, but regards the faster velocity of the transverse cascade [25, 48, 49]. Thus, before determining the slopes from the plots of the p -order transverse structure functions against the third-order longitudinal structure function, the increments are rescaled by a factor of $3/2$.

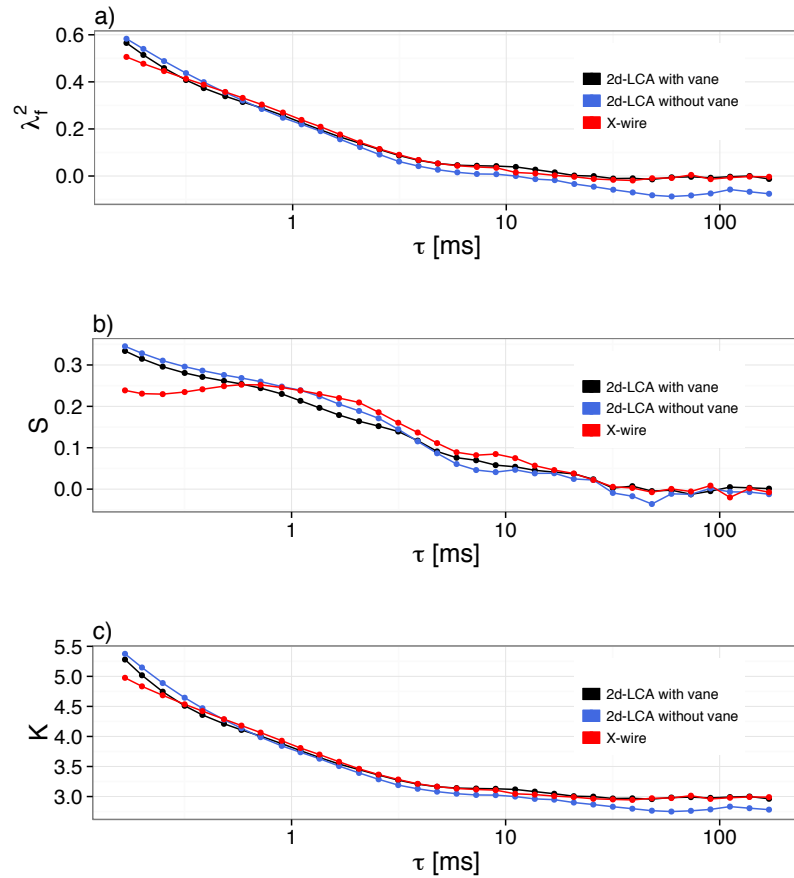


Figure 5.10: Formparameter (a), skewness (b) and kurtosis (c) for the longitudinal velocity increments against τ for all three anemometers.

In the following this factor will be referred to as the scaling factor s_f . The intermittency factors found for the transverse component are 0.291 for the 2d-LCA with vane, 0.235 for the 2d-LCA without vane and 0.295 for the x-wire^b. It is reasonable to believe that the smaller intermittency value of the 2d-LCA without vane is related to its weaker angular resolution that corresponds to the transverse velocity component.

For the data sets examined here the smallest difference between μ determined by means of ESS and ESST arises from the data sets provided by the 2d-LCAs, whereas the deviation for the x-wire is about twice as much.

^bIt should be stressed that the calculated intermittency factors strongly depend on the quality of the fit that is used to obtain the values of ζ_p .

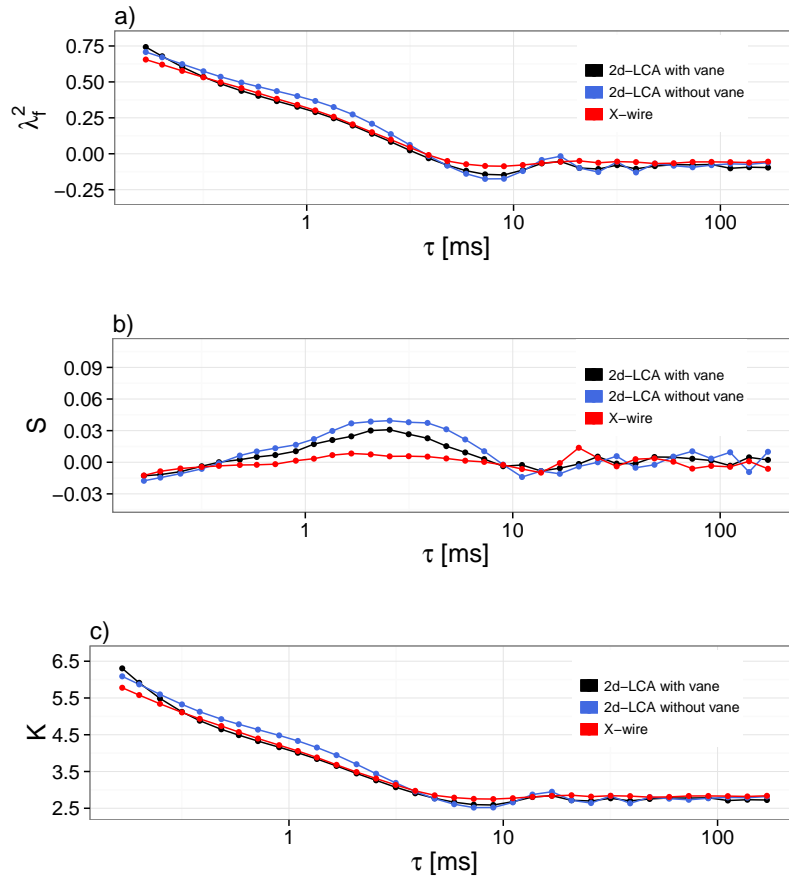


Figure 5.11: Formparameter (a), skewness (b) and kurtosis (c) for the transverse velocity increments against τ for all three anemometers.

The analysis based on two-point statistics provided so far shows that the 2d-LCA (regardless of the kind of cantilever) provides comparable results when compared to standard x-wires. However, statistical properties derived from higher-order structure functions ($S_v^6 - S_v^8$) suffer from a larger statistical error, as the number of data points is not very huge (8.000.000). Thus, extreme events become very rare and each of them has a tremendous impact. This effect should not be underestimated. Tests with the data sets revealed that removing only few of the most extreme longitudinal velocities leads to a notable overestimation of μ .

The dependence of s_f on μ (which is found for longitudinal structure function as well) indicates that the relation from eqn. (1.8) is not complete. Instead, the scaling should follow $S(s_f \cdot r) \propto r^{p/3 - \mu(s_f)/18p(p-3)}$.

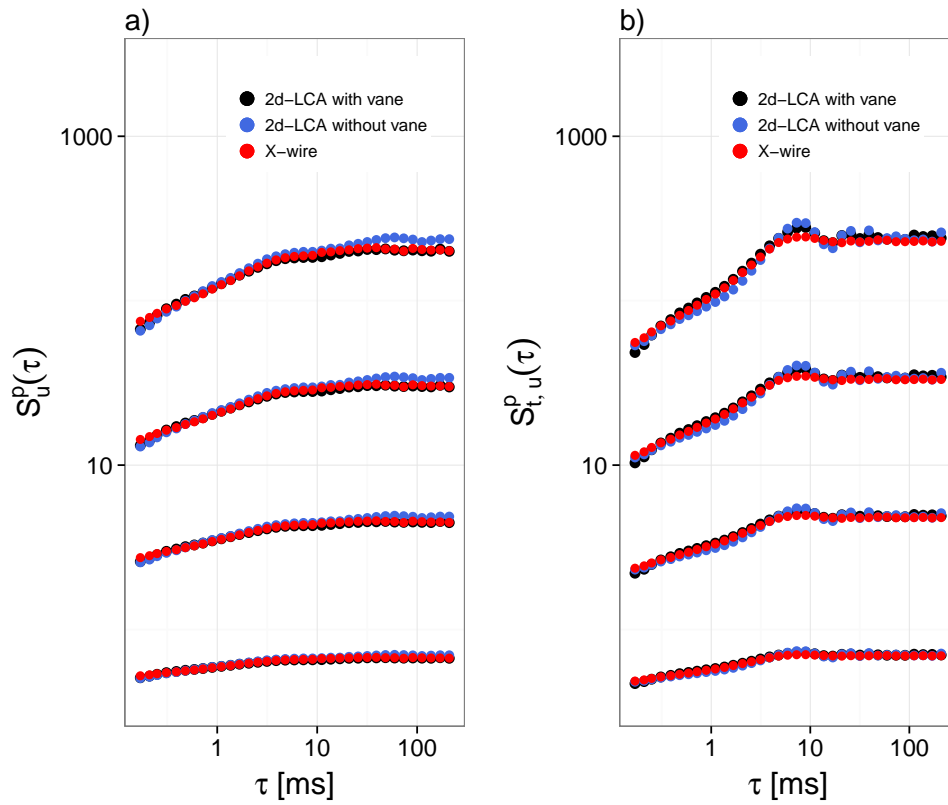


Figure 5.12: Longitudinal (a) and transverse (b) structure functions of order $p = 1, 2, 3, 4$ (from bottom to top) for all anemometers.

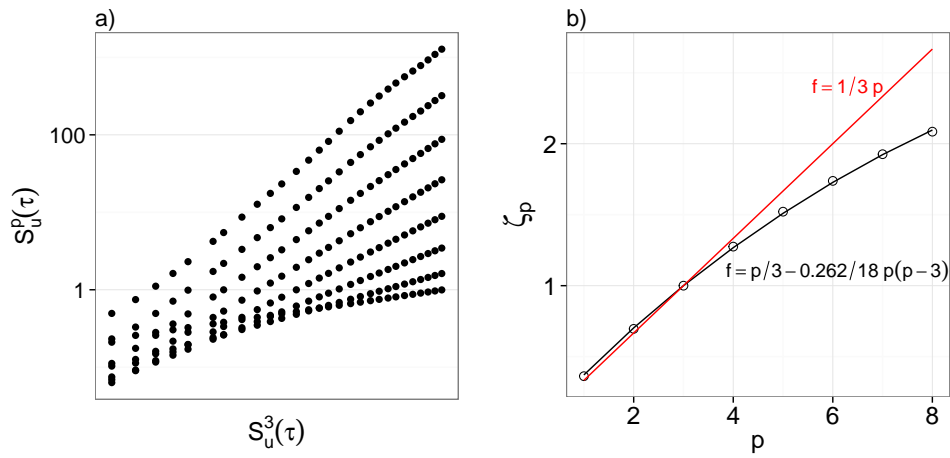


Figure 5.13: Structure functions of different orders p against the third structure function for the 2d-LCA with vane (a) and corresponding fit according to eqn. (1.9) (b).

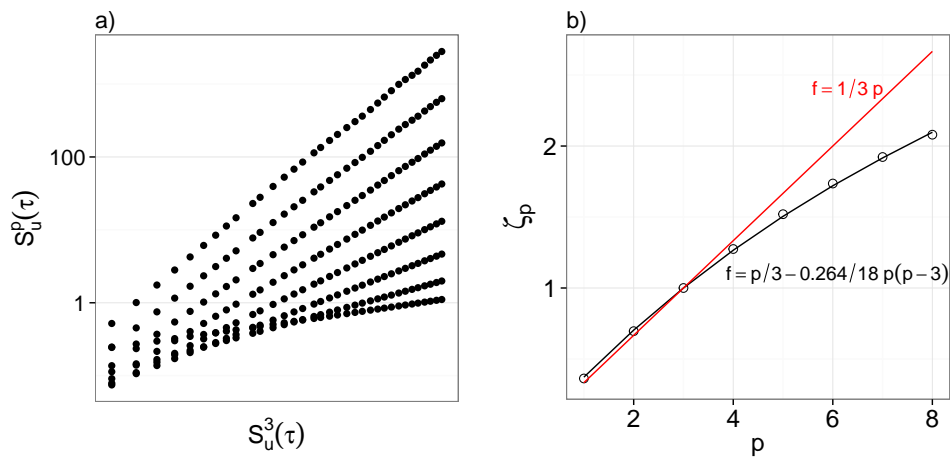


Figure 5.14: Structure functions of different orders p against the third structure function for the 2d-LCA without vane (a) and corresponding fit according to eqn. (1.9) (b).

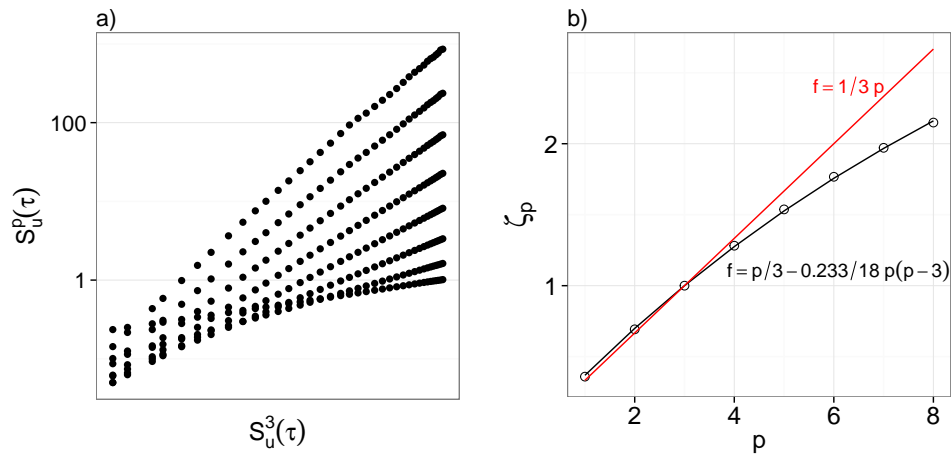


Figure 5.15: Structure functions of different orders p against the third structure function for the x-wire (a) and corresponding fit according to eqn. (1.9) (b).

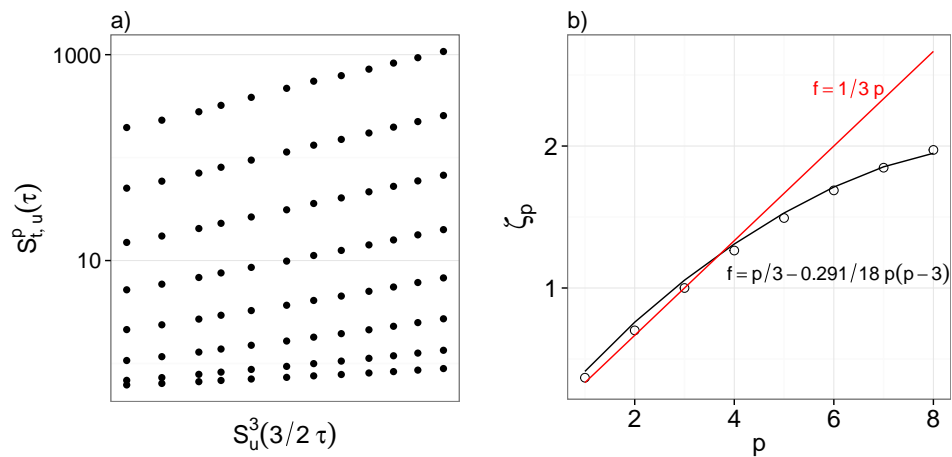


Figure 5.16: Transverse structure functions of different orders p against the third longitudinal structure function with rescaled τ for the 2d-LCA with vane (a) and corresponding fit according to eqn. (1.9) (b).

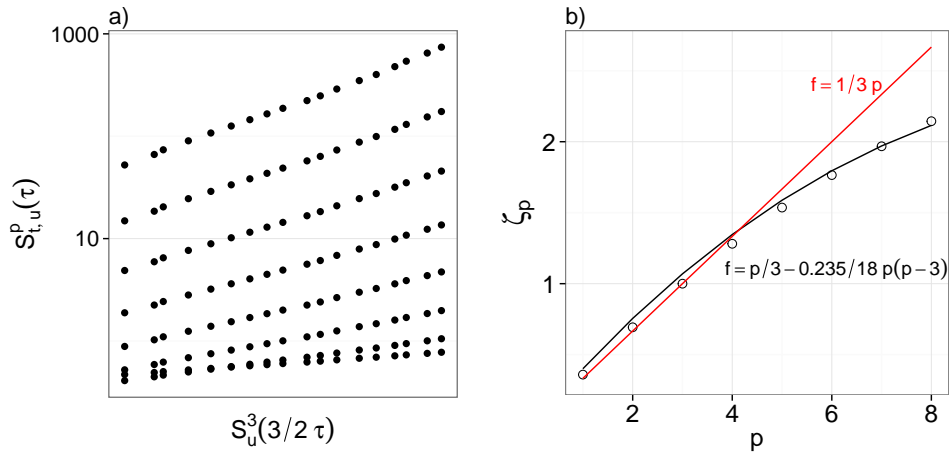


Figure 5.17: Transverse structure functions of different orders p against the third longitudinal structure function with rescaled τ for the 2d-LCA without vane (a) and corresponding fit according to eqn. (1.9) (b).

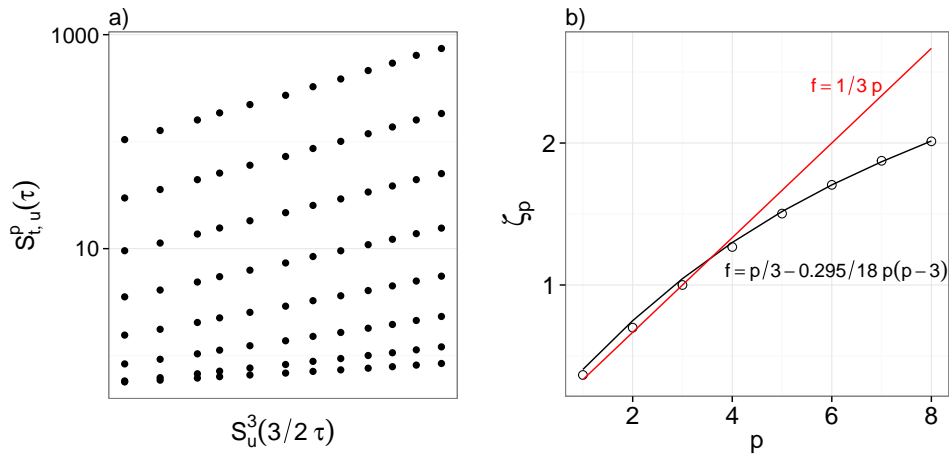


Figure 5.18: Transverse structure functions of different orders p against the third longitudinal structure function with rescaled τ for the x-wire (a) and corresponding fit according to eqn. (1.9) (b).

5.2 Flow with extreme angle of attack

The advantage of the cantilever with vane is the extended range of accepted angle of attack (see section 4.1) when compared to a cantilever without vane. In the following, the performance of the new design will be demonstrated by means of measurements in a flow with very extreme angle of attack. For this purpose the 2d-LCA is equipped with a cantilever of $140\mu\text{m}$ in length and a vane of $30\mu\text{m}$ in height. A standard x-wire with an angular acceptance range of $\pm 40^\circ$ is used as reference. In order to generate very large angle of attack within a turbulent domain, the anemometers were placed very close (8 cm) behind a thick cylinder of 4 cm in diameter. All key parameter of the setup are summarized in table 5.3.

| | |
|-----------------------|--|
| wind velocity | 12 m/s |
| cylinder dimensions | diameter: 4 cm length: 60 cm |
| 2d-LCA | Cantilever of $140\mu\text{m}$ in length with vane of $30\mu\text{m}$ in height |
| x-wire | type: Dantec 55p51 wire length: 1.25mm (sensitive) |
| sampling frequency | 60kHz (low-pass filter at 30kHz) |
| number of Data points | 8.000.000 (for each anemometer) |
| Reynolds number Re | 33.800 |

Table 5.3: Overview of the setup parameters.

The 2d-LCA has been calibrated for an angular range of $\pm 65^\circ$ and the x-wire for a range of $\pm 40^\circ$. The following analysis aims for revealing the differences in the statistics between both anemometers.

General data evaluation and one-point statistics

As the first step, the plot in fig. 5.19 shows the histograms of the time series of the angle of attack for the 2d-LCA (green) and the x-wire (red). The histogram from the 2d-LCA data shows a distribution up to angle of attack of around $\pm 62^\circ$ with a mean value of -0.08° . Very extreme angle of attack around $\pm 60^\circ$ show very little count numbers, but are still present. In the center and for angle of

attack between roughly $40^\circ - 50^\circ$ the distribution shows some irregularities. These are likely to be caused by dirt on the 2d-PSD or on the reflection pad of the cantilever (also see section 3). On the contrary, the x-wire is not capable of detecting angle of attack more extreme than $\pm 40^\circ$ due to the angular limits of the calibration plane. For angle slightly lower than $+40^\circ$ and slightly larger than -40° the histogram shows higher number counts. These rises exist because more extreme angle are projected into the inside of the calibration plane (see also section 4.4). The mean angle of attack measured by the x-wire is -0.41° .

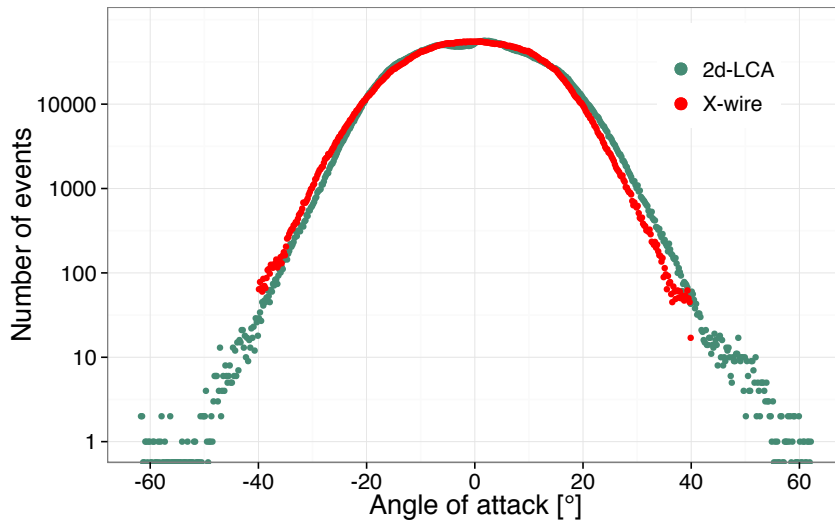


Figure 5.19: Histogram of the angle of attack for the 2d-LCA (green) and the x-wire (red).

In fig. 5.20 the spectral densities for the angle of attack are compared. The spectra were normalized by the absolute power and averaged by adding multiple spectra of shorter sections of 8×1024 samples.

Both spectra show comparable dynamic ranges and agree well up to frequencies of about 2kHz. Beyond that, the x-wire spectrum decays faster than the 2d-LCA. Moreover, both anemometers capture a peak at about 65Hz that corresponds to the detaching vortices induced by the cylinder ^a.

Next, in fig. 5.21 the spectral densities for the absolute value of velocity are considered. Here, both spectra are almost identical up to the point where the x-wire spectrum merges into noise (at about 8kHz). The spectrum of the 2d-LCA continues to decay for more than one decade.

^aThe detaching frequency f_d is estimated using the Strouhal number defined as $Sr = f_d d / u$, where d is a characteristic length (in this case d is the diameter of the cylinder).

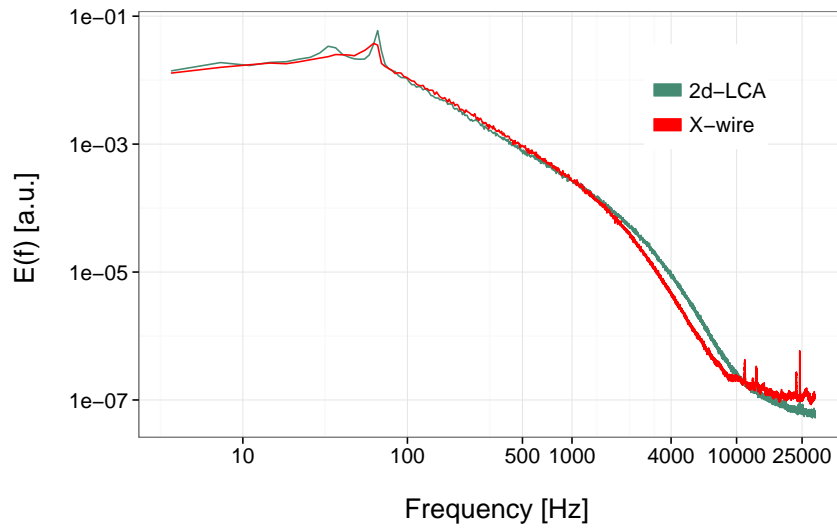


Figure 5.20: Spectral densities of the angle of attack for the 2d-LCA (green) and the x-wire (red).

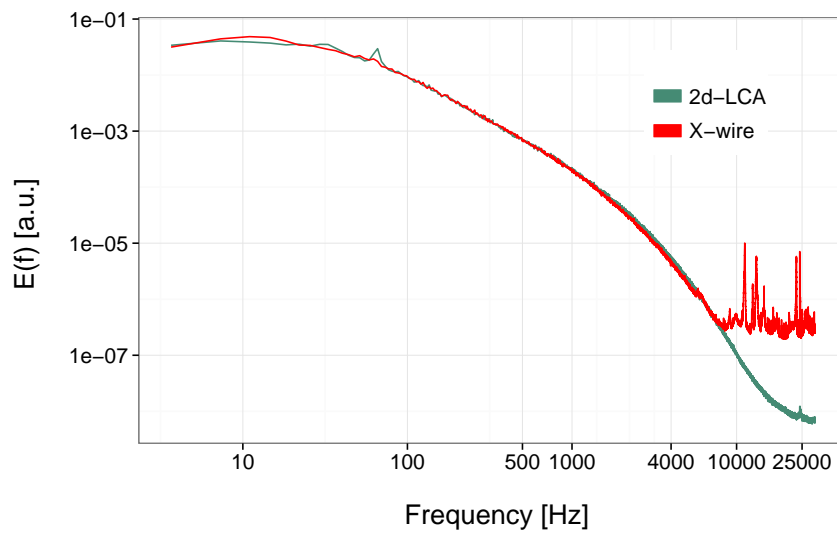


Figure 5.21: Spectral densities of the absolute value of velocity for the 2d-LCA (green) and the x-wire (red).

Two-point statistics

The next step is the evaluation of increment PDFs for the angle of attack, which are shown in fig. 5.22. The time intervals chosen are $\tau_1=0.167\text{ms}$, $\tau_2=0.333\text{ms}$,

$\tau_3=1\text{ms}$, $\tau_4=1.667\text{ms}$ and $\tau_5=16.667\text{ms}$ (from top to bottom). The solid lines represent fits in accordance with eqn. (1.18) (for distribution corresponding to $\tau_1 - \tau_4$) and a Gauss-fit (for the distribution corresponding to τ_5). It is striking that the tails of the distributions obtained from the x-wire are overestimated for τ_1 and τ_2 and underestimated for τ_3 and τ_4 . Only for the largest scale both anemometers agree. The same behavior is seen from the course of the form parameter, which is shown in fig. 5.23. Here, the graph corresponding to the x-wire starts at higher values and decays much faster than the 2d-LCA for small τ . For higher τ of about 10ms, both graphs join again.

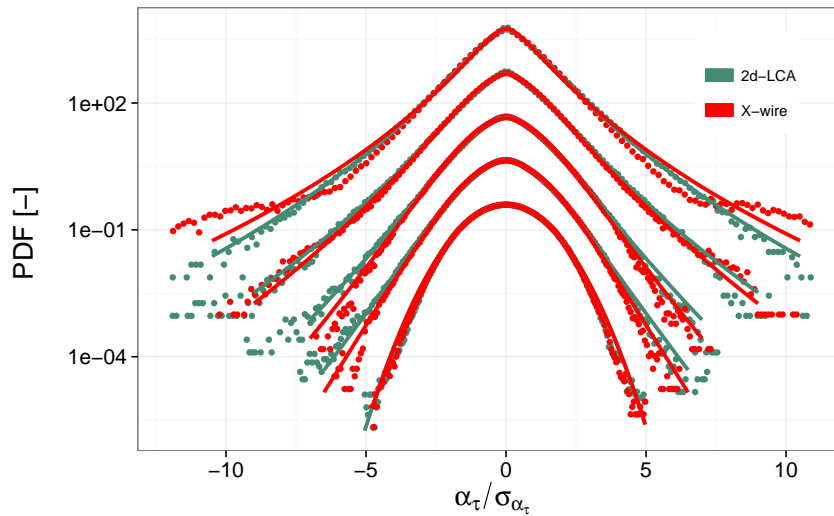


Figure 5.22: Increment PDFs for the angle of attack for the 2d-LCA (green) and the x-wire (red) with $\tau_1=0.167\text{ms}$, $\tau_2=0.333\text{ms}$, $\tau_3=1\text{ms}$, $\tau_4=1.667\text{ms}$ and $\tau_5=16.667\text{ms}$ (from top to bottom). Solid lines represent fits of the PDFs. The distributions corresponding to τ_{1-4} were fitted according to eqn. (1.18) and the distribution corresponding to τ_5 was fitted using a Gauss.

Lastly, fig. 5.24 shows the increment PDFs for the absolute value of velocity. Again, small deviations are present in the tail sections, although not as strongly pronounced as in the PDFs for increments of angle of attack.

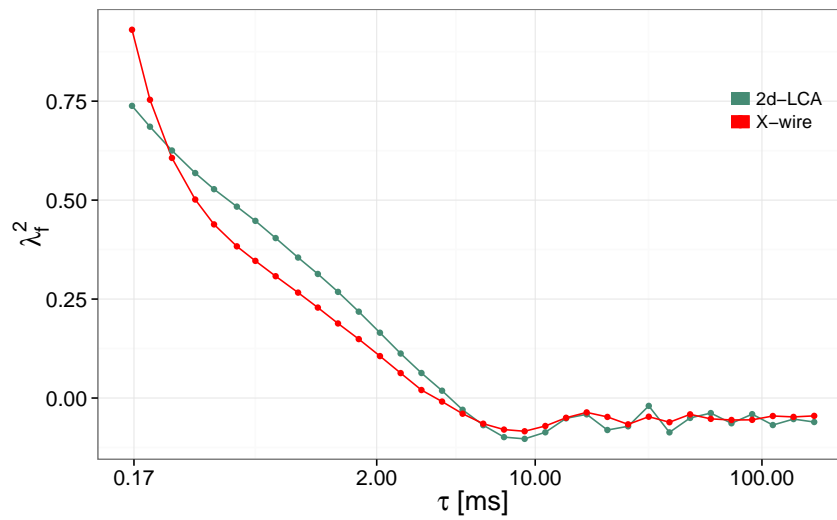


Figure 5.23: Course of the form parameter for the 2d-LCA (green) and a x-wire (red).

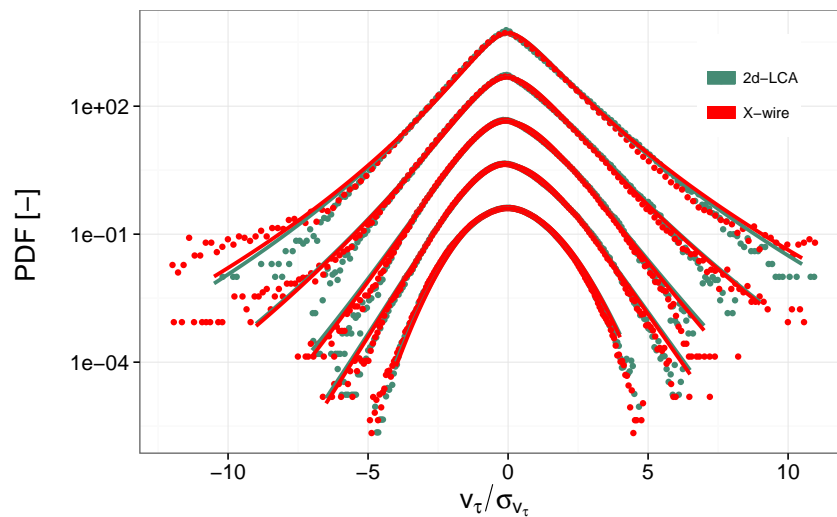


Figure 5.24: PDFs of increments for the absolute value of velocity for the 2d-LCA (green) and the x-wire (red) for $\tau_1=0.167$ ms, $\tau_2=0.333$ ms, $\tau_3=1$ ms, $\tau_4=1.667$ ms and $\tau_5=16.667$ ms (from top to bottom). Solid lines represent fits of the PDFs. The distributions corresponding to τ_{1-4} were fitted according to eqn. (1.18) and the distribution corresponding to τ_5 was fitted using a Gauss.

5.3 Measurements in the wake of a large grid

The measurements presented in this section were carried out in the ONERA S1 wind tunnel in Avrieux, France. The goal of the measurements was to investigate the small-scale structures in fully developed turbulent flow generated by means of a grid. The dimensions of the setup and the flow velocity have been adapted in such a way that Kolmogorov scales in the order of millimeters could be reached. In that case all scales within the flow would become detectable by standard hot wires. In the following, the data collected by the 2d-LCA will be compared with a single hot wire of type Dantec 55p11 with wire length of 1.25mm and another sensor prototype, which is not discussed further in the following. The table in 5.4 lists all important setup parameters. Two photographs

| | |
|--|---|
| wind velocity | 44.4m/s (near the grid) |
| grid dimensions | diameter: 10m bar width: 0.12m mesh width: 0.625m |
| 2d-LCA | Cantilever of 140 μ m in length with vane of 30 μ m in height sampling: 100kHz (low-pass filter at 50kHz) |
| x-wire | type: Dantec 55p11 wire length: 1.25mm (sensitive) sampling: 250kHz (low-pass filter at 100kHz) |
| sensor prototype | sensing length: 30 μ m sampling: 200kHz (low-pass filter at 100kHz) |
| number of Data points | 2d-LCA: 10 ⁶ x-wire: 25 ⁶ sensor prototype: 20 ⁶ |
| Taylor Reynolds number Re_λ | 800 |

Table 5.4: Overview of the setup parameters.

of the setup are shown in fig. 5.25. The anemometers discussed here were mounted (among others) in a distance of 15.36m away from the grid on a support structure that has been built for this purpose specifically. The hot wire data has been collected by staff members of LEGI (University of Grenoble, France). The measuring campaign took 5 days in total. During that time several interim

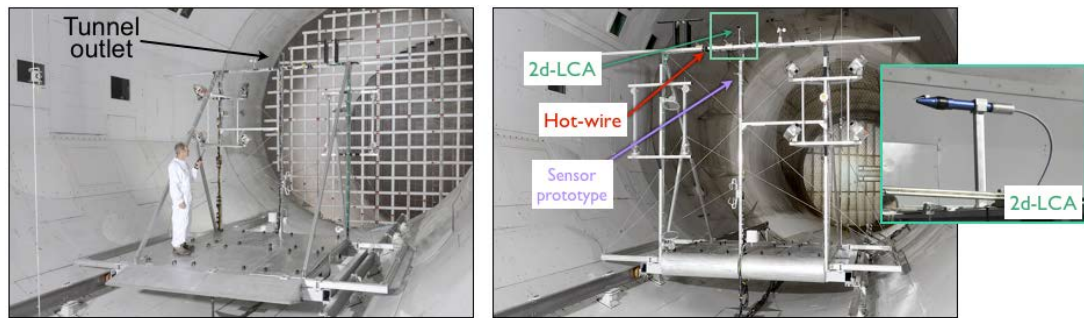


Figure 5.25: Measurement setup in the S1 wind tunnel at the ONERA facility. Several anemometers are mounted to a rack in a distance of 15.36m behind the grid. The positions of the 2d-LCA, the sensor prototype and the hot wire are highlighted. The magnified area shows the installation of the 2d-LCA.

calibrations of the hot wire and the sensor prototype were performed by means of the velocity measured behind the grid (based on pressure readings). For that purpose the wind tunnel velocity has been slowly increased from 0m/s to 44.4m/s and the resulting ramps have been used for calibration. Because of the turbulent inflow this method is rather imprecise and accompanied by uncertainties. The 2d-LCA has been calibrated using a mobile calibration unit as shown in fig 5.26 right after the measurement.

General data evaluation

The following data analysis is referred to the absolute value of the velocity only since the hot wire and the sensor prototype are one-dimensional anemometers. A first impression of the time series provided by all three anemometers is given in fig 5.27. The figure shows short sequences corresponding to 0.1ms for each anemometer. Immediately, one takes note of the fact that the time series collected by the sensor prototype is superimposed with heavy noise. The time series from the hot wire and the 2d-LCA appear to be similar at first sight. A comparison of energy spectra for the whole time series of all three anemometers is shown in fig. 5.28. As can be seen, the spectra of the hot wire and the sensor prototype have huge peaks in the high frequency region of above $\sim 7\text{kHz}$. A major amount of these peaks (in particular the sharp ones) is likely to be caused by electrical noise favored by the setup that comprises a lot of measuring systems and other equipment in a narrow space. The two peaks at $\sim 400\text{Hz}$ and $\sim 600\text{Hz}$ seen in the 2d-LCA spectrum are caused by detaching vortices from the mounting bracket and the cable, which have diameter of 2cm and 1.4cm,



Figure 5.26: 2d-LCA mounted to a mobile calibration unit during the measuring campaign at the ONERA S1 wind tunnel.

respectively. It is believed that these detaching vortices caused vibrations on the relatively long and thin 2d-LCA boom (see magnified area in fig. 5.25). For different velocities a change in frequency has been observed. A $-5/3$ decay (indicated by the black line) is found for the hot wire and the sensor prototype between about 50Hz-3kHz and for the 2d-LCA between about 200Hz-3kHz. Before continuing the analysis, the time series of the sensor prototype will be low-pass filtered at 50kHz by means of a butterworth filter of 8th order. A section of the filtered time series is shown in fig. 5.29.

The table in 5.5 compares the key parameter obtained from the data sets of all three anemometers. The mean values of the velocity agree well for all three anemometers. Larger differences occur for the maximum velocity between the sensor prototype and the other two anemometers. The values of the Taylor lengths were obtained using eqn. (1.26) and the Löfdahl-Aronson method that is explained in section 1.2.6. It should be noted that filtering in the high frequency area has an impact on the derivative in eqn. (1.26). Therefore, a value for the Taylor length from the NSTAP data set cannot be identified free of uncertainties. The values in brackets were determined from the positive curvature of the autocorrelation coefficient (see section 1.2.6). Both methods deliver comparable values for the data sets corresponding to the 2d-LCA and the sensor prototype. For the hot wire, only the Löfdahl-Aronson gives a Taylor length that agrees with the other anemometers. The second method based on the shape of the autocorrelation coefficient gives a much smaller value.

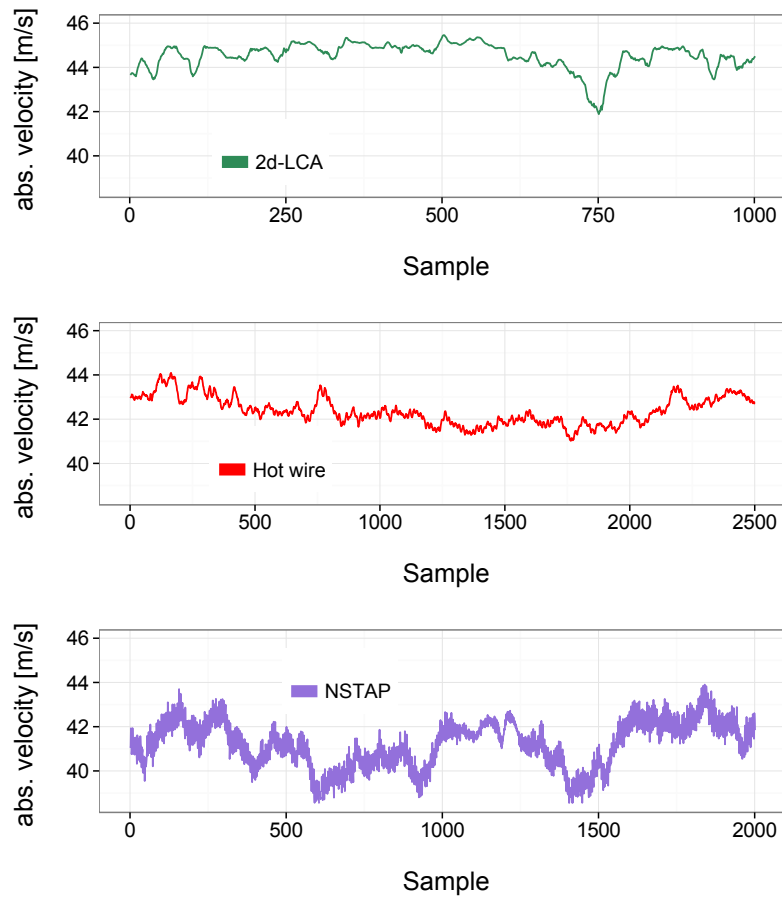


Figure 5.27: Time series for the absolute value of the velocity measured with the 2d-LCA (green), hot wire (red) and sensor prototype (purple). The time series correspond to 0.1ms for each anemometer.

The derivatives needed to calculate the Kolmogorov lengths were also determined using the Löfdahl-Aronson method. Kolmogorov scales ranging between 1.15mm (2d-LCA) and 1.21mm (hot-wire) were found. Therefore, the original goal of the experiment to create a flow with Kolmogorov lengths larger than the largest sensing element (hot wire length of 1.25mm) cannot be validated.

The turbulence intensities obtained from the data of the 2d-LCA and the hot wire are similar, whereas a larger value has been found for the sensor prototype. Moreover, deviations occur for the variances between all three anemometers. Fig. 5.30 shows the PDFs of increments for the absolute values of the velocity for $\tau_1=0.05\text{ms}$, $\tau_2=0.15\text{ms}$, $\tau_3=2\text{ms}$, $\tau_4=20\text{ms}$ and $\tau_5=0.1\text{s}$ (from top to

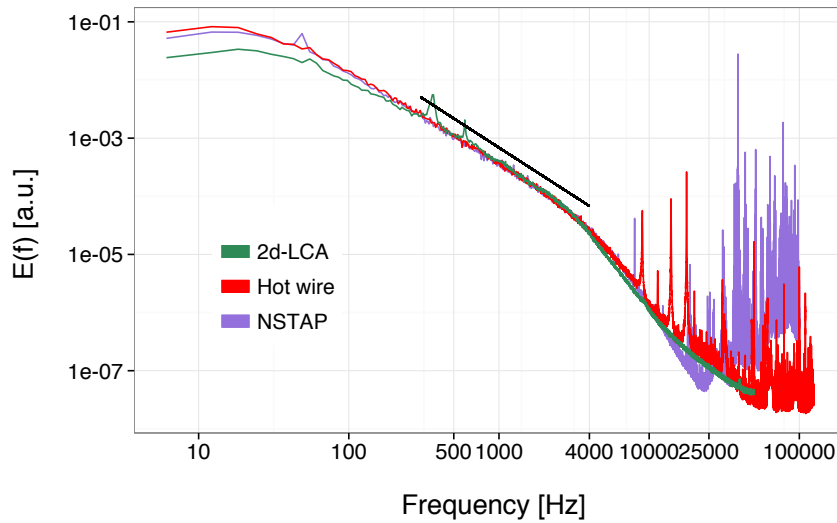


Figure 5.28: Energy spectra obtained from the 2d-LCA (green), hot wire (red) and sensor prototype (purple). The black line indicates a slope of $-5/3$.

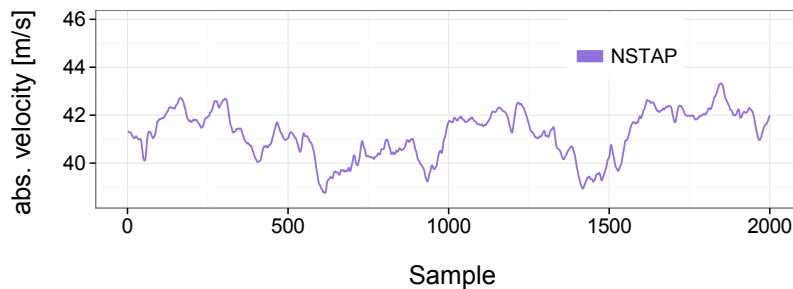


Figure 5.29: Section of filtered time series at 50kHz for the absolute value of the velocity measured with the sensor prototype. The time series corresponds to 0.1ms.

bottom). This corresponds to frequencies between 10Hz and 20kHz. One can see that the statistics of all anemometers agree best for smallest scales, i.e. τ_1 . It is striking that for larger τ the 2d-LCA PDFs are more intermittent. However, the analysis of the measurements presented in section 5.1 shows that the 2d-LCA does not systematically show this behavior. Further deviations also exist between the sensor prototype probe and the hot wire, especially for small τ . One possible reason for the extreme intermittent statistics of the 2d-LCA on

| Parameter | 2d-LCA with vane | sensor proto-type | hot wire |
|-----------------------------------|------------------|-------------------|---------------|
| mean velocity [m/s] | 44.22 | 42.11 | 42.84 |
| min. / max. velocity [m/s] | 38.12 / 46.14 | 40.65 / 51.40 | 40.06 / 46.25 |
| integral length L [mm] | 90.3 | 104.5 | 87.6 |
| Taylor length λ [mm] | 10.84 (11.27) | 12.55 (11.52) | 9.80 (6.11) |
| Kolmogorov length η [mm] | 1.15 | 0.98 | 1.21 |
| turbulence intensity TI [%] | 2.29 | 3.46 | 1.94 |
| variance σ^2 [m^2/s^2] | 1.02 | 2.51 | 0.68 |

Table 5.5: Key parameters of the flow measured with the 2d-LCA, the sensor prototype and a hot-wire.

larger scales might be a coarse calibration (interval steps of 15° and 5m/s) that has been performed using the mobile calibration unit on-site. Originally, this coarse calibration was meant for validation purposes of a much finer calibration that has been carried out before, however, the first calibration became useless after dirt particle hit the cantilever. For this reason the coarse calibration has been used in order to allocate the measured data.

The fact that a lot of dust particles and pollen were carried by the flow also had an impact on the other anemometers. The reason for this polluted air is the fact that the ONERA S1 wind tunnel sucks in air from the outside without any filtering. Consequently, many hot wires broke during the measurement campaign or delivered a corrupt signal due to dust collisions. With regards to the 2d-LCA this means that the window (see fig. 2.3) has been potentially polluted too, thus resulting in another source of uncertainty.

On the whole, one can say that the results with its discrepancies presented in this section clearly emphasize the importance of promoting the development of measurement techniques.

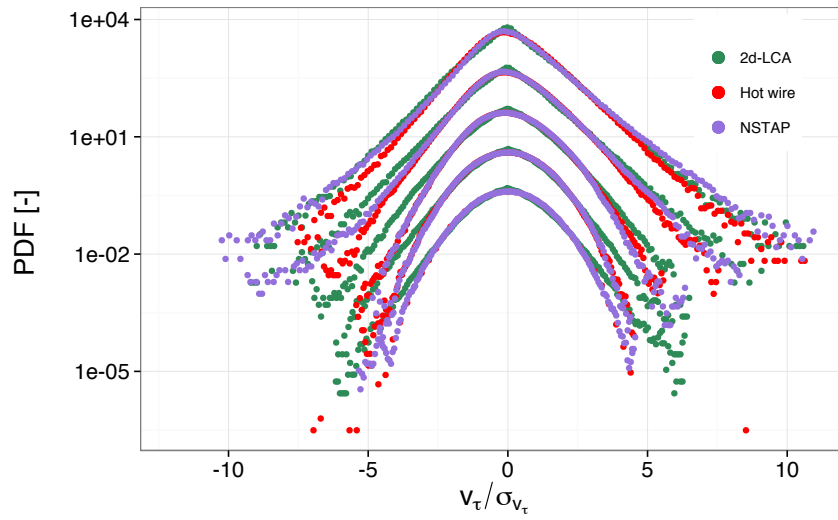


Figure 5.30: PDFs of increments for the absolute value of the velocity for the 2d-LCA (green), the hot wire (red) and the sensor prototype (purple) for $\tau_1=0.05\text{ms}$, $\tau_2=0.15\text{ms}$, $\tau_3=2\text{ms}$, $\tau_4=20\text{ms}$ and $\tau_5=0.1\text{s}$ (from top to bottom).

Chapter 6

Outlook and Summary

The objective of the work presented here is the continuation of the development of the 2d-LCA. Before this work the 2d-LCA suffered from low stability, insufficient user friendliness, noise sensitivity (electronics) and a weak angular resolution. Several efforts have been given in order address these issues.

The first step was a redesign of the 2d-LCA body. In the course of this, several components were replaced or optimized with the goal to improve the manageability, especially with regard to the alignment of the cantilever. The actions described in section 2.3 have led to a significant simplification of the initialization procedure (see appendix C), thus making the anemometer accessible to inexperienced persons. Furthermore, the redesign improved the stability of the 2d-LCA. The tests from section 4.5 confirm that the stability of the 2d-LCA is comparable to commercial x-wires.

One focus of this work was the development of a new electrical circuit for the computation of the 2d-PSD signals. The new circuit design is presented in appendix H. It features low-noise operational amplifiers with very short slew rates that ensure a fast response of the anemometer up to about 140kHz. In addition, an external and portable signal-conditioning unit has been created. A comparison between the new electronics and the older design show an improvement with regard to noise level and dynamic.

Certainly the most valuable achievement of this work is the introduction of a new series of vane-equipped cantilevers (see section 3) that were proven to significantly increase the range of accepted angle of attack. A comparison of calibration planes obtained using the old cantilever and the new design with vane clearly verify that the range of acceptance angle has increased from $\pm 50^\circ$ to $\pm 90^\circ$ (see section 4.1). This is a unique characteristic among high-resolution anemometers.

The performance of the improved 2d-LCA has been demonstrated by means of three different measurements. These include measurements of wake flows

generated by two different cylinders and a huge grid. Commercial x-wires, a hot wire and a non-commercial micro-structured hot-wire (NSTAP) served as reference sensors. The statistics of all data sets collected were compared and confirmed the applicability of the 2d-LCA.

The tests made so far have identified even more potential for further improvements. In this context, two aspects are particularly considerable. First, as shown in fig. 4.7 the cantilever with vane achieves a great angular resolution in regions of extreme angle of attack. This resolution is significantly larger than in the vicinity of the centerline of 0° . In order to exploit this feature, one might argue to simply change the alignment of the whole anemometer with regard to the flow, however, turning the anemometer away from the flow would lead to unequal angular ranges and resolution powers between positive and negative angle of attack.

The second aspect concerns the flow around the vane for small angle of attack. It has been found that for small angle of roughly $<5^\circ$ the existence of the vane does not improve the twisting significantly. This is due to the small additional area of attack provided by the vane. In fact, the larger standard deviations observed in fig. 4.5 along the 0° direction together with the discrepancies in the same area presented in fig. 4.10 give reason to believe that the vane destabilizes the flow for small inflow angle and causes disturbances of the deflection.

The two aspects named above motivate for a further optimization of the cantilever design. One design idea, which could suppress the high standard deviation around the centerline of 0° and increase the resolution power in that area is a cantilever with a “v”-shaped or “hat”-shaped vane as shown in fig. 6.1. Both types of vanes provide the same additional area of attack. It is believed that these designs would preserve the extended angular range and at the same time ensure a stationary flow around the cantilever for straight and nearly straight inflow. The non-stationarity (that is indicated by a higher standard deviation around 0°) of the cantilever with current design is caused by the vane that is constantly trying to reach a stable position by means of bending. This situation can be compared with an attempt to blow against the edge of a piece of paper without folding it. It is reasonable to believe that the two inclined faces of the new types of vanes could minimize this effect.

The graphs in fig. 6.2 show the areas of the “v”-shaped or “hat”-shaped vanes that are facing the flow for different angle of attack between 0° and 90° in comparison to the current design. The blue graph corresponds to the simple vane as used until now. It basically shows the sine-projection, which reaches its maximum at 90° . The red and green graphs represent “v”- or “hat”-shaped vanes with angle of 15° and 45° between both wings, respectively.

Although this graph does not take any aerodynamic effects into account, it can be used to roughly relate the forces acting on the different types of vanes to each other. The steeper slopes for small inflow angle of the suggested vanes give reason to believe that the weak resolution power in this area can be increased in comparison to the current design. However, this is only possible at the expense

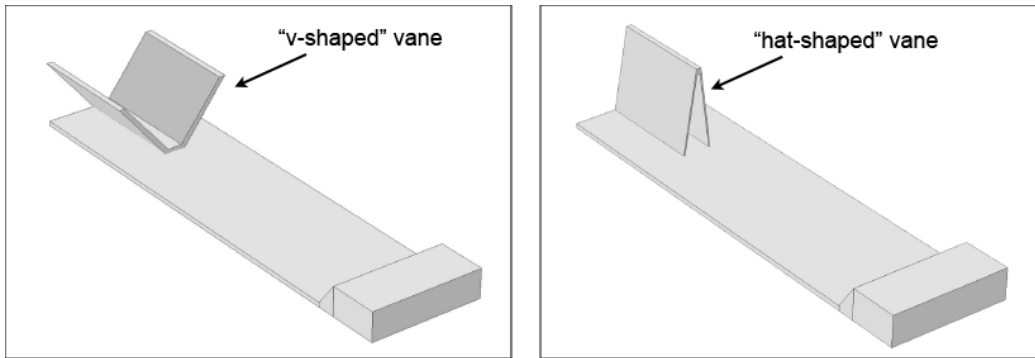


Figure 6.1: New design of a cantilevers with “v”-shaped and “hat”-shaped vanes.

of the resolution power for large angle of attack.

Recently, an application for a patent for these new designs has been filed (file number: 102015000064.0).

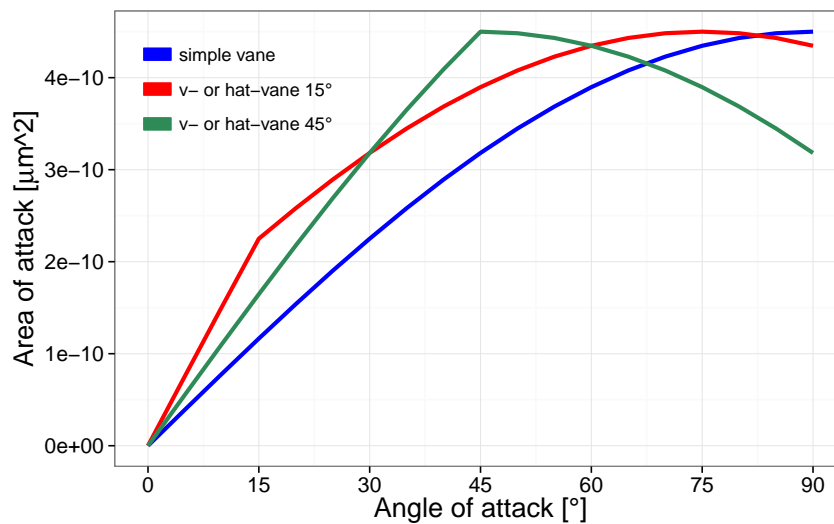


Figure 6.2: Area of attack provided by a simple vane (blue), “v”- or “hat”-shaped vane with 15° between both sides (red) and 45° between both sides (green).

In future CFD-tools including fluid-structure interaction (FSI) could be used to further investigate the properties of these or similar cantilever designs.

Appendix A

Influence of the anemometer housing upon the flow

The front section of the housing of the 2d-LCA has been designed in such a way that distortion due to passing flow is eliminated and blockage is reduced. However, this design has been developed for a 1d-LCA originally. In order to assess it for oblique flows in the range of $\pm 90^\circ$, hot-wire measurements have been carried out. Although, it might be assumed that stationary effects caused by the sensor become non-relevant after calibration, an additional risk of formation of non-stationary effects like turbulent backflow exists. These effects will likely have an impact on the measured data and thus need to be excluded or at least revealed.

Possible non-stationary effects have been identified using x-wire measurements in a rather unusual approach. For that, an x-wire has been built into a 2d-LCA housing with its wires placed at the position of the cantilever (about 1cm from the edge of the sensor). Next, a calibration for angle of attack of $\pm 90^\circ$ has been performed. This approach aims for comparing the calibration obtained that way with a calibration by a standard x-wire. In particular, the standard deviation for each calibration point, which is attributed to non-stationary effects is of interest. The calibrations have been carried out for a velocity range of 4-13m/s in intervals of 1m/s and inflow angle in the range of $\pm 90^\circ$ in intervals of 5° . Although, this angular range exceeds the application range of the x-wire by far (see section 4.4), the measured values are still useful for comparison. The calibrations with housing and without are shown in fig. A.1 together with its standard deviations for each point.

The result of this rather indirect test shows, that both calibrations agree very well in terms of shape and in terms of standard deviation. Consequently, this analysis claims that the design of the sensor housing is suitable for operation in two dimensions at least up to inflow angle of $\pm 90^\circ$.

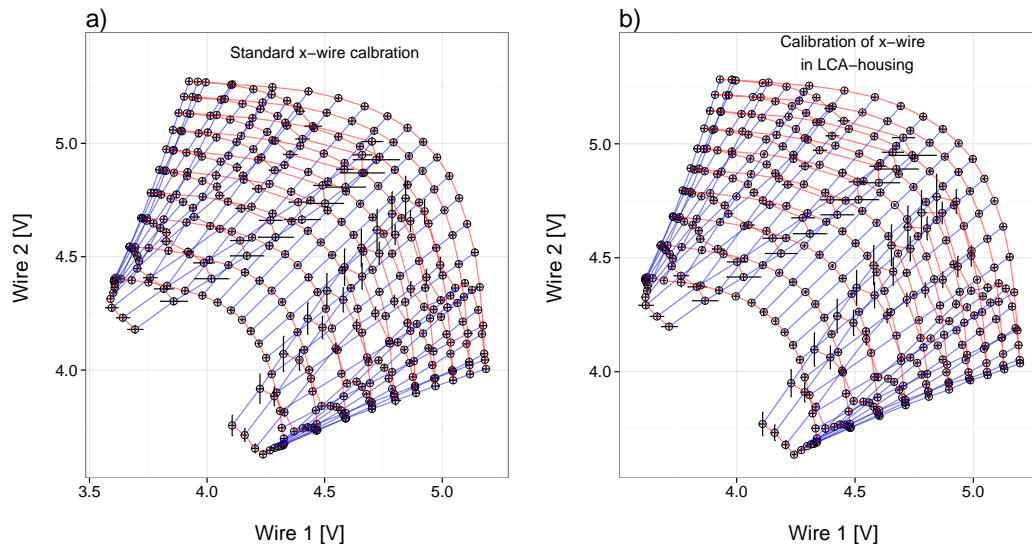


Figure A.1: Standard x-wire calibration (a) for 4-12m/s and inflow angle of $\pm 90^\circ$ and a calibration obtained from the same x-wire built into a LCA-housing (b). Black error bars indicate the standard deviations for each calibration points.

Appendix B

Labview program for automated calibration

As mentioned in section 4 the calibration process has been completely automated using several hardware components and a LabVIEW program.

The LabVIEW interface (see fig. B.1) features several setting possibilities for adjusting the accuracy and the range of the calibration. In addition, it allows for calibrating more than one sensor at the same time. The number of sensors is limited by the number of channels of the A/D-converter that is used for data acquisition.

The most relevant parts of the interface shown in fig. B.1 are pooled in sections (highlighted in red). In section A the ranges for the angle of attack and the inflow velocities together with the interval steps are specified. In the exhibited configuration an angular range of -35° - $+35^{\circ}$ and a flow velocity range of 8-18m/s have been chosen. The interval steps are 5° and 1m/s for the inflow angle and the velocity, respectively. Once executed, the program sets the flow velocity of the wind tunnel to the specified initial value and begins to pass through the angular range in intervals of the preassigned steps starting at highest negative angle of attack. The mean values of the output signals of the sensor(s) are recorded in a plain text file for each position. After covering the whole angular range, the flow velocity is increased by the given velocity step and the procedure is repeated until the whole calibration plane is generated. The amount of data points to be sampled can be defined. Furthermore, a plot in section B displays the recorded signals that are used to calculate the mean values. Optionally, this time series can be recorded as well. Finally, in section C the recorded calibration planes for the sensor(s) are plotted. All remaining setting and display elements are used for further configuration of hardware or monitoring purposes.

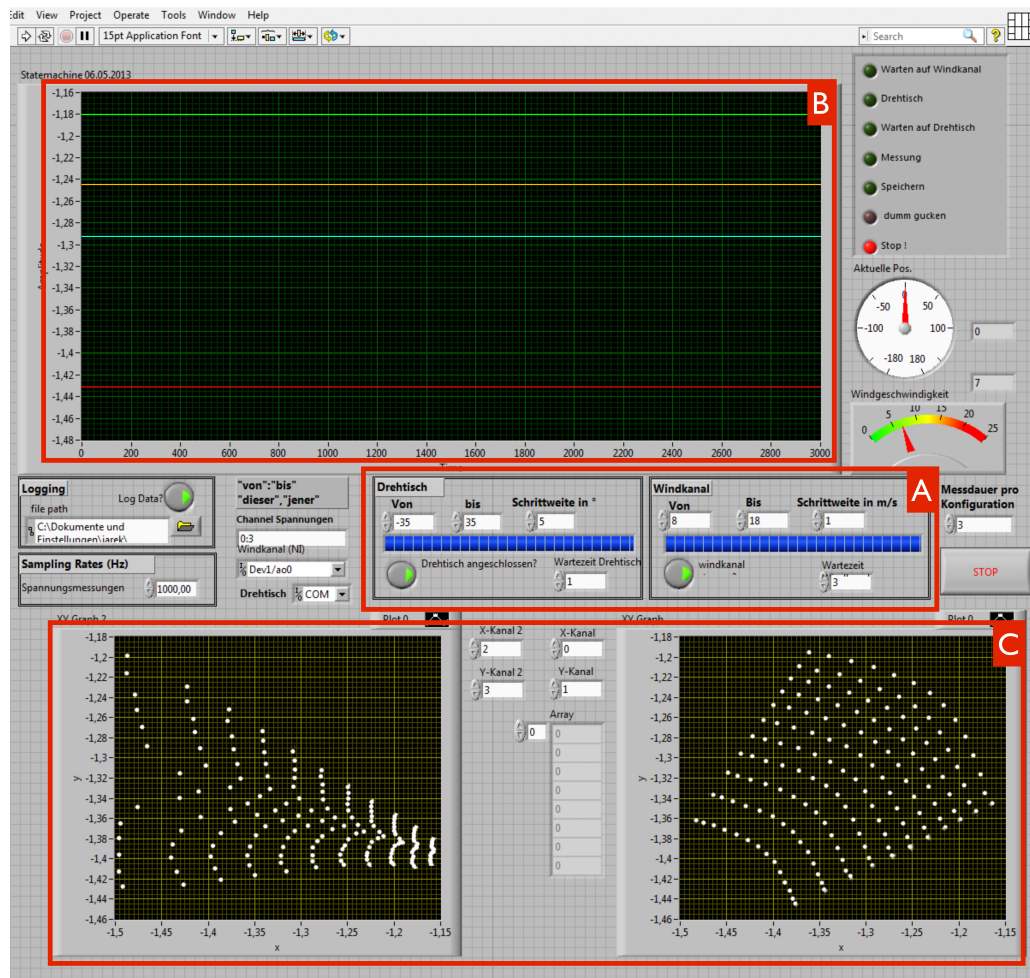


Figure B.1: Screenshot of the LabVIEW user interface for performing automated calibrations.

Appendix C

Adjusting of the Laser

C.1 Alignment of the laser

As in the case of any other anemometers, the 2d-LCA needs to be set up appropriately before operation. This chapter addresses the preparation procedure that involves the alignment of the cantilever and the reflecting spot along the 2d-PSD.

A precise positioning of the laser on the cantilever surface is of great importance for the performance of the anemometer. Since the greatest amount of deflection for a one-side clamped cantilever occurs at the tip, the best dynamic response is achieved if the laser is positioned as close as possible to the edge. However, it must be ensured that the center of the spot and thus the maximum light intensity remains on the cantilever surface. A tracking of the laser along the cantilever by naked eye is virtually impossible because of the tiny dimensions. Even under a microscope it is only possible after attenuating the laser light by means of appropriate natural density filters. Otherwise, the center of the laser spot is hardly recognizable. All in all, this approach is rather circumstantial. Instead, a different method has established that uses the diffraction pattern that is present in the forward-scattered light when pointing onto any part (cantilever or supporting structure) of the chip. This pattern is clearly visible when projected on a wall in a distance of about one meter.

The orientation of the pattern gives information about the location of the laser beam. Different orientations corresponding to distinctive positions are illustrated in fig. C.1(a-d). Thus, by observing the diffraction pattern it is straightforward to locate the cantilever. Once this is accomplished, the tip of the cantilever has to be approached. This is done by moving the laser along the long side of the cantilever down to the position where the pattern begins to weaken. At this position the laser beam leaves the tip of the cantilever. Thus, the op-

timal position is right before the weakening is noticeable. The position of the

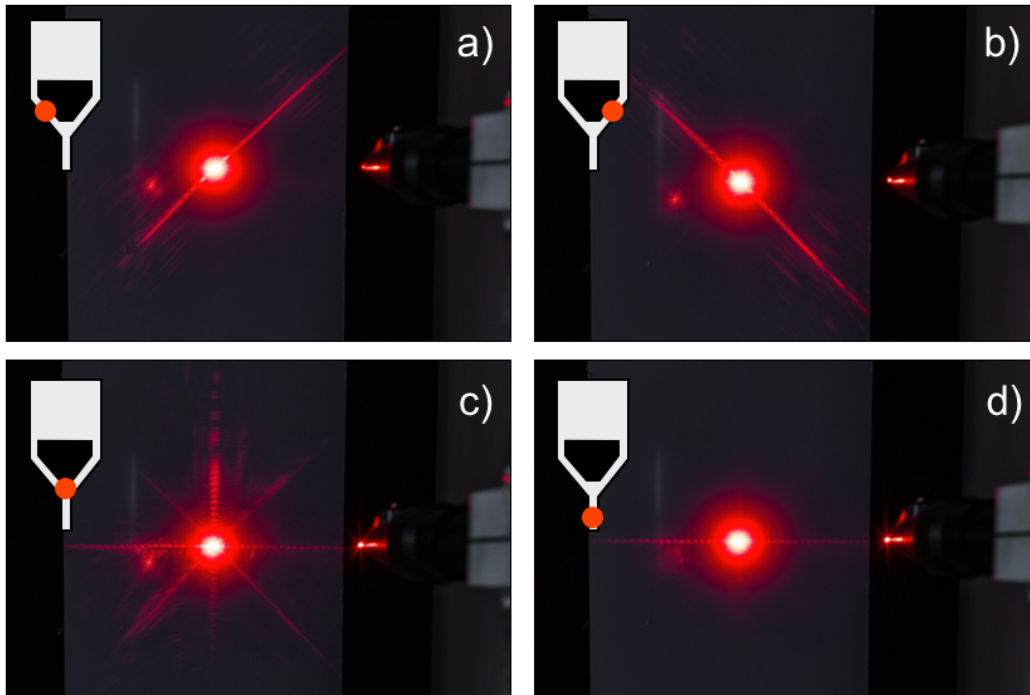


Figure C.1: Diffraction patterns in the forward scattered light for different positions of the laser along the chip. The positions indicated are from the perspective of the laser beam.

reflecting spot needs to be verified and if necessary corrected by means of the positioning options provided by parts #9 and #10 (see fig. 2.6). When using part #9, the laser position must be readjusted as well.

Appendix D

Characteristics of 2d-PSDs

D.1 Functionality of a 2d-PSD

In the following the functionality and basic characteristics of the 2d-PSD used for the 2d-LCA of third kind are discussed.

Today's state of the art PSDs made for visible light consist of resistive layers of p- and n-type silicon, forming a pn-junction. Incident light induces a photocurrent within the depletion zone, which is proportional to the light energy. The photocurrent passes through the p-type region to two or more electrodes and through the n-type region to one common electrode. In the case of a two-dimensional lateral effect PSD, i.e. a PSD with only one continuous active area, a resistive layer of p-type silicon serves as a current divider for four electrodes. In the course of this, the current is divided between the four electrodes proportional to the position of the incident light spot. The electrode that is placed closest to the light spot receives the most induced photocurrent.

Another familiar type of two-dimensional PSD-devices is the so-called quadrant-PSD. These PSDs consist of four subdivided active areas (segments) separated by a small gap of typically $1\text{-}2\mu\text{m}$ with one electrode per segment and one common anode. For proper operation, the light spot to be tracked must partially cover all four segments. Its position is determined by comparing the photocurrents induced in each segment. The largest deflection distance of a moving light spot that can be measured is limited to the size of the spot itself. Thus, defocusing can increase the measuring range, however at the expense of a weaker resolution power.

During experiments with various types of PSD-devices it has been found that a lateral effect two-dimensional pin-cushion PSD of type Hamamatsu S5990-01 with an active area of $4\text{mm} \times 4\text{mm}$ performs best for the 2d-LCA in terms of signal quality and manageability. The term "pin-cushion" is referred to PSDs

with improved electrode designs and a more sensitive active area that results in better linearity [28]. The light spot position can be tracked over the whole active area. However, if a part of the spot leaves this area, a shift in center of gravity of the light towards the center of the sensor will occur. This effect leads to incorrect position information.

Quadrant PSDs were also tested in the 2d-LCA, but proved rather ineffective for the operation as its linear behavior strongly depends on the light spot profile, which is not uniform due to the light interference pattern and residues from the production process on the surface of the reflective pad (see section 3). Consequently, the non-uniform spot would cause jumps in the position signal while moving along the segments. Thus, quadrant PSDs are more suited for centering purposes than for linear position tracking [26].

D.2 Position resolution of the 2d-PSD

The position resolution of any 2d-PSD is defined as the smallest detectable displacement distance of the light spot [27]. This distance is directly related to the smallest detectable change in current, which is depended on the signal to noise ratio (SNR) of the PSD. According to [28] the resolution of a lateral effect PSD is given by:

$$resolution = L \frac{I_n}{I_{ph}}, \quad (D.1)$$

with the induced photocurrent I_{ph} ^a, the total noise current I_n and the edge length L of the active area of the PSD. I_n can be expressed as:

$$I_n = \sqrt{I_{shot}^2 + I_{thermal}^2 + I_{en}^2}. \quad (D.2)$$

Here, I_{shot} and $I_{thermal}$ are shot and thermal noises produced by the 2d-PSD and are given by:

$$I_{shot} = \sqrt{2qBwd(I_{ph} + I_{dark})} + I_{en}^2 \quad (D.3)$$

^aThe photocurrent depends on the wavelength (photosensitivity of the PSD) and laser power. In the case of the 2d-PSD that operates in the 2d-LCA of third kind a photocurrent of about $22\mu A$ is estimated.

$$I_{thermal} = \sqrt{\frac{80k_b Bwd}{R_{ie}}}, \quad (D.4)$$

with the elementary charge q , the bandwidth Bwd , the dark current of the 2d-PSD I_{dark} and its inter-electrode resistance R_{ie} . I_{en} is an additional noise term associated with the op-amp used in the transimpedance connection for operating the 2d-PSD. I_{en} is determined by:

$$I_{en} = \frac{en}{R_{ie}} \sqrt{Bwd}, \quad (D.5)$$

with the input voltage noise en . For the configuration used in the 2d-LCA, a displacement resolution of about $0.3\mu\text{m}$ is achieved.

D.3 Response speed

The temporal resolution of each 2d-LCA component is of great importance and needs to be investigated carefully. As has been shown in section 3.1, the temporal resolution of the cantilever is in the range of 45-100kHz (depending on the kind of cantilever). In order to maintain the upper value as the temporal resolution of the whole anemometer, it must be ensured that no other component operates slower than this. Therefore, there is a need to determine the temporal resolution of the 2d-PSD.

The response speeds for PSDs are usually found in the datasheets. However, the values strongly depend on the wiring setup. For wavelengths of $\lambda_{laser} > 900\text{nm}$ the response speed also depends on λ_{laser} and is slightly diminished towards higher wavelength^b.

For the 2d-PSD used here, a rise time, i.e. the time needed for the output signal to rise from 10%-90% of its peak value, is $1\mu\text{s}$ [28]. This value was obtained for a near-infrared illumination of $\lambda_{laser} = 900\text{nm}$ with a forward bias of +5V at the cathode and a load resistance of $1\text{k}\Omega$. Although these conditions do not reflect the configuration used for the 2d-LCA, this value can be taken as a reference point. The tendency of the real rise time should go to even smaller values as a higher forward bias of +9V and comparable load resistances are used.

^bSilicon becomes more transparent towards a wavelength of $1.13\mu\text{m}$. Thus, light can penetrate deeper into the active material and induce electrons in the n-type layer. These electrons take longer time to drain off the electrodes.

Appendix E

Experimental setup for the estimation of Q-factors and resonance frequencies

In section 3.2 experimental results for Q-factors and resonance frequencies of two cantilevers of $140\mu\text{m}$ in length with vane and without vane are presented. In the following, the setup of the experiment will be explained in more detail. In order to drive the cantilevers electrostatically, the chips were prepared and terminated accordingly. In the course of this, the cantilever and a silicon block that was brought very close to the cantilever ($\approx 39\mu\text{m}$) served as the electrodes. Both components were coated with gold ($\approx 100\text{nm}$) to ensure good conductivity and were terminated using thin stranded wires. The wires were glued to the cantilevers using a conductive adhesive. The prepared cantilevers are shown in fig. E.1. The alternating current for driving the cantilevers was applied between A and B for the upper cantilever and between A and C for the lower cantilever. In the next step, the prepared cantilevers were fixed to a copper stage and put headlong inside a specifically designed vacuum chamber (fig. E.2). The connections A,B and C from figure E.1 were routed to the outside and connected to the signal generator (spectrum analyzer of type Agilent E4402B). The height of the stage has been adjusted in such a way that the distance between the cantilever surface and the bottom window of the chamber reached a minimal distance. This short distance made it possible to focus a laser beam (by means of a microscope objective) through the bottom window onto the cantilever surfaces. Fig. E.3 shows the extremely small laser spot in proportion to the cantilever. The position of the laser focus along the cantilever surface was adjusted using a traverse that positioned the whole chamber in two directions. The laser light that bounced off the (excited) cantilever and some other stationary parts (like the foundation of the setup or the window of the chamber) was collected by a

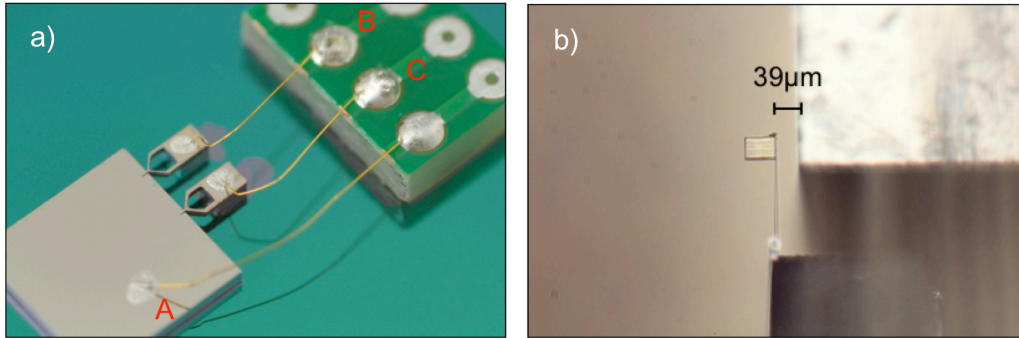


Figure E.1: Two cantilever chips prepared and terminated for electrostatic excitation (a) and side view of the cantilever above the silicon block (b). The alternating current for driving the cantilevers is applied between A and B (upper cantilever) or A and C (lower cantilever).

photodiode. The interference of the stationary laser beam and the moving beam led to light intensity variations that were associated with the excitation of the cantilever.

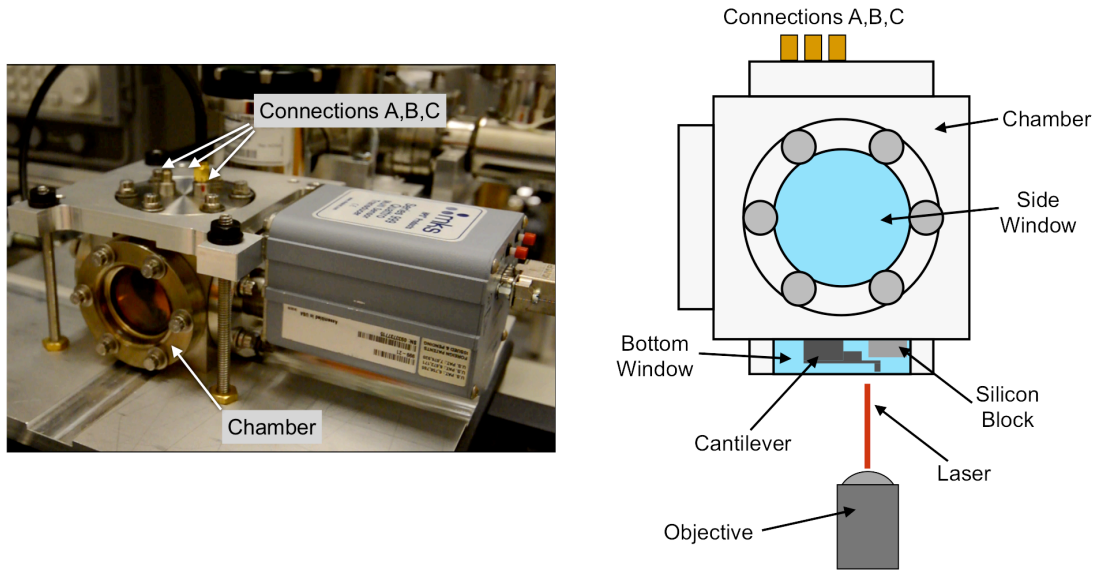


Figure E.2: Photograph of the vacuum chamber and schematic illustration of the setup.

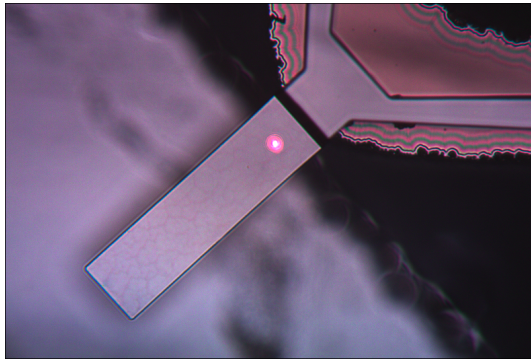


Figure E.3: Size of the laser spot in proportion to the cantilever.

Appendix F

Allocation of measured data

The basic procedure of applying the calibration to measured data is adopted from [34]. At the very beginning, two individual data sets are created from the calibration as recorded according to the procedure explained in 4. By doing so, the information regarding angle of attack and velocities are separated. Thus, each data set contains either velocity or angular information together with the x/y-coordinates of the reflected spot along the 2d-PSD. Plotting these two data sets yields the 3d-scatter plots as shown in fig. F.1 a) and b). Next,

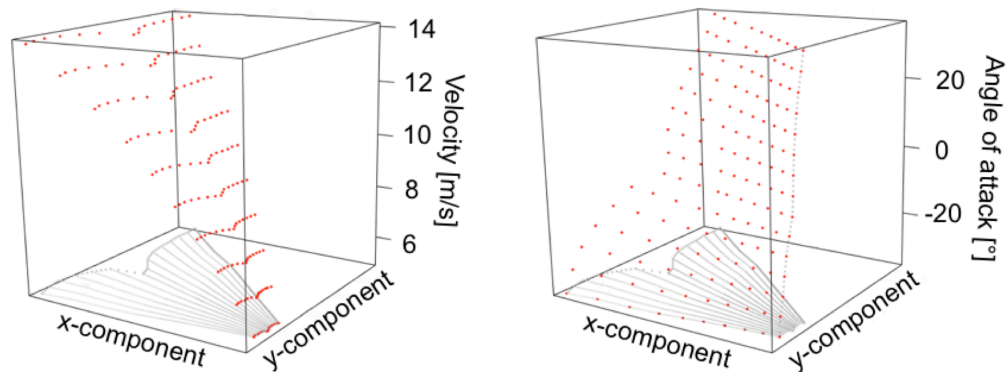


Figure F.1: Calibration points plotted against velocity (a) and angle of attack (b).

additional points are generated between the calibrated values using 3d-Akima splines (piecewise 3rd-order polynomials). That way a dense grid as illustrated in fig. F.2 is created.

The actual allocation of raw data-points (points within the x/y-plane) is done by determining the corresponding z-values, i.e. values for velocities or inflow angle. This is done by applying a prediction algorithm that searches for the best

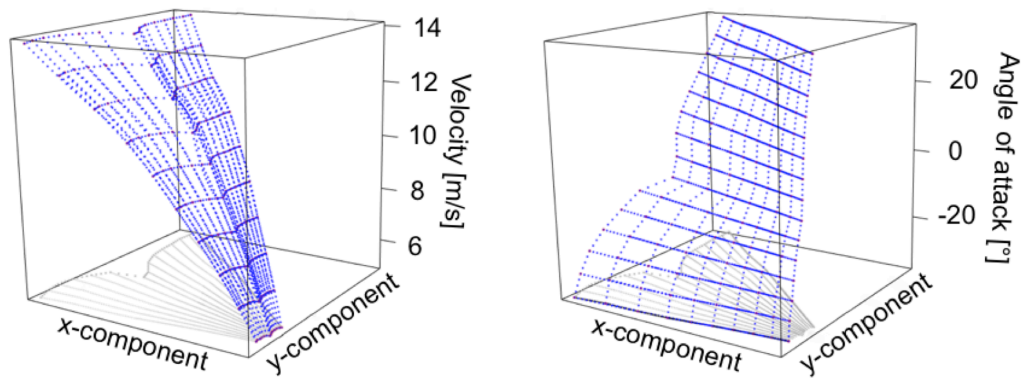


Figure F.2: Interpolated points (blue) using Akima-splines for the data sets representing velocities (a) and angle of attack (b).

value based on the available points.

Lastly, the longitudinal and transverse velocity components are obtained from the velocities and angle of attack.

Appendix G

Lead and connector pin assignment

Table G.1 shows the lead and connector pin assignment of the data cable used for the 2d-LCA. The cable is equipped with a circular push-pull connector of type Fischer S-103-A062-130, which is connected to the anemometer and a D-Sub 15 plug for connection to the external unit.

| Push-pull connector / pin | color of lead | D-Sub 15 plug / pin | Purpose |
|---------------------------|---------------|---------------------|------------------------------------|
| 4 | red | 7 | power supply +V |
| 5 | white | 13 | DC-motor (horizontal direction) |
| 6 | orange | 6 | DC-motor (vertical direction) |
| 7 | cable shield | 7 | ground |
| 10 | black | 12 | signal (x-component) |
| 11 | blue | 11 | power supply -V |
| 12 | green | 15 | signal (y-component) |

Table G.1: Pin assignment for the data cable of the 2d-LCA.

Appendix H

Circuit diagrams

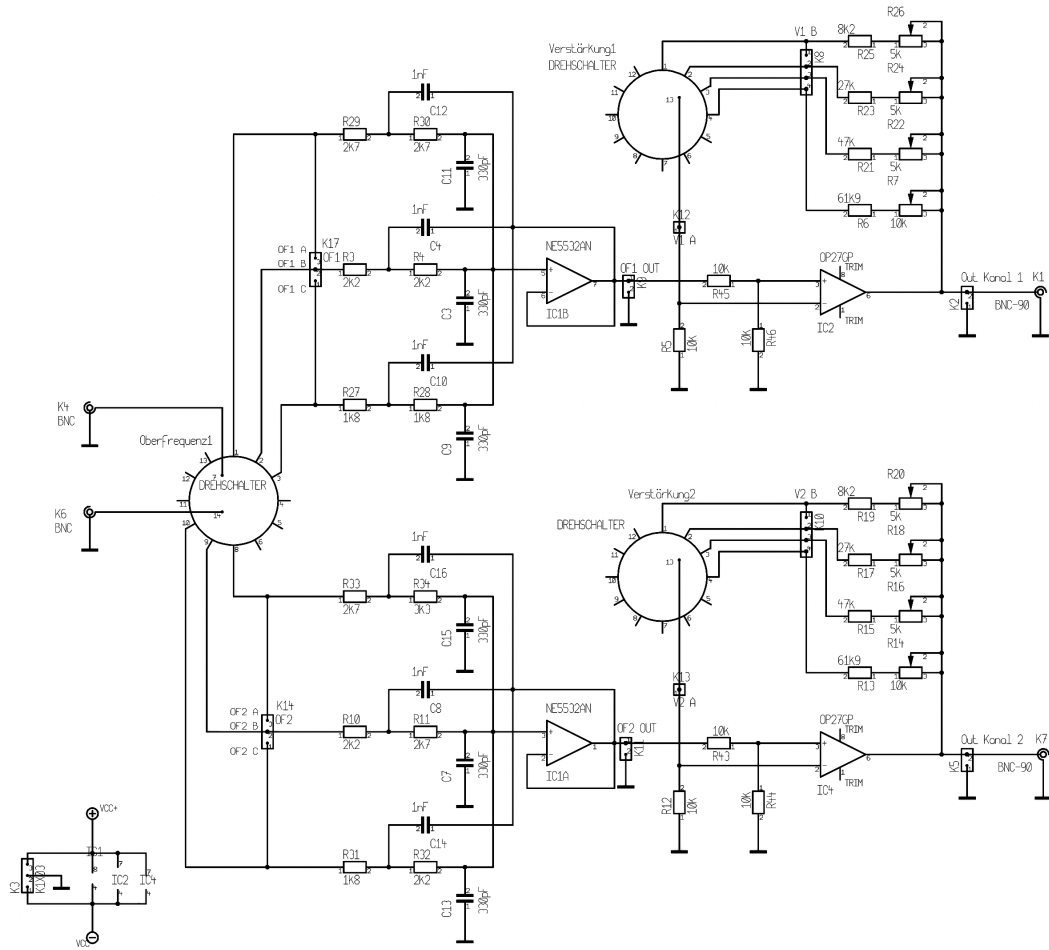


Figure H.2: Main circuit diagram for the amplification and filter section of the central unit.

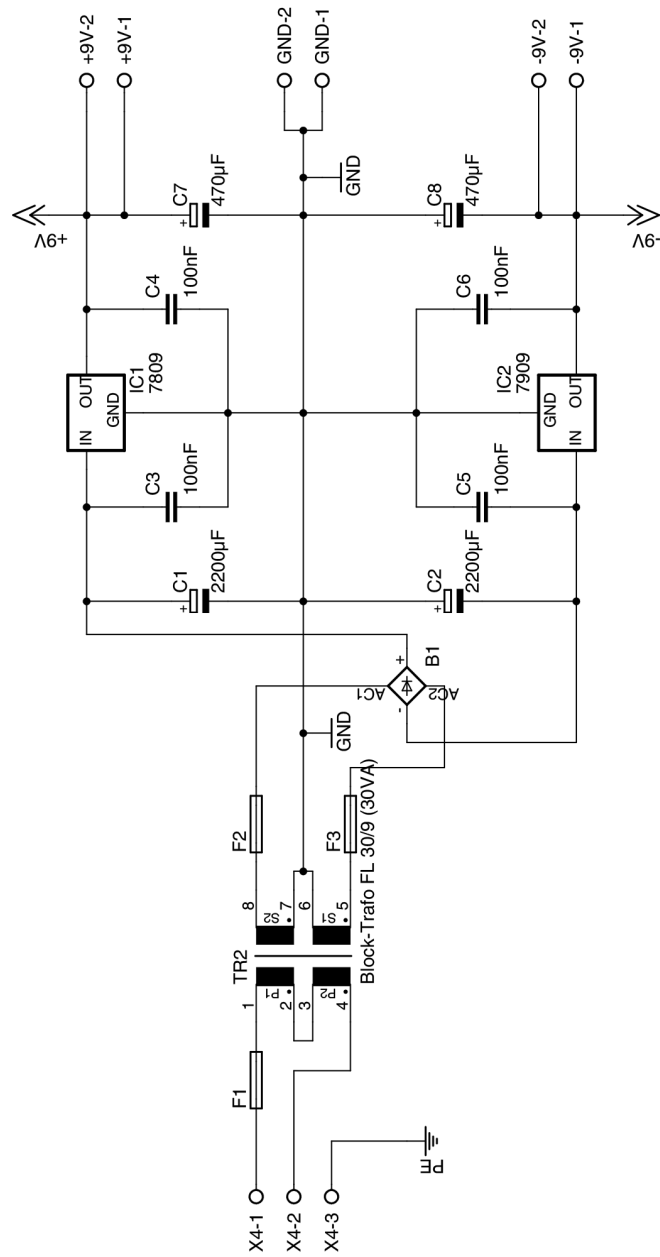
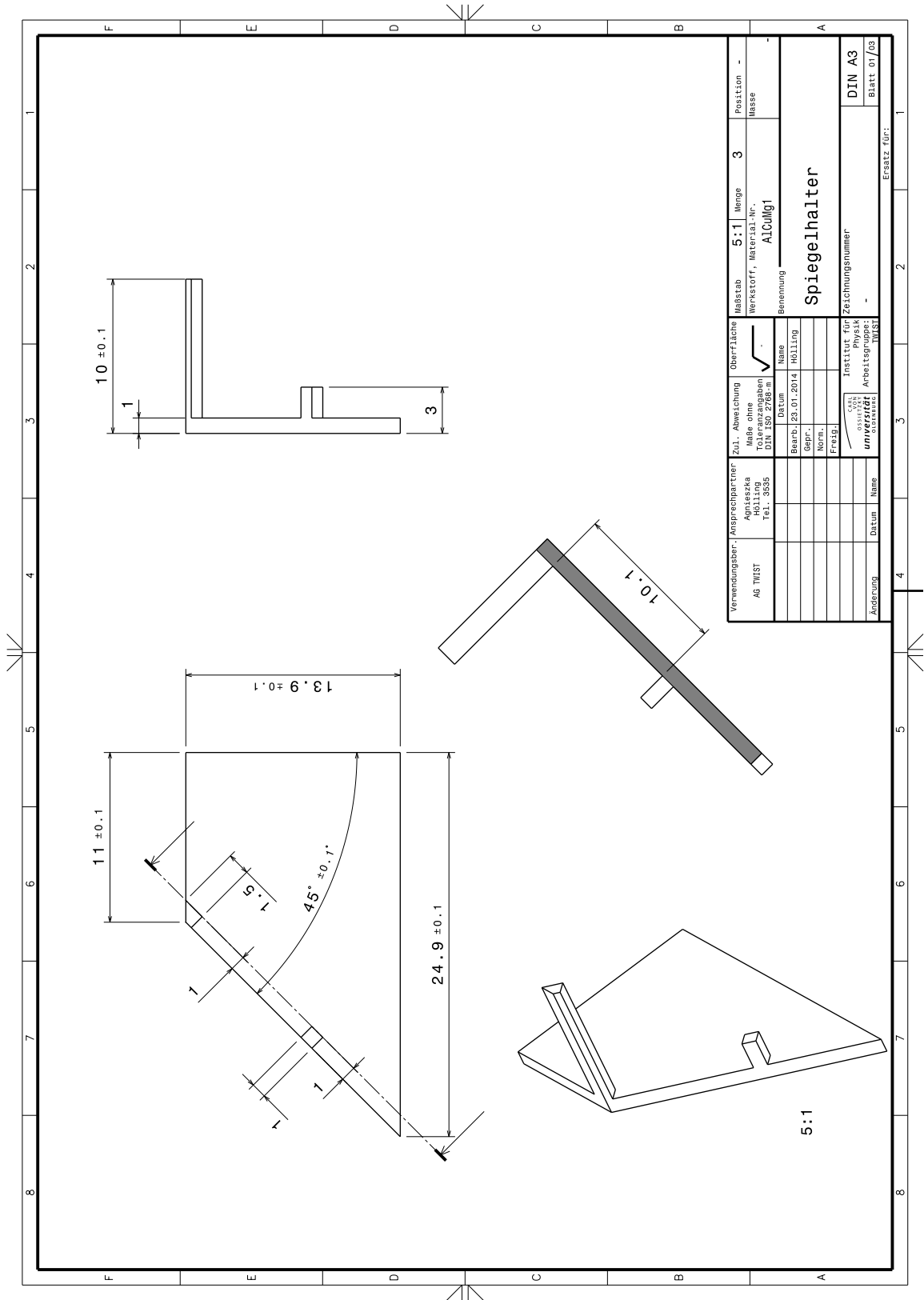


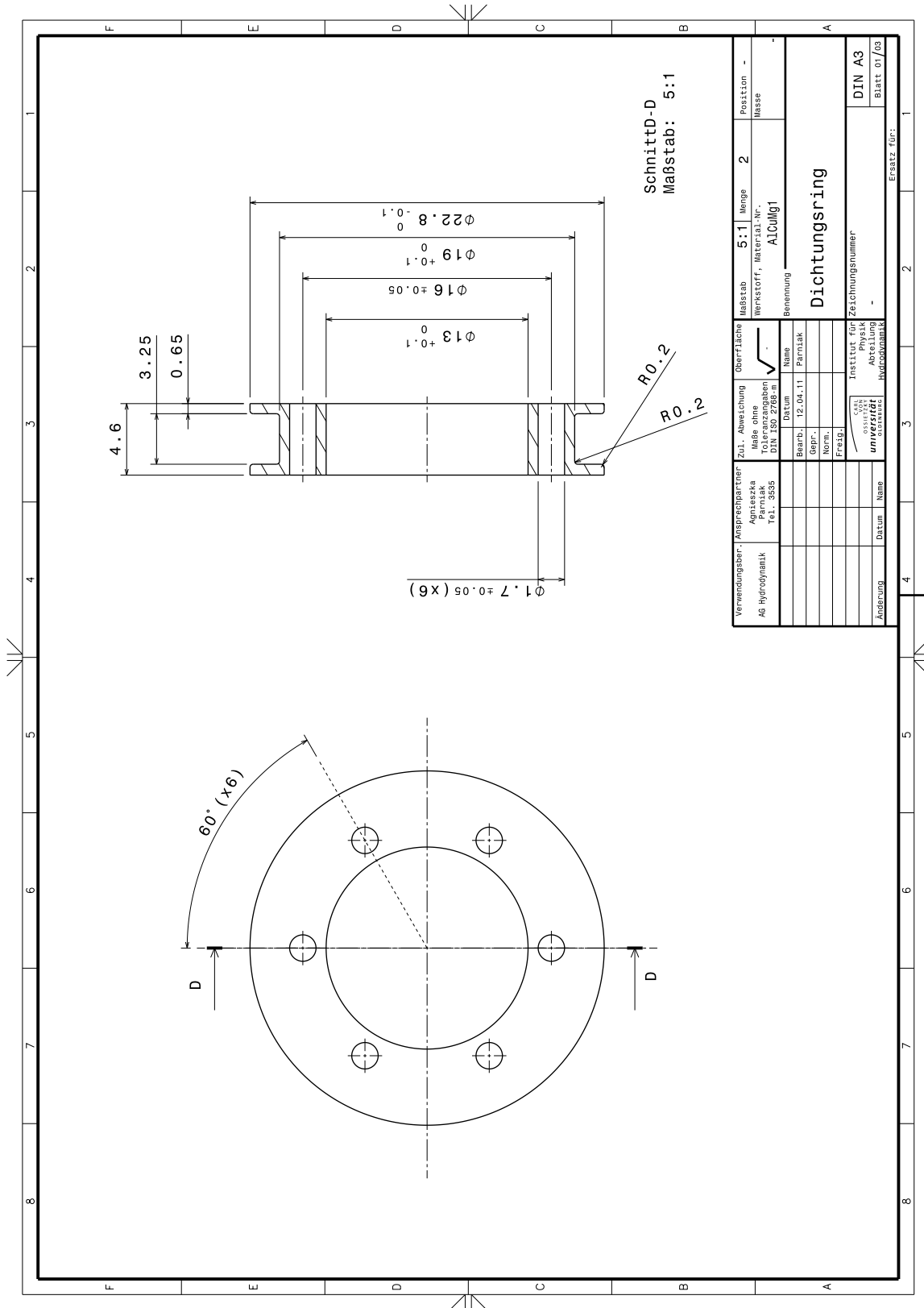
Figure H.3: Circuit diagram for the power supply used in the central unit.

Appendix I

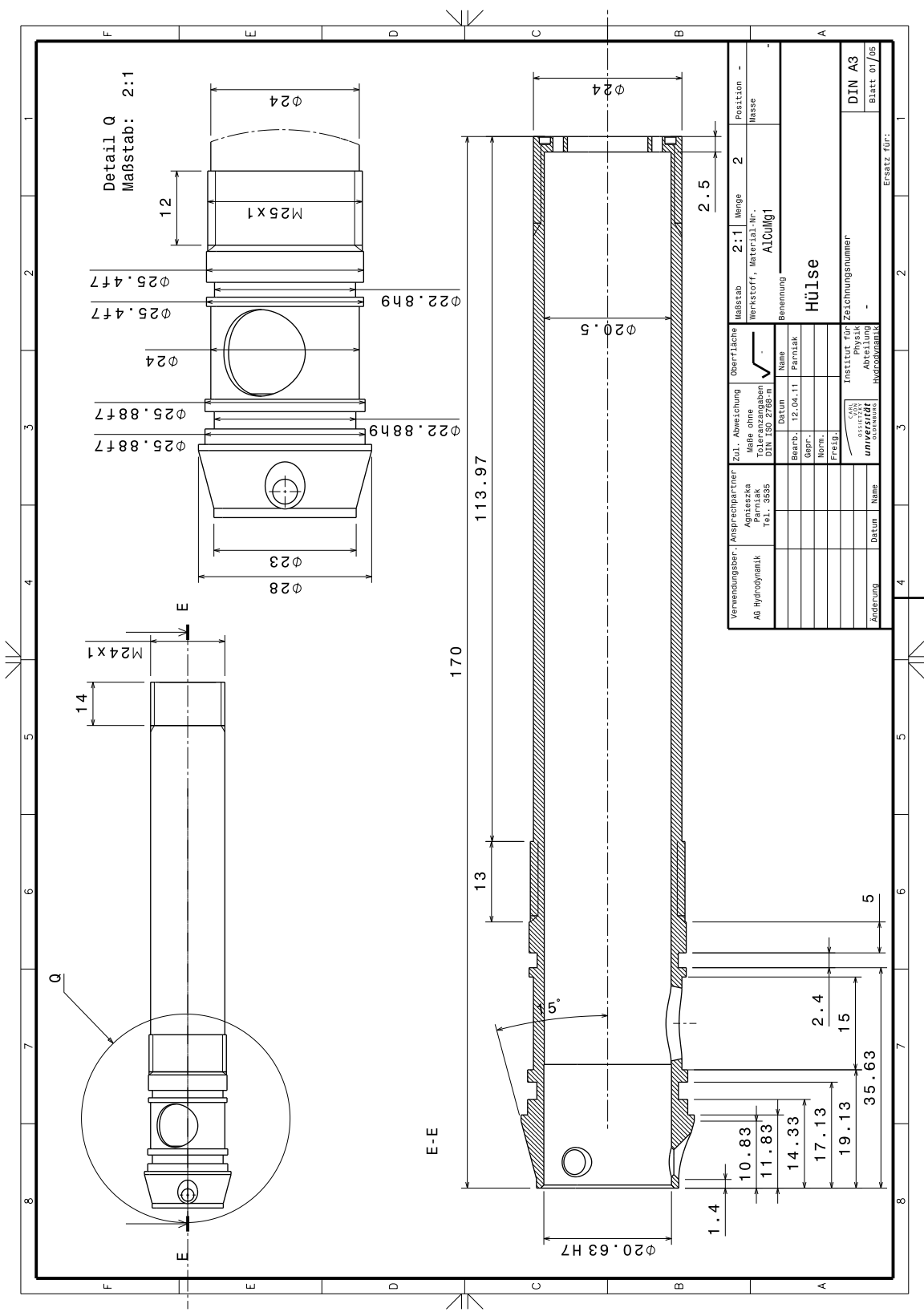
Technical drawings



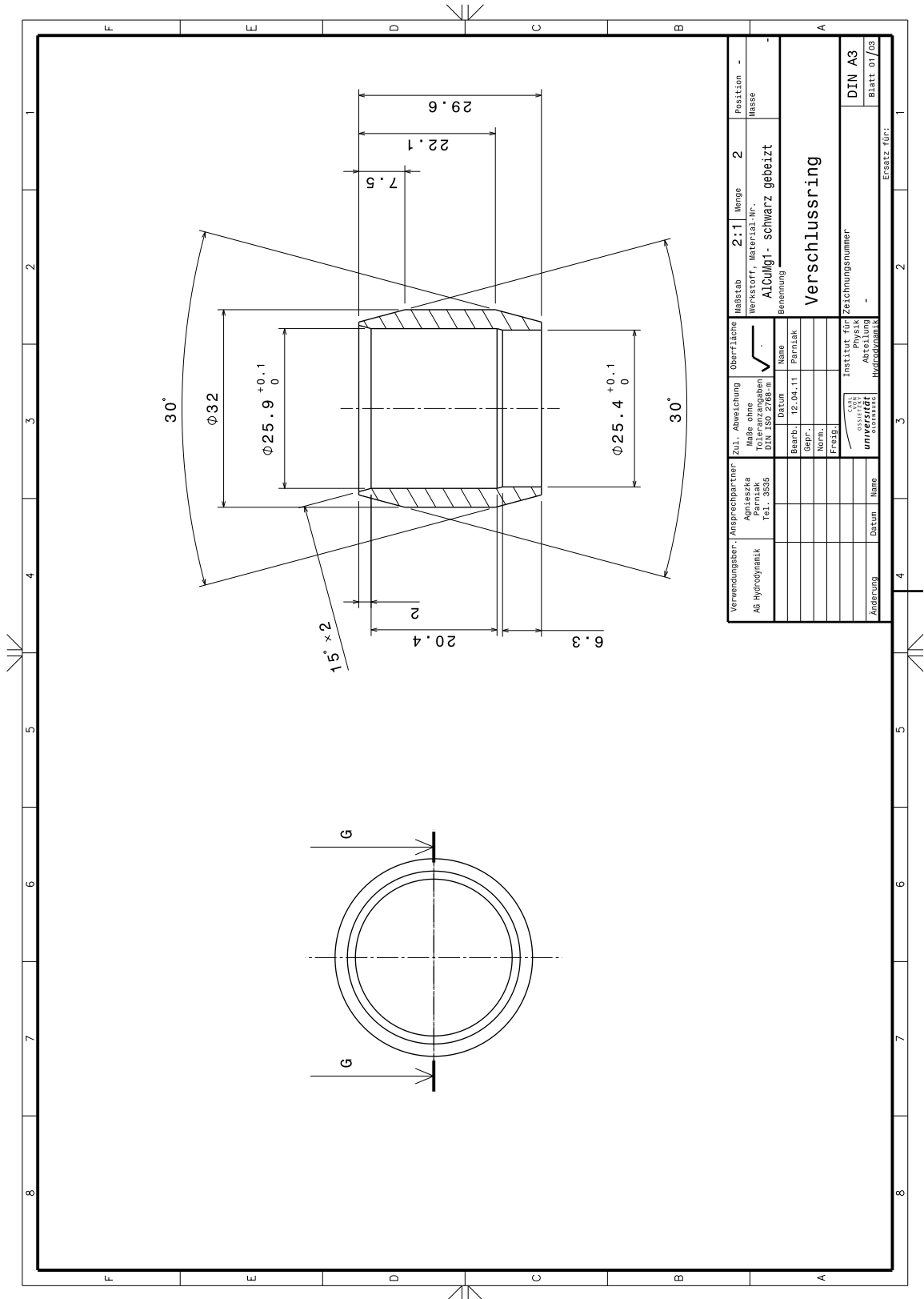
| | | | | | | | | | | | | |
|------------------|----------|------------------|------------------------------|------------------|---|--------------|--------------------------|----------------------|--------|---|-----------|------------------|
| Verwendungsber.: | AG TWIST | Ansprechpartner: | Agriaszka Helling Tel.: 5565 | Zul. Abweichung: | Masse ohne Toleranzangaben DIN ISO 2768-m | Oberrfläche: | Maßstab: | 5:1 | Menge: | 3 | Position: | Masse |
| | | | | | | | Werkstoff, Material-Nr.: | ALU0011 | | | | |
| | | | | | | | Benennung: | Spiegelhalter | | | | |
| | | | | | | | Name: | | | | | |
| | | | | | | | Datum: | | | | | |
| | | | | | | | Gepr.: | | | | | |
| | | | | | | | Norm.: | | | | | |
| | | | | | | | Freig.: | | | | | |
| | | | | | | | Institut für Physik | | | | | Zeichnungsnummer |
| | | | | | | | UMWELT | | | | | DIN A3 |
| Änderung | | Datum | Name | | | | | | | | | Blatt 01/08 |
| | | | | | | | | | | | | Ersatz für: |

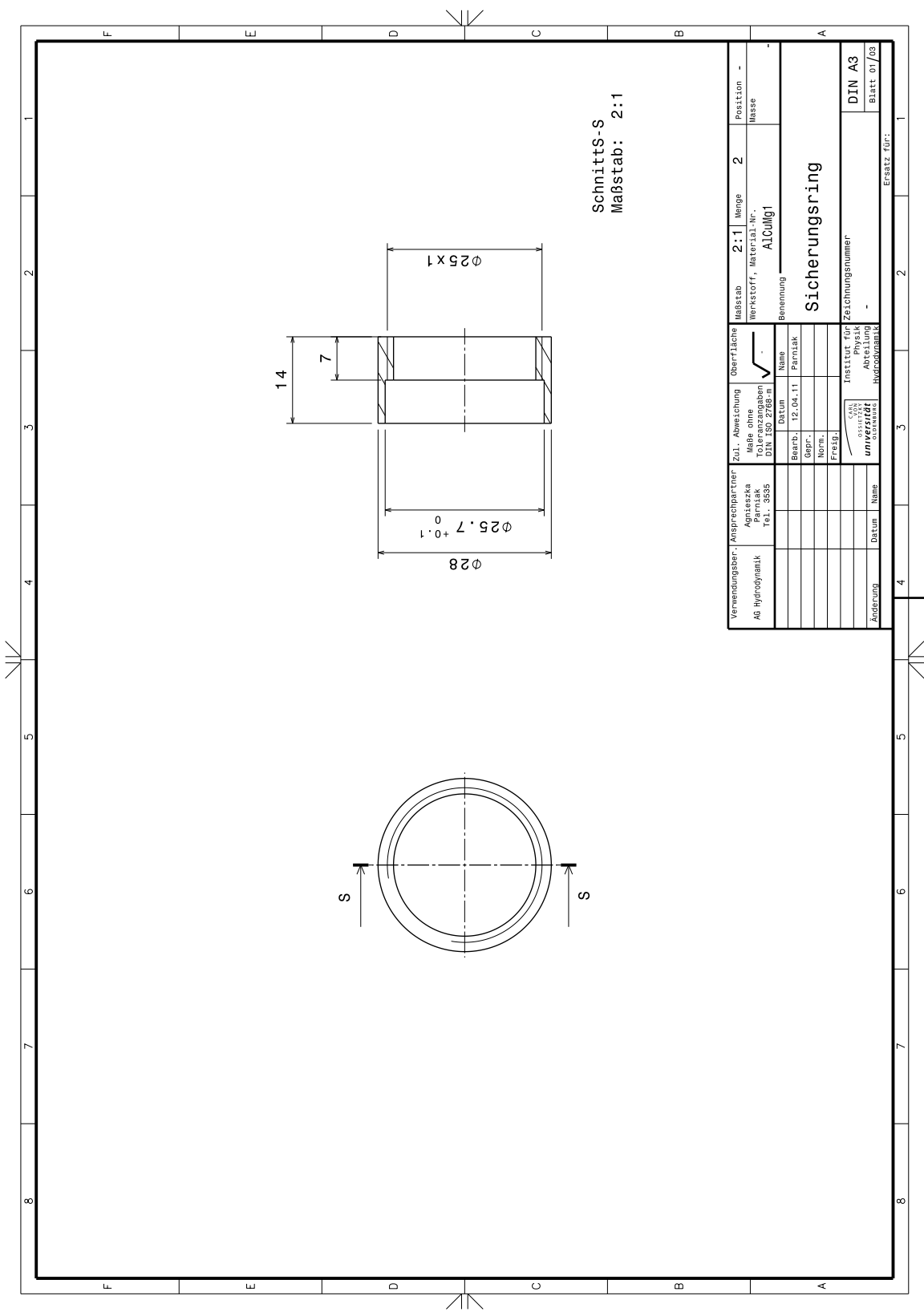


| | | | | | | | | | |
|------------------|-----------------|------------------|-------------------------------------|---|----------|------------------|--------------------------|---------------|---|
| Verwendungsber.: | AG Hydrodynamik | Ansprechpartner: | AgriSzexka Parniak Tel.: 5585 | ZUL. Abweichung: | Menge: | 2 | Position: | - | |
| | | | | Menge ohne Toleranzangaben DIN ISO 2768-m | Maßstab: | 5:1 | Werkstoff, Material-Nr.: | AluAlu11 | |
| | | | | Bepr.: | Datum: | 12.04.11 | Benennung: | Dichtungsring | |
| | | | | Norm.: | Name: | Parniak | | | |
| | | | | Freig.: | | | | | |
| Änderung: | Datum | Name | | Institut für Hydrodynamik Abteilung Hydrodynamik | | Zeichnungsnummer | | DIN A3 | |
| | | | | Upr. Normale | | - | | Blatt 01/08 | |
| | | | | | | | | Ersatz für: | 1 |



| | | | | | | | | | | | | | |
|------------------|-----------------|------------------|-------------------------------|--------------------------------|--|---------------------|-----------|-------------|-------|-------------|---|-----------|-------|
| Verwendungsber.: | AG Hydrodynamik | Anspruchpartner: | Agneszka Parniak Tel. 3555 | Zul. Abweichung: | Menge ohne Toleranzangaben DIN ISO 2768-m | Oberrfläche: | ALUMINIUM | Maßstab: | 2:1 | Menge: | 2 | Position: | Masse |
| Änderung: | | Datum: | | Bearb.: | 12.04.11 | Name: | Parniak | Benennung: | Hülse | | | | |
| | | Gepr.: | | Norm.: | | Freib.: | | | | | | | |
| | | Datum: | | Institut für Zeichnungennummer | | Institut für Physik | | Blatt 01/05 | | Ersatz für: | | DIN A3 | |





Schnitts-S
Maßstab: 2:1

| | | | | | | |
|---------------------------------|--|--|---|----------------|---------|------------|
| Verwendungsber. AG Hydrodynamik | Ansprechpartner Agrileszka Parniak Tel. 3555 | Zul. Abweichung Maße ohne Toleranzangaben DIN ISO 2768-m | Überfläche | Maßstab 2:1 | Menge 2 | Position - |
| | | | Werkstoff, Material-Nr. ALUQUIG1 | | | Masse |
| | | | Benennung | Sicherungsring | | |
| Änderung | Datum | Name | Institut für Zeichnungenummer | | | |
| | | | SIL Institut für Physik Abt. Hydrodynamik | | | |
| | | | Ersatz für: DIN A3 Blatt 01/03 | | | |

Bibliography

- [1] M. R. C. Bell, J.P. Richter, *The Notebooks of Leonardo da Vinci Vol. 2*, Dover Pubns (1970)
- [2] R. Ecke, *The Turbulence Problem, An Experimentalist Perspective*, Los Alamos Science No. 29 (2005)
- [3] B. Eck, *Technische Strömungslehre*, Springer (1978)
- [4] H. Sigloch, *Technische Fluidmechanik*, Schroedel (1980)
- [5] L. F. Richardson, *Weather Prediction by Numerical Process*, Cambridge University Press (1922)
- [6] U.Frisch, *Turbulence: the Legacy of A.N.Kolmogorov*, Cambridge University Press (1995)
- [7] C.Meneveau, K.R.Sreenivasan , *The multifractal nature of turbulent energy dissipation*, *J. Fluid Mech.* Vol.224,429 (1991)
- [8] R. Zheng, *Multiscales and cascade in isotropic turbulence*,
- [9] A. N. Kolmogorov, *The local structure of turbulence in an incompressible viscous fluid for very high Reynolds number*. *Dokl. Akad. Nauk. SSSR* (1941)
- [10] T. Ishihara, Y. Kaneda, M. Yokokawa, K. Itakura, A. Uno, *Small-scale statistics in high-resolution direct numerical simulation of turbulence: Reynolds number dependence of one-point velocity gradient statistics*, *J. Fluid Mech.* vol. 592, pp. 335–366, Cambridge University Press (2007)
- [11] S. B. Pope, *Turbulent Flows*, Cambridge University Press (2000)
- [12] H. Awbi, *Ventilation of Buildings*, Routledge (2003)
- [13] J. Fraden, *Handbook of Modern Sensors*, Springer Science+Business Media (2010)

- [14] J.G. Webster, The Measurement, Instrumentation and Sensors Handbook, Crc Pr inc (1998)
- [15] F. E. Jørgensen, How to measure turbulence with hot-wire anemometers, Dantec Dynamics A/S (2002)
- [16] H.H. Bruun, Hot-Wire Anemometry, Oxford University Press Inc., New York (1995)
- [17] C. Renner, Markowanalysen stochastisch fluktuierender Zeitserien, Doctoral Thesis, University of Oldenburg (2002)
- [18] C. Renner, Über Untersuchungen der Statistik von Geschwindigkeitsfluktuationen in einem turbulenten Freistrah, Diploma Thesis, University of Oldenburg (1997)
- [19] G. I. Taylor, Statistical Theory of Turbulence, Proceedings of the Royal Society of London, Series A, Mathematical and Physical Sciences, Vol. 151, No. 873, pp. 444-454 (1935)
- [20] P. K. Kundu, I.M. Cohen, D.R. Dowling, Fluid Mechanics, 5th Edition, Academic Press (2011)
- [21] W. K. George, Lectures in Turbulence for the 21st Century (2013)
- [22] A.N. Kolmogorov, A refinement of previous hypotheses concerning the local structure of turbulence in a viscous incompressible fluid at high Reynolds number, J. Fluid Mech. **13**, 82-85, (1962)
- [23] E. Sekula, The Structure of Turbulent Jets: Application of Experimental and Environmental Methods, Universitat Politecnica de Catalunya (2010)
- [24] P.A. Davidson, Turbulence - An Introduction for Scientists and Engineers, Oxford University Press (2004)
- [25] M. Siefert, Analyse der kleinskaligen Turbulenz mittels multivariater Markovprozesse, Doctoral Thesis, University of Oldenburg (2004)
- [26] Henrik Andersson, Position Sensitive Detectors - Device Technology and Applications in Spectroscopy, Doctoral Thesis, Mid-Sweden University (2008)
- [27] Simon M. Sze, Kwok K. Ng, Physics Of Semiconductor Devices, John Wiley & Sons Inc. (1981)

- [28] Position Sensitive Detector, Product catalog KPSD0001E01, Hamamatsu Photonics K.K. Solid State Division (2002)
- [29] D. Aronson, L. Løfdahl. The plane wake of a cylinder. Measurements and inferences on the turbulence modelling. *Phys. Fluids A* 5, 1433 (1993)
- [30] B. Castaing, Y. Gagne, E. J. Hopfinger, Velocity probability density functions of high Reynolds number turbulence, *Physica D* 46 177-200 (1990)
- [31] G. Kampers, Einfluss von unterschiedlichen Drahtlängen auf Hitzdrahtmessungen in turbulenten Strömungen, Master Thesis, University of Oldenburg (2012)21, 645
- [32] G. Kampers, Charakterisierung und Optimierung der Reflexionseigenschaften von Cantilevern für die Laser-Cantilever-Anemometrie (Bachelor Thesis), University of Oldenburg, Germany (2009)
- [33] Segalini A., Örlü R., Schlatter P., Alfredsson P.H., Rüedi J.D. and Talamelli A., A method to estimate turbulence intensity and transverse Taylor microscale in turbulent flows from spatially averaged hot-wire data, *Exp. Fluids*, (2011)
- [34] M. Hölling, Sensorentwicklung für Turbulenzmessungen (Diss.), University of Oldenburg, Germany (2008)
- [35] C. Beck, Superstatistics in hydrodynamic turbulence *Physica D* 193 195-207 (2004)
- [36] J. Puczyłowski, Weiterentwicklung des 2D Laser-Cantilever-Anemometers (Master Thesis), University of Oldenburg, Germany (2009)
- [37] S. Barth et al., Laser-Cantilever-Anemometer - A new high resolution sensor for air and liquid flows, *Rev. Sci. Instrum.* 76, 075110 (2005)
- [38] E. Hau, Wind turbines, Springer; 3rd edition (2013)
- [39] M. Onorato, R. Camussi, G. Iuso, Small scale intermittency and bursting in a turbulent channel flow, *Physical Review E* Volume 61, no. 2 (2000)
- [40] M. Li, R. Bhiladvala, T.J. Morrow, J.A. Siooss, K. Lew, J.M. Redwing, C.D. Keating, T.S. Mayer, Bottom-up assembly of large-area nanowire resonator arrays, *Nature Nanotechnology* VOL 3 (2008)

- [41] J. E. Sader, Frequency response of cantilever beams immersed in viscous fluids with applications to the atomic force microscope, *Journal of Applied Physics* 84, 64 (1998)
- [42] Q. Sun, Information preservation methods for modeling micro-scale gas flows, *Doctoral Thesis, University of Michigan* (2003)
- [43] R. Benzi, S. Ciliberto, R. Tripicciono, C. Baudet, F. Massaioli, S. Succi, Extended self-similarity in turbulent flows, *Physical IReview E*, Volume 48, No 1 (1993)
- [44] S. F. Hoerner, Fluid-Dynamic Drag, *Hoerner Fluid Dynamics* (1958)
- [45] M. Wilczek, H. Xu, Y. Narita, A note on Taylor's hypothesis under large-scale flow variation, *Nonlin. Processes Geophys.*, 21, 645-649 (2014)
- [46] M. Vallikivi, Turbulence measurements with a nano-scale thermal anemometry probe, *Master thesis, Chalmers University* (2010)
- [47] P. Valent, J. C. Vassilicos, Dissipation and decay of fractal-generated turbulence, *Physics of Fluids*, 23, 119101 (2011)
- [48] R. Grauer, H. Homann, J.F. Pinton, Longitudinal and transverse structure functions in high-Reynolds-number turbulence, *New Journal of Physics* 14 063016 (2012)
- [49] M. Siefert, J. Peinke, Different cascade speeds for longitudinal and transverse velocity increments of small-scale turbulence, *PHYSICAL REVIEW E* 70, 015302(R) (2004)

Acknowledgement

I would like to thank all members of the TWiSt group for the great cooperation and support of my work.

A special thanks goes to Joachim Peinke who intergrated me into his group and gave me the opportunity to work on this thesis. I am also grateful for numerous fruitful discussions and the possibilities to participate in many domestic and international conferences that helped me to widen my horizon.

Another special thanks goes to Michael Hölling who has introduced me to my thesis subject and supported my work in the lab and during data analysis. His critical questions had a positive influence on this thesis.

I would like to thank Rustom Bhiladvala for his great hospitality while our laboratory times in Canada and the effort he invested to help me with my work. Also, I am very happy to have him as my second supervisor for this thesis.

Ingrid Neunaber, Gerrit Kampers and Agnieszka Hölling deserve a special mention for helping me with measurements and designing. Another big thank goes out to Achim Kittel, Alois Schaffarczyk and Gerd Gülker for fruitful discussions and advice.

Erklärung

Ich erkläre hiermit, dass

- (a) eine Promotion zum Dr. rer. nat. angestrebt wird,
- (b) ich diese Arbeit selbstständig verfasst und nur die angegebenen Hilfsmittel benutzt habe, und dass die Arbeit in Teilen bereits veröffentlicht bzw. zur Veröffentlichung eingereicht wurde,
- (c) diese Dissertation weder in ihrer Gesamtheit noch in Teilen einer anderen Hochschule zur Begutachtung in einem Promotionsverfahren vorgelegen hat.

Oldenburg, den 17. April 2015

.....

(Jaroslaw Puczyłowski)

Curriculum

Personal information:

| | |
|----------------|----------------------|
| Name | Jaroslav Puczyłowski |
| Birthday | 12.10.1982 |
| Place of birth | Cosel, Poland |
| Citizenship | German |

Education:

| | |
|-------------------|--|
| 09/1999 – 07/2003 | Fachgymnasium für Technik Oldenburg |
| 10/2003 – 04/2006 | Carl von Ossietzky Universität Oldenburg |
| 05/2006 – 04/2007 | California State University, Long Beach, USA |
| 04/2007 – 07/2009 | Carl von Ossietzky Universität Oldenburg |

Scientific experience:

| | |
|-------------------|---|
| 10/2008 | Bachelor of Engineering, Universität Oldenburg |
| 02/2010 | Master of Science, Universität Oldenburg |
| 01/2010 – 01/2011 | Wissenschaftlicher Mitarbeiter, ForWind |
| 02/2011 – 04/2015 | Wissenschaftlicher Mitarbeiter, Universität Oldenburg |

List of publications

Peer-reviewed publications

- J. PUCZYLOWSKI, M. HÖLLING, J. PEINKE, A. HÖLLING,
R. BHILADVALA:
A new approach to highly resolved measurements of turbulent flow
Meas. Sci. Technol. 26 (2015) 055302 (12pp)

Conference proceedings

- J. PUCZYLOWSKI, M. HÖLLING, J. PEINKE:
New anemometer for atmospheric turbulent flow
Proceedings of The Science of Making Torque
Heraklion, Griechenland, Greece, 28.- 30.06.2010
- H.HEISSELMANN, J. PUCZYLOWSKI, M. HÖLLING, J. PEINKE:
Development of highly resolving drag based anemometers
Progress in Turbulence IV, iTi 2010 Proceedings
Bertinoro, Italien, 19.-23.09.2010
- H.HEISSELMANN, J. PUCZYLOWSKI, M. HÖLLING, M. WÄCHTER, J. PEINKE:
Development and Characterisation of Highly Resolving Wind Speed and
Direction Sensors
DEWEK 2010, 10th German Wind Energy Conference
Bremen, Deutschland 17.-18.11.2010
- J. PUCZYLOWSKI, M. HÖLLING, J. PEINKE:
Velocity Measurements in turbulent flows performed by a 2D-Laser Can-
tilever Anemometer
International Symposium on Applications of Laser Techniques to Fluid
Mechanics
Lissabon, Portugal 05.- 08.07.2010
- J. PUCZYLOWSKI, M. HÖLLING, J. PEINKE:
New anemometer for highly resolved measurements of atmospheric tur-
bulence
The Science of Making Torque from Wind
Oldenburg, Deutschland 9.-11.10.2012

J. PUCZYLOWSKI, I. NEUNABER, M. HÖLLING, J. PEINKE:

New anemometer for highly resolved measurements in atmospheric flows

EWEA 2013 Annual Event

Wien, Österreich 4.-7.02. 2013